REPORT DOCUMENTATION PAGE

Form Approved
OMB NO. 0704-0188

Public Reporting burden for this collection of information is estimated to average 1 hour per response, including the time for reviewing instructions, searching existing data sources, gathering and maintaining the data needed, and completing and reviewing the collection of information. Send comment regarding this burden estimates or any other aspect of this collection of information, including suggestions for reducing this burden, to Washington Headquarters Services, Directorate for information Operations and Reports, 1215 Jefferson Davis Highway, Suite 1204, Arlington, VA 22202-4302, and to the Office of Management and Budget, Paperwork Reduction Project (0704-0188,) Washington, DC 20503.

1. AGENCY USE ONLY	2. REPORT DATE 02/28/2004	3. REPORT TYPE AND DATES COVERED Final Report; (03/01/01- 11/30/03)

4. TITLE AND SUBTITLE Dynamic Cracking and Eneregy Absorption in Laminates Containing Through-Thickness reinforcement	5. FUNDING NUMBERS DAAD19-01-C-0083

6. AUTHOR(S)
S.Narayanaswamy and B. N. Cox

7. PERFORMING ORGANIZATION NAME(S) AND ADDRESS(ES) Rockwell Scientific, 1049 Camino Dos Rios Thousand Oaks, CA 91360	8. PERFORMING ORGANIZATION REPORT NUMBER

9. SPONSORING / MONITORING AGENCY NAME(S) AND ADDRESS(ES) U. S. Army Research Office P.O. Box 12211 Research Triangle Park, NC 27709-2211	10. SPONSORING / MONITORING AGENCY REPORT NUMBER 42711.1-MS

11. SUPPLEMENTARY NOTES
The views, opinions and/or findings contained in this report are those of the author(s) and should not be construed as an official Department of the Army position, policy or decision, unless so designated by other documentation.

12 a. DISTRIBUTION / AVAILABILITY STATEMENT Approved for public release; distribution unlimited.	12 b. DISTRIBUTION CODE

13. ABSTRACT (Maximum 200 words)

Inertial effects in the mechanism of fibre pullout were examined, with emphasis on how the rate of propagation of stress waves along the fibre, and thence the pullout dynamics, are governed by friction and the propagation of companion waves excited in the matrix. The frictional sliding between the fibre and the matrix is described by a constant interfacial friction stress, the sign of which depends on the relative particle velocity of the fibre and the matrix. The analytical results were also validated by detailed numerical finite element calculations with a cohesive law simulating interfacial friction. In addition to the theoretical work, through a sub-contract to ETech, we performed fundamental experiments to investigate the process of dynamic interfacial debonding and fiber push-in, especially in 2D model composite systems. With the use of high speed diagnostics, a quantitative comparison was made between the experimental observations and the theoretical results and they show excellent agreement. Steady state crack propagation characteristics in through thickness reinforced laminate structures was mapped out in terms of controllable loading and material parameters including the crack velocity and the properties of the through-thickness reinforcement

14. SUBJECT TERMS			15. NUMBER OF PAGES 176
			16. PRICE CODE

17. SECURITY CLASSIFICATION OR REPORT UNCLASSIFIED	18. SECURITY CLASSIFICATION ON THIS PAGE UNCLASSIFIED	19. SECURITY CLASSIFICATION OF ABSTRACT UNCLASSIFIED	20. LIMITATION OF ABSTRACT UL

Copy #_____

Dynamic Cracking and Energy Absorption in Laminates Containing Through-Thickness Reinforcement

Final Report for 03/01/01–11/30/03

Contract No. DAAD19-01-C0083

Prepared for:

U.S. Army Research Office
ATTN: AMSRL–RP–RI
P.O. Box 12211
Research Triangle Park, NC 27709-2211

Prepared by:

B.N. Cox and S. Narayanaswamy
Rockwell Scientific
1049 Camino Dos Rios
Thousand Oaks CA 91360

February 2004

ROCKWELL SCIENTIFIC

Table of Contents

1. INTRODUCTION

This is the final report for our contract No. DAAD19-01-C-0083 "Dynamic Cracking and Energy Absorption in Laminates Containing Through-Thickness reinforcement" covering the period March 1, 2001 through November 30, 2003. We summarize major basic research results in the delamination resistance of through thickness reinforced structures under dynamic loading conditions. Leveraging collaborations at Los Alamos National Lab (with Dr. Irene Beyerlein), at E Tech (with Prof. Ares Rosakis) and at Northwestern U (with Prof. Roberta Massabo) will be described.

2. STATEMENT OF PROBLEM STUDIED

The central theoretical problem studied was the fracture problem of dynamic delamination cracking in the presence of large scale bridging (LSB) and the micromechanical problem of how through-thickness reinforcement responds to dynamic mixed mode crack displacement. The design rules for optimization of the structure will be based on insight developed through fundamental understanding of dynamic delamination in the presence of through-thickness reinforcement. To achieve this goal, research included:

I. Identifying fracture mechanisms especially those relating to dynamic deformation of through-thickness reinforcement in the neighbourhood of a delamination crack.

II. Formulating efficient solutions to the problem of a delamination crack propagating dynamically though laminated specimens under conditions of LSB.

III. Analysing the dynamic constitutive law for through-thickness reinforcement acting as bridging entities in the wake of a dynamic delamination crack.

IV. Mapping the solution domain for the dynamic LSB problem.

3. SUMMARY OF IMPORTANT RESULTS

Highlights of our accomplishments are as follows:

(i)   Using beam theory dynamic mode I crack propagation in through-thickness reinforced laminate structures was studied. In particular, steady state dynamic crack growth for a

Double Cantilever Beam (DCB) loaded with a flying wedge was examined [1,3]. This analysis provides guidelines for design of experiments to probe the efficacy of bridging on improving the dynamic fracture toughness of through thickness reinforced structures.

(ii)   Steady state crack propagation characteristics in through thickness reinforced laminate structures was mapped out in terms of controllable loading and material parameters including the crack velocity and the properties of the through-thickness reinforcement. For small crack velocities, the through-thickness reinforcement considerably enhances the delamination resistance of the structure. At higher velocities, the kinetic energy term dominates the overall energetics and the relative effect of the reinforcement on increasing the delamination resistance is insignificant. The model suggests a simple fracture test for estimating the properties of the through-thickness reinforcement under dynamic loading conditions.

(iii)   The character of the displacement profile for mode I cracking behavior of a symmetric laminate containing a large bridging zone shows features similar to those in the analogous static loading problem [5], including the possibility of oscillations extending far into the crack wake. However, the details of the functional form of the profile, including the existence of oscillations, depend on the crack velocity.

(iv)   Even for moderately large crack velocities, kinetic energy dominates the fracture process and the relative effect of both the bridging contribution of the reinforcement and the intrinsic fracture toughness of the laminate are small. For small to moderate crack velocities, the steady state cracking characteristics are very strongly influenced by the bridging mechanism, which significantly enhances the delamination resistance of the structure. This is reflected both in the equilibrium force required to drive the wedge as well as in the wedge-crack tip separation distance. This regime is of the most practical significance, since low crack velocities will be favored for other loading configurations, such as normal impact on the laminate, to avoid the penalty of imparting high kinetic energy to the material. In crack propagation solutions where the crack tip is not

constrained to travel at a given velocity, here the velocity of the wedge, it will seek an energetically favourable velocity. Through-thickness reinforcement might thus be regarded as removing easy, low velocity fracture paths under certain dynamic conditions.

(v)   Inertial effects in the mechanism of fibre pullout (or push-in) in composites was examined, with emphasis on how the rate of propagation of stress waves along the fibre, and thence the pullout dynamics, are governed by friction and the propagation of companion waves excited in the matrix [2,4]. With a simple shear lag model, the effect of uniform frictional coupling between the fibre and the matrix is accounted for in a straightforward way. Analytical solutions are derived when the pullout load increases linearly in time.

(vi)   We find in the pullout problem that the process zone of activated material is generally divided into two or three domains along the axis of the fibre. Within these domains, slip in the sense implied by the load, slip in the opposite sense (reverse slip), and stick may be observed. The attainable combinations define three regimes of behavior, which are realized for different material parameter values. The elastodynamic problem was also solved more accurately using finite element methods, with friction represented by an interfacial cohesive zone. The predictions of the shear lag theory are broadly confirmed.

(vii)   Numerical results encourage the use of the shear lag approximation in dynamic pullout problems, where quantities that have been averaged in the direction normal to the fibre axis are of interest. The shear lag approximation appears to be at least as viable for dynamic problems as it has proven for static problems. Good agreement in the load-displacement relation, for example, is found. Agreement in the predicted length of the process zone is obtained as long as the process zone length is $2 - 4$ times the fibre radius. Since the evolution of domains of slip, stick, and reverse slip can become very complicated for general loading histories, an analytical approach could be particularly valuable.

(viii) With the aid of the dynamic pullout law derived above, simple criteria were determined for significant inertial effects in representative crack propagation problems. Also fast numerical solutions were formulated for general loading cases and hence have a scheme to compute the bridging law for fairly general conditions [12]. This will be required to solve large-scale bridging, dynamic crack problems to self-consistency (bridging tractions unknown *a priori*). The history dependent bridging law thus computed will form the basic ingredient in the computation of the structural response of the composite under dynamic loading conditions.

(ix) The dynamic crack energy release rate as a function of the local crack tip velocity has been computed for a material possessing orthotropic symmetry under general mixed mode loading conditions. The dynamic energy release rate varies as $O[(v_r - v)^{-1}]$ as $v \rightarrow v_r$, and where v is the crack speed and v_r is the Rayleigh wave speed. We find that the variation in the dynamic crack energy relase rate for orthotropic materials can be rationalized in terms of the orthotropy parameters λ and ρ, just as in the static case. This computation of the dynamic energy release rate is necessary to calculate the energetics of crack growth for standard engineering specimens [13].

(x) An approximate formula for the static weight function that describes the crack tip stress intensity factor due to a pair of point loads on the fracture surface of an orthotropic delamination specimen has been postulated and validated numerically [7]. This weight function enables accurate solution of mode I delamination problems in the presence of large scale bridging over all crack length regimes, since it avoids the errors of beam theory in describing the singular crack tip fields. However, comparison of results for large scale bridging problems with a Dugdale (uniform traction) bridging law shows that a beam theory model with appropriate crack tip corrections (available in the literature) may be acceptably accurate. The weight functions will be used to formulate integral equation solutions, which will be to ensure that accurate results are always available at least as a reference in future work. Extension to mode II loading and dynamic weight functions is under way.

(xi).   Upon passing of the crack tip, a debond crack propagates along the length of the fibre away from the fracture plane. Propagation of the debond crack is governed by the fracture energy associated with the separation of the matrix and the fibre at the debond crack tip and the work done against friction in displacing the debonded fibre along its axis. In many composites, the debond energy is small and pullout is dominated by friction over a wide range of pullout displacements. However, to deal with cases where this assumption is not true, we developed a theoretical framework that incorporates the debond energy in the pullout model. Although, simple extensions of shear lag models are available to deal with debond energy contribution for the quasistatic loading case, the corresponding formalism for the dynamic case appears much more complicated [15].

(xii)   A subcontract was issued to Etech, Inc. for experiments to gain understanding of the mechanics of fibre push-in (analogous to pullout) under dynamic loading [14]. The first experiments have already been completed (Owen and Rosakis) and the key strain field and velocity data successfully recorded. Dynamic photoelasticity was used to reveal the nature of the stress fields associated with the dynamic sliding process. The role of impact speed (loading rate) was investigated at a constant static pre-load. At a short distance behind the propagating front, kinks in the fringes form in angled bands. These bands intersect the top and bottom interfaces and reveal the region of sliding propagating along the interface. From a sequence of images, the speed of propagation of sliding was measured and from analysis of the fringes, estimates of the loading rate and the stresses along the interface were made. A numerical FEM cohesive model has been proposed to understand the experimentally observed deformation profiles [12].

(xiii)   The elastic interaction of multiple delaminations in laminated structures subject to out of plane loading has been investigated [16]. The study has shown that there are significant short and long range interaction effects between cracks in a structure with multiple delaminations. These interaction effects can be shielding or amplification of the energy release rate of a crack and strongly depend on geometry of the system.   Additional

effects, such as friction in the regions of the crack face contact and the effect of cohesive and bridging mecahnis acting along the cracks are under investigation.

(xiv)   As part of our objective of fostering multi-disciplinary interactions with the rest of the community, we organized a focused workshop on the fundamentals of dynamic cracking, as a joint effort with Dr. Huajian Gao of the Max Planck Institute, Germany, Professor Dietmar Gross of Darmstadt University, Germany, and Professor Daniel Rittel of Technion University, Israel. The workshop was held from July 14 – 18, 2003 at the Max Planck Institute's Ringberg Castle, in Bavaria. Our objective in the workshop was to entertain vigorous discussions of recent, significant advances in our understanding of the fundamentals of dynamic fracture at various scales; and to look for better definition of future research objectives.   We reviewed recent, significant advances in our understanding and to discuss future research objectives [17]. We feel that this field is very ripe for the establishment of new directions to take advantage of greatly increased fundamental knowledge and the workshop was an excellent vehicle for identifying such directions.

4. LIST OF PUBLICATIONS PREPARED UNDER THIS CONTRACT

Papers in peer-reviewed journals

1.* N.Sridhar, R. Massabò, B.N.Cox and I.J.Beyerlein, *"Delamination Dynamics in Through-Thickness Reinforced Laminates with application to DCB Specimen"*, *International J. of Fracture*, Vol. 118, pp.119-144, (2002)
2.* N.Sridhar, Q.D.Yang and B.N.Cox, "Stick, Slip and Reverse Slip Characteristics during Dynamic Fiber Pullout", *J. Mechanics and Physics of Solids*, Vol.51, Number 7, pp.1215-1241, (2003)
3.* B.N.Cox and N.Sridhar, "A Traction Law for Fiber Tows Bridging Mixed Mode Cracks", *Mechanics of Composite Materials and Structures*, Vol. 9, pp.299-331, (2002)
4.* B.N.Cox, N.Sridhar, and I.J.Beyerlein, "Inertial effects in the Pullout Mechanism during Dynamic Loading of a Bridged Crack", *Acta Materialia*, 49, pp.3863-3877, (2001)
5. R. Massabò and B. N. Cox, "Unusual Characteristsics of Mixed Mode Delamination Fracture in the Presence of Large Scale Bridging," *Mechanics of Composite Materials and Structures*, Vol. 8, pp.61-80, (2001)
6. M. A. McGlockton, B. N. Cox, and R. M. McMeeking, "A binary Model of Textile Composites: III High Failure Strain and Work of Fracture in 3D weaves", *J. Mechanics and Physics of Solids*, Vol.51, Number 8, pp.1573-1600, (2003)
7. R. Massabò, L. Brandinelli, and B. N. Cox, "Mode I Weight Function Methods for an Orthotropic Double Cantilever Beam," *Int. J. of Eng. Science, 41, 1497-1518, 2003.*

Papers in conference proceedings
8. N. Sridhar, Q.D.Yang, and B.N.Cox , "Characteristics of Fiber Pullout under Dynamic Loading Conditions", *2001 ASME Congress and* Exposition, New York, (2001)
9. N.Sridhar, I.J.Beyerlein, B.N.Cox, and R. Massabò, "Dynamic Delamination in Through-Thickness reinforced DCB specimens", *Proc. Int. Conf. on Fracture, ICF10, Dec. 2001*
10. R. Massabò and B. N. Cox, "Beam Theory and Weight Function Methods for Mode I Delamination with Large Scale Bridging," *Proc.Int.Conf. on Fracture, ICF10, Dec. 2001.*
11. N.Sridhar, B.N.Cox, I.J.Beyerlein, and C.L.Dunn, "Mechanics of Crack bridging under dynamic loads", *MRS Fall Meeting*, V. 653, *Z.2.5.3,* Boston, December 2000

Papers to be submitted
12. N. Sridhar, Q.D.Yang, and B.N.Cox, "Dynamics of Fiber pullout under impact load condition," in preparation for submission to *Journal of Applied Mechanics*
13.* N.Sridhar, I.J.Beyerlein and B.N.Cox, "Computation of Dynamic Crack Energy Release Rate for Orthotropic Systems," in preparation for submission to *Journal of Applied Mechanics*
14.* A.Rosakis, Q.D.Yang, B.N.Cox and N.Sridhar, "The Physics of Dynamic Fiber Push-In Opposed by Friction ," prepared for submission to *Proc. of the Royal Society*

15. N.Sridhar, Q.D.Yang and B.N.Cox, *"Debond Crack Propagation during dynamic fiber pullout,"* in preparation for submission to *J. Mechanics and Physics of Solids*

16. M. Andrews, R. Massabò, and B. N. Cox, "Crack Stability under quasistatic Multiple Delamination,*"* in preparation for submission to *Int. J. of Solids and Structures.*

17.* B. N. Cox, H. Gao, D. Gross, and D.Rittel, "Modern Topics and Challenges in Dynamic Fracture"*,"* in preparation for submission to *J. Mechanics and Physics of Solids*

** Appended to report

5.   LIST OF PARTICIPATING SCIENTIFIC PERSONNEL

Dr. Sridhar Narayanaswamy,

Member of the Technical Staff, Materials Science Function

Rockwell Scientific

Dr. Qingda Yang,

Member of the Technical Staff, Materials Science Function

Rockwell Scientific

Dr. Brian Cox,

Principal Scientist, Materials Science Function

Rockwell Scientific

Prof. Roberta Massabò

Department of Civil Engineering, Northwestern University

Prof. Ares Rosakis

Department of Aeronautics, California Institute of Technology

Dr. Irene Beyerlein,

Member of the Technical Staff, Materials Science and Technology Division

Los Alamos National Laborator

<u>Student supported:</u>

Ms. Catherine Dunn, an undergraduate student in the Department of Aeronautics, MIT was supported as a summer intern (May – July 2000) under this ARO grant.

**ROCKWELL
SCIENTIFIC**

DELAMINATION DYNAMICS IN THROUGH-THICKNESS REINFORCED LAMINATES WITH APPLICATION TO DCB SPECIMEN

N. Sridhar

Rockwell Scientific
1049 Camino Dos Rios
Thousand Oaks, CA 91360, U.S.A.
Email: sridhar@rwsc.com
Phone: 805-373-4774

R. Massabò

Department of Civil and Environmental Engineering
McCormick School of Engineering and Applied Science
Northwestern University
Evanston, IL 60208
U.S.A.

B. N. Cox

Rockwell Scientific
1049 Camino Dos Rios
Thousand Oaks, CA 91360
U.S.A.

and

I. J. Beyerlein

Los Alamos National Laboratory
Los Alamos, NM 87545
U.S.A.

ABSTRACT

Bridged crack models using beam theory formulations have proved to be effective in modeling quasi-static delamination crack growth under large scale bridging conditions in through-thickness reinforced structures. In this paper, beam theory is used to study dynamic mode I crack propagation in through-thickness reinforced laminate structures. In particular, steady state dynamic crack growth for a Double Cantilever Beam (DCB) loaded with a flying wedge is examined. The steady state crack propagation characteristics are mapped out in terms of controllable loading and material parameters including the crack velocity and the properties of the through-thickness reinforcement. For small crack velocities, the through-thickness reinforcement considerably enhances the delamination resistance of the structure. At higher velocities, the kinetic energy term dominates the overall energetics and the relative effect of the reinforcement on increasing the delamination resistance is insignificant. The model suggests a simple fracture test for estimating the properties of the through-thickness reinforcement under dynamic loading conditions.

1.   Introduction

Through-thickness reinforcement of various kinds, including stitched or woven continuous fiber tows and metallic or fibrous short rods, has been developed to address the delamination problem in structural composite laminates.   Substantial experimental evidence shows that through-thickness reinforcement dramatically alters the delamination characteristics for the better under both static and dynamic loading conditions (see [1] for review). For static loading, a fundamental theory based on observations of essential mechanisms is now mostly in place [2-18].   The mechanics of crack bridging by the through-thickness tows has been mapped out, with governing length scales and material parameters identified [4,10,7,14,16-18]. With the correct fracture mechanics, a practical engineering approach to deducing the constitutive relations for through-thickness reinforcement from engineering tests has been demonstrated, which is a major step towards certifiable test procedures and design standards [13].

Interesting large-scale bridging effects arise in through-thickness reinforced delamination cracks under static mixed mode loading conditions [8,11].   For instance, in a mixed mode bending specimen, which can be thought of as a combination of double cantilever beam (DCB) and end notched flexure (ENF) specimens, the crack commences growth in mixed mode, but may after some growth reach a configuration for which the mode I energy release rate vanishes. When this happens, subsequent growth must be in pure mode II.   Crack profile calculations and experimental observations show that fracture surface contact occurs both at the crack tip and possibly at other points along the crack wake.   Models of the fracture problem in which interpenetration of the fracture surfaces are not barred (a modelling fiction) predict a smoothly oscillating crack opening profile.   The oscillations can be regarded as analogous to those found in the deflection of a point-loaded beam on an elastic foundation, which is a classical engineering problem (e.g., [18]). The characteristic length of the oscillations depends on the traction relation and can be smaller than or comparable to the bridged zone length in cases of practical interest [8,11].

Since large bridging zones have such a strong influence on the character of delamination in static cases, the question naturally arises of what their effect may be in dynamic delamination, with

particular attention to demarcating the classes of oscillating and non-oscillating solutions that may exist and identifying regimes where bridging effects are weak and strong in a given material. The influence of cohesive/bridging mechanisms on the dynamic fracture process has been investigated previously (see [20-28] among the others). The model in [28], in particular, analyses dynamic crack propagation in a composite material characterised by two distinct toughening mechanisms, similar to the composite laminates treated in this paper. The model, however, refers to an infinite medium and to steady-state propagation of the crack (leading to small scale bridging). Here mode I dynamic delamination in the presence of large bridging zones, e.g., of through-thickness reinforcement, is studied by means of beam theory.

Dynamic delamination without through-thickness reinforcement has already been studied quite extensively using beam theory (see, e.g., [29-34] among the earlier works). Despite the simplifications imposed on the stress field, comparison with finite element calculations shows that the dominant dynamic features are still retained, while the problem remains tractable by analytical methods [34]. Beam models that are successful in at least some domain have been formulated with the two arms of the DCB specimen represented as either Euler-Bernoulli or Timoshenko beams with different boundary conditions at the crack tip or ahead of it [32-34]. Kanninen's model [34] introduces an elastic foundation of shear and rotational springs that connect the two arms of the specimen ahead of the crack tip. The crack grows by continuous removal of the springs from the notch tip. While this device presages the fields of crack bridging to be studied here, Kanninen's work is strictly limited to the regime where the total toughness or work of fracture of the system is a material constant, independent of crack length. More complex crack characteristics will be demonstrated here, under large scale bridging conditions.

The paper examines dynamic delamination for through-thickness reinforced structures and identifies crack propagation characteristics for the mode I case. The bridging action of the through-thickness reinforcement is represented by a distribution of tractions acting along the fracture surfaces opposing their relative displacement. The tractions are coupled to the crack displacement by a bridging relation, which embodies the mechanism of load transfer from the reinforcement to the surrounding material. With the results of the analysis, the mechanics of crack growth for a through-thickness reinforced DCB specimen loaded by a flying wedge is

examined. This specimen offers a relatively simple experiment for studying the role of through-thickness reinforcement on dynamic crack propagation. A steady state situation can exist, i.e., one in which the configuration of the structure and the traction distribution are time invariant in a reference frame translating with the crack tip, when the crack tip is moving at a constant speed. (For a classical DCB specimen, with the load always applied at a fixed location, a steady state condition is not readily attained and unsteady crack growth would be more representative. But for a DCB loaded by a flying wedge, where the point of contact moves along the specimen, the steady state is likely to be found more easily in experiments.) The existence of steady state condition greatly simplifies the analysis. Non-steady state crack growth, including transient response to a newly applied load will be studied elsewhere.

2.0   Beam Theories of a Double Cantilever Beam

From Figure 1a, the equations of motion for the beam element in the crack wake of a DCB specimen are:

$$\frac{\partial Q}{\partial x} - p(w,t) = \rho\, h\, \frac{\partial^2 w}{\partial t^2} \quad , \tag{1a}$$

$$\frac{\partial M}{\partial x} - Q = \rho\, I\, \frac{\partial^2 \phi}{\partial t^2} \quad , \tag{1b}$$

where $w(x,t)$ is the transverse displacement of the neutral plane, which is also half the crack opening displacement, $\phi(x,t)$ is the clockwise rotation of the cross-section, t is time, Q is the shear force per unit width, M is the bending moment per unit width, $2h$ is the total thickness of the DCB specimen, ρ is the material density, $I\,(= h^3/12)$ is the moment of inertia of the beam element per unit width, and $p(w,t)$ is the bridging traction corresponding to the opening mode. Since attention is focused on the mode I case, the bridging traction p can be assumed to depend only on time and the opening displacement w.

2.1   Timoshenko Beam

For a Timoshenko beam, the constitutive equations are:

$$Q = \kappa G \, h \left(\phi + \frac{\partial w}{\partial x} \right) \quad , \tag{2a}$$

$$M = EI \frac{\partial \phi}{\partial x} \quad , \tag{2b}$$

where the dimensionless shear coefficient $\kappa = 5/6$ for a rectangular cross-section, G is the shear modulus and E is Young's modulus.

The equations of motion together with the constitutive equations yield:

$$\frac{\partial^2 w}{\partial x^2} + \frac{\partial \phi}{\partial x} - \frac{p(w,t)}{\kappa G h} = \frac{\rho}{\kappa G} \frac{\partial^2 w}{\partial t^2} \quad , \tag{3a}$$

$$\frac{\partial^2 \phi}{\partial x^2} - \frac{12 \kappa G}{E h^2} \left(\phi + \frac{\partial w}{\partial x} \right) = \frac{\rho}{E} \frac{\partial^2 \phi}{\partial t^2} \quad . \tag{3b}$$

Under steady state cracking, $f(x,t) = f(X)$ where $X = x - v\,t$ and v is the (constant) velocity of the crack tip. The above equations then reduce to:

$$\frac{\partial^2 w}{\partial X^2} + \frac{\partial \phi}{\partial X} - \frac{p(w,X)}{\kappa G h} = \frac{v^2}{c_l^2} \frac{E}{\kappa G} \frac{\partial^2 w}{\partial X^2} \quad , \tag{4a}$$

$$\frac{\partial^2 \phi}{\partial X^2} - \frac{12 \kappa G}{E h^2} \left(\phi + \frac{\partial w}{\partial X} \right) = \frac{v^2}{c_l^2} \frac{\partial^2 \phi}{\partial X^2} \quad , \tag{4b}$$

where $c_l^2 = E / \rho$.

2.2 Euler-Bernoulli Beam

For an Euler-Bernoulli beam, the shear deformation is considered to be negligible ($\gamma \to 0$) and hence $\phi = \gamma - \partial w / \partial x \approx -\partial w / \partial x$. In addition, the rotational inertia is considered to be small and ignored. The only independent field quantity is the opening displacement w. The constitutive equation (2b) becomes:

$$M = - EI \frac{\partial^2 w}{\partial x^2} \qquad , \qquad (5)$$

and equation (1b) reduces to:

$$\frac{\partial M}{\partial x} - Q = 0 \qquad . \qquad (6)$$

Combining Eqs. (1a), (5) and (6) yields:

$$\frac{\partial^4 w}{\partial x^4} + \frac{12\,\rho}{E\,h^2} \frac{\partial^2 w}{\partial t^2} + \frac{12}{E\,h^3} p(w,t) = 0 \qquad . \qquad (7)$$

Under steady state cracking

$$\frac{\partial^4 w}{\partial X^4} + \frac{12}{h^2} \frac{v^2}{c_l^2} \frac{\partial^2 w}{\partial X^2} + \frac{12}{E\,h^3} p(w,X) = 0 \qquad , \qquad (8)$$

where $X = x - v\,t$ and v is the (constant) velocity of the crack tip.

2.3   Displacement Characteristics for a Linear Bridging Relation

Consider a rate independent linear bridging relation:

$$p(w, X) = p_0 + \beta w \qquad . \qquad (9a)$$

A softening linear relation ($p_0 > 0$, $\beta < 0$) is known to be realistic for large displacements for short rods or z-pins under mode I static loading [35]. An initial hardening response, during which the rod is progressively debonded from the laminate, is confined to relatively small displacements. Softening occurs after the whole rod has debonded, when the embedded length of the rod and therefore frictional resistance decrease to zero as the rod is pulled out of the laminate.   In contrast, mode I tests on stitched laminates indicate an approximately linear hardening relation ($p_0 > 0$, $\beta > 0$), which peaks when the stitch breaks and then falls relatively rapidly to zero [36]. The difference from the case of rod pullout arises because of the mechanics of stitch deformation – larger displacements arise in the hardening phase for a stitch, because the stitch can be drawn down into the composite from the outer surface of the laminate before it breaks.   In steady state dynamic loading the bridging tractions could also depend on the crack velocity and the crack displacement gradient. This dependence is under investigation [37] and is not considered here. The dimensionless quantity

$$S = 12 \beta h / E \qquad (9b)$$

is a convenient indicator of the stiffness of the bridging relation**.** For a hardening bridging relation $S > 0$ and for softening $S < 0$.

In the results that follow, the length variables are non-dimensionalized by h, the laminate half thickness ($w \equiv h W$ and $X \equiv h \xi$). For such a linear bridging relation the opening displacement in Equation 9 obeys:

$$\frac{\partial^4 W}{\partial \xi^4} + V^2 \frac{\partial^2 W}{\partial \xi^2} + B^2 W + P_0^2 = 0 \qquad . \qquad \text{(10a)}$$

The clockwise rotation ϕ for the Timoshenko beam obeys:

$$\frac{\partial \phi}{\partial \xi} = \frac{(p_0 + \beta h W)}{\kappa G} - \left(1 - \frac{E v^2}{\kappa G c_l^2}\right) \frac{\partial^2 W}{\partial \xi^2} \qquad . \qquad \text{(10b)}$$

The coefficients V, B, and P_0 in Equation 10a are:

For the Timoshenko beam:

$$V^2 = \frac{1}{\left(\dfrac{\kappa G}{E} - \dfrac{v^2}{c_l^2}\right)} \left[12 \frac{\kappa G}{E} \frac{v^2/c_l^2}{(1 - v^2/c_l^2)} - \frac{S}{12} \right] \qquad ; \qquad \text{(11a)}$$

$$B^2 = S \frac{\kappa G/E}{\left(1 - \dfrac{v^2}{c_l^2}\right)\left(\dfrac{\kappa G}{E} - \dfrac{v^2}{c_l^2}\right)} \qquad ; \qquad \text{(11b)}$$

$$P_0^2 = \frac{\kappa G/E}{\left(1 - \dfrac{v^2}{c_l^2}\right)\left(\dfrac{\kappa G}{E} - \dfrac{v^2}{c_l^2}\right)} \frac{12 p_0}{E} \qquad ; \qquad \text{(11c)}$$

For the Euler-Bernoulli (E-B) beam:

$$V^2 = 12 \, v^2 / c_l^2 ; \qquad\qquad B^2 = S = \frac{12 \beta h}{E} ; \qquad P_0^2 = \frac{12 \, p_0}{E} ; \qquad \text{(12)}$$

Table 1 shows representative values of these dimensionless groups and the material parameters they contain for stitched carbon epoxy laminates with unidirectional in-plane reinforcement or quasi-isotropic lay-ups.

Table 1. Typical parameters for stitched carbon/epoxy composites.

Parameter	Typical values
Longitudinal wave speed of laminate (c_l)	2000 – 8000 m/sec
Elastic stiffness of laminate (E)	50 – 150 Gpa
Shear stiffness of laminate (G)	5 – 10 Gpa
Thickness of laminate (h)	2 – 15 mm [a]
Through-thickness bridging stiffness (β)	50 – 1000 MPa/mm [a]
Through-thickness bridging parameter (p_0)	0 – 20 MPa
Critical crack opening displacement (w_c)	0.02 – 1.5 mm [a,b]
Inter-laminar fracture energy (G_0)	0.1 – 1.0 kJ / m^2
W_c	0.01 – 0.1 [b]
$\overline{G}_0 = 12G_0 /(E\,h)$	$10^{-7} – 10^{-5}$
$\Delta\overline{G}_b = 2P_0^2 W_c + B^2 W_c^2$	$0.0 – 10^{-3}$
$\kappa G/E$	0.03 – 0.
$S = 12\beta h/\mathrm{E}$	0.0025 – 1.2
Euler-Bernoulli Beam $B = \sqrt{12\beta h/E}$	0.05 – 0.6
$P_0 = \sqrt{12\,p_0 /E}$	0.0 – 0.1
Timoshenko Beam $B = \sqrt{12\beta h/E}\cdot\eta[v,R]$	0.05 – 0.6 [c]
$P_0 = \sqrt{12p_0/E}\cdot\eta[v,R]$	0.0 – 0.1 [c]

[a] For a fixed area fraction of stitching, the critical displacement and the laminate thickness and the reciprocal of the stiffness parameter tend to be approximately proportional.
[b] Critical displacements at the high end of the stated range are expected when the surface segments of a stitch are pulled down into the laminate (toward the fracture plane) by tension in the through-thickness segment [14].
[c] For a Timoshenko beam, the values of B and P_0 are functions of V (following Eq. (11), with the short notation η introduced here). The ranges shown in the table are those for $V = 0$, for which the expressions for B and P_0 reduce to those for the Euler-Bernoulli beam. For stitched laminates, $\beta > 0$ and therefore B is real.

The general solution to equation 10 is:

$$W(\xi) = -\frac{P_0^2}{B^2} + K_1 e^{-\sqrt{-\frac{V^2}{2} - \frac{1}{2}\sqrt{V^4 - 4B^2}}\,\xi} + K_2 e^{+\sqrt{-\frac{V^2}{2} - \frac{1}{2}\sqrt{V^4 - 4B^2}}\,\xi}$$
$$+ K_3 e^{-\sqrt{-\frac{V^2}{2} + \frac{1}{2}\sqrt{V^4 - 4B^2}}\,\xi} + K_4 e^{+\sqrt{-\frac{V^2}{2} + \frac{1}{2}\sqrt{V^4 - 4B^2}}\,\xi} \quad . \tag{13}$$

In the limit $v \to 0$, this reduces to the result for the static case obtained by Massabò and Cox [8]. Whether B and V are real or pure imaginary and which is larger in magnitude determine the qualitative nature of the displacement profile, especially the possibility of oscillations. The possible cases are as follows. The functions

$$f_1 = \frac{S}{12^2} \frac{E}{\kappa G} \left(1 - \frac{v^2}{c_l^2} \right) - \frac{v^2}{c_l^2} \qquad \text{and} \qquad f_2 = \frac{1}{6} \sqrt{S \frac{E}{\kappa G} \left(1 - \frac{v^2}{c_l^2} \right) \left(\frac{\kappa G}{E} - \frac{v^2}{c_l^2} \right)} \qquad (14)$$

and the two real parameters n_1 and n_2, which depend on V^2 and B^2, will appear in conditions for the solutions for the Timoshenko beam.

- Case 1: $B^2 > 0$, $V^2 < 0$ and $V^4 > 4B^2$ => hyperbolic functions

$$W(\xi) = -\frac{P_0^2}{B^2} + K_1 Cosh(n_1 \xi) + K_2 Sinh(n_1 \xi) + K_3 Cosh(n_2 \xi) + K_4 Sinh(n_2 \xi), \quad (15a)$$

$$n_1 = \sqrt{\left| V^2 \right| + \sqrt{V^4 - 4B^2}} / \sqrt{2} \text{ and } n_2 = \sqrt{\left| V^2 \right| - \sqrt{V^4 - 4B^2}} / \sqrt{2} \qquad . \qquad (15b)$$

For the Timoshenko beam, the conditions for this case reduce to

$$S \left(\frac{\kappa G}{E} - \frac{v^2}{c_l^2} \right) > 0 \quad \text{and} \quad f_1 > f_2 \qquad (15c)$$

The second of these conditions cannot be satisfied if $S < 0$ and therefore this case is obtained only in that part of the domain $\{S > 0, \kappa G/E > v^2/c_L^2\}$ in which $f_1 > f_2$.

For the E-B beam, the conditions for Case 1 are never satisfied.

- Case 2: $B^2 > 0$, $V^2 > 0$ and $V^4 > 4B^2$ => trigonometric functions

$$W(\xi) = -\frac{P_0^2}{B^2} + K_1 Cos(n_1\xi) + K_2 Sin(n_1\xi) + K_3 Cos(n_2\xi) + K_4 Sin(n_2\xi), \qquad (16a)$$

$$n_1 = \sqrt{V^2 + \sqrt{V^4 - 4B^2}} / \sqrt{2} \text{ and } n_2 = \sqrt{V^2 - \sqrt{V^4 - 4B^2}} / \sqrt{2} \qquad . \qquad (16b)$$

For the Timoshenko beam, the conditions for this case reduce to

$$S\left(\frac{\kappa G}{E} - \frac{v^2}{c_l^2}\right) > 0 \quad \text{and} \quad -f_1 > f_2 \qquad (16c)$$

When $S < 0$, the second of these conditions is satisfied for all $v/c_L > \kappa G/E$.

For the E-B beam, the conditions for this case reduce to

$$0 \le S \le 36\frac{v^4}{c_l^4} \qquad (16d)$$

- Case 3: $B^2 < 0 \Rightarrow$ sums of trigonometric and hyperbolic functions

$$W(\xi) = -\frac{P_0^2}{B^2} + K_1 Cos(n_1\xi) + K_2 Sin(n_1\xi) + K_3 Cosh(n_2\xi) + K_4 Sinh(n_2\xi), \qquad (17a)$$

$$n_1 = \sqrt{V^2 + \sqrt{V^4 - 4B^2}} / \sqrt{2} \text{ and } n_2 = \sqrt{-V^2 + \sqrt{V^4 - 4B^2}} / \sqrt{2} \qquad . \qquad (17b)$$

For the Timoshenko beam, the conditions for this case reduce to

$$S\left(\frac{\kappa G}{E} - \frac{v^2}{c_l^2}\right) < 0 \qquad (17c)$$

together with $f_1^2 > f_2^2$. The latter condition is easily seen to be obeyed on the boundaries of the two domains $\{S < 0,\ \kappa G/E > v^2/c_L^2\}$ and $\{S > 0,\ \kappa G/E < v^2/c_L^2\}$. Furthermore, neither $\partial(f_1^2 - f_2^2)/\partial S$ nor $\partial(f_1^2 - f_2^2)/\partial v$ possesses zeroes within either domain. Therefore, the condition $f_1^2 > f_2^2$ must always hold in the domains within which Eq. (17c) is satisfied and need not be stated as a separate condition.

For the E-B beam, the conditions for this case reduce to

$$S < 0 \qquad . \qquad (17d)$$

Case 4: $B^2 > 0$ and $V^4 < 4B^2 \Rightarrow$ products of trigonometric and hyperbolic functions

$$
\begin{aligned}
W(\xi) \;=\; & -\frac{P_0^2}{B^2} + K_1\, Cosh(\,n_1\,\xi\,)Cos(\,n_2\,\xi\,) + K_2\, Cosh(\,n_1\,\xi\,)Sin(\,n_2\,\xi\,), \\
& + K_3\, Sinh(\,n_1\,\xi\,)Cos(\,n_2\,\xi\,) + K_4\, Sinh(\,n_1\,\xi\,)Sin(\,n_2\,\xi\,)
\end{aligned}
\qquad (18a)
$$

$$n_1 = \sqrt{2B - V^2}\,/2 \quad \text{and} \quad n_2 = \sqrt{2B + V^2}\,/2 \qquad . \qquad (18b)$$

For the Timoshenko beam, the conditions for this case reduce to

$$S\left(\frac{\kappa G}{E} - \frac{v^2}{c_l^2}\right) > 0 \quad \text{and} \quad f_1^2 < f_2^2 \qquad (18c)$$

The second of these conditions can only be satisfied in the domain $\{S > 0,\ \kappa G/E > v^2/c_L^2\}$, since the function $f_1^2 - f_2^2$ is positive on the boundaries of the domain $\{S < 0,\ \kappa G/E < v^2/c_L^2\}$ and neither $\partial(f_1^2 - f_2^2)/\partial S$ nor $\partial(f_1^2 - f_2^2)/\partial v$ possesses zeroes within this domain.

For the E-B beam, the conditions for this case reduce to

$$S \geq 36 \frac{v^4}{c_l^4} \qquad . \tag{18d}$$

The possible forms of the solution for the crack profile are summarized for the Timoshenko and Euler-Bernoulli beams in Figs. 2.a and 2.b where the boundaries of the different domains are controlled by the quantity $\kappa G/E$. The curved boundary (drawn schematically) surrounding the domain labeled "TH" in Fig. 2a corresponds to the condition $f_1^2 = f_2^2$, i.e.,

$$S = \frac{2\kappa G/E - v^2/c_l^2 \pm 2\sqrt{\kappa G/E\left(\kappa G/E - v^2/c_l^2\right)}}{1 - v^2/c_l^2} \frac{12^2 \kappa G}{E} \tag{19}$$

For negligible shear deformations ($\kappa G/E \rightarrow \infty$), Eq. (18c), which defines the domain TH, becomes $S \geq 36/(1 - v^2/c_l^2)v^4/c_l^4$ and the map of Fig. 2a becomes similar to that of Fig. 2b for an Euler-Bernoulli beam (where the domain TH is defined by Eq. (18d), $S \geq 36 v^4/c_l^4$). The term $(1 - v^2/c_l^2)$ in the modified Eq. (18c) accounts for the rotational inertia effects.

Oscillations in the profile are possible when the solution contains trigonometric functions (domains T, TH and T+H in Figure 2). This is always the case for the Euler-Bernoulli beam. For the Timoshenko beam, the conditions for the occurrence of oscillations depend on the crack velocity, the anisotropy of the beam, and the stiffness of the bridging mechanism, represented by S. For typical material parameters, transitions from oscillating to non-oscillating solutions (region H in Fig. 2a) could be observed at attainable velocities. For example, for stitched polymer composite laminates, $S > 0$ and the magnitude of S (0.0025 – 1.2) is typically less than $4(12\kappa G/E)^2$ (0.52 - 23), where $\kappa G/E$ is the anisotropy parameter (Table 1). Therefore, parameters for a Timoshenko beam will lie near the boundary of region H in Fig. 2a for velocities $v/c_l < (\kappa G/E)^{1/2} \approx 0.2 – 0.4$ and the boundary may well be crossed as the velocity changes.

While oscillations appear to be the common case in the maps of Fig. 2, other conditions can intervene, especially a boundary condition corresponding to the rupture of the through-thickness

reinforcement. Such rupture (failure of the bridging mechanism) will limit the length of the bridged zone, perhaps to a length that is less than the wavelength of the oscillations.

Oscillations would imply the presence of regions of contact along the delamination surfaces in a simple specimen. Oscillations following the functional forms derived here (with negative displacements) could be observed in a specimen in which the crack runs along a compliant layer of thickness small compared to the specimen thickness, h, but large compared to the amplitude of the crack displacement. In the absence of a compliant layer, strong resistance to material interpenetration must modify the profile, but the possibility of multiple humps of positive opening displacement is suggested.

In the limit case $v \to 0$, the behavior of the Timoshenko beam reduces to that already derived for the static problem [8].

3.   Wedge-Loaded Double Cantilever Beam

The arbitrary constants K_1, K_2, K_3, and K_4 that appear in the displacement profile function, Eq. 13, are defined in any problem through boundary and continuity conditions. When the constants are known, all other characteristics of the fracture problem can be determined, such as the critical load for crack propagation, the length of the bridging zone when the bridging ligaments have finite strength, and various contributions to the energy of fracture.

Here the problem of a double cantilever beam (DCB) specimen loaded dynamically by a flying wedge is studied. Solutions are sought where the wedge and the crack translate together at constant velocity, v, with a time-invariant crack configuration (steady state configuration). This special case offers considerable insight into the dynamic fracture process and also offers a relatively simple experimental approach for future study (Fig. 1b). The beam arms are modeled as Euler Bernoulli beams, so that both shear deformation and rotational inertia are ignored. Therefore, the constants V^2, B^2, and $P_0{}^2$ referred to hereafter are those presented in Eq. 12, so that V, $B^2 = S$, and P_0 are real and have simple interpretations as the normalized velocity, bridging

stiffness, and bridging traction at zero displacement, respectively. Without loss of generality, $V > 0$, while $P_0 > 0$ for physical reasons, and the sign of $B^2 = S$ may be positive or negative. The beam arms are assumed to be built-in at the crack tip so that the influence of the elasticity of the material ahead of the crack tip is neglected. This assumption is expected not to modify the characteristics of fracture provided the beam arms are long enough. The beams are assumed to be axially inextensible.

In Fig. 1b, 2α is the wedge angle, l is the distance between the wedge and the crack tip and a_0 is the length of the bridging zone. In non-dimensional form, $l \equiv h\,L$, and $a_0 \equiv h\,A_0$. The wedge angle is assumed to be small and hence small deflection beam theory should be sufficient to model the problem. Due to symmetry, only the top half of the DCB specimen needs to be considered. The bridging constituent is assumed to possess the linear bridging relationship of Eqn. 9.

3.1   Deflection Profile

The deflection profile of the cantilever beam due to the wedge loading is governed by Eq. 10a for the bridged portion of the crack. For the unbridged portion, the deflection profile ($w_u \equiv h\,W_u$) is obtained by setting $B = P_0 = 0$ in Eq.10a. Therefore:

$$\frac{\partial^4 W_u}{\partial \xi^4} + V^2\,\frac{\partial^2 W_u}{\partial \xi^2} = 0 \qquad\qquad \text{for } (-L \le \xi \le -A_0) \quad , \qquad (20a)$$

$$\frac{\partial^4 W}{\partial \xi^4} + V^2\,\frac{\partial^2 W}{\partial \xi^2} + B^2 W + P_0^2 = 0 \qquad\qquad \text{for } (-A_0 < \xi \le 0) \qquad . \qquad (20b)$$

The relevant boundary conditions are:

$$W(\xi = 0) = 0 \qquad\qquad\qquad\qquad\qquad , \qquad (21a)$$

$$W^{'}(\xi = 0) = 0 \qquad\qquad\qquad\qquad\qquad , \qquad (21b)$$

$$W_u^{'}(\xi = -L) = -\alpha \qquad , \qquad (21c)$$

$$W_u^{''}(\xi = -L) = -\frac{\mu}{2} W_u^{'''}(\xi = -L) \qquad , \qquad (21d)$$

where μ is the coefficient of friction between the wedge and the beam arm and the derivative is with respect to ξ. Equations 21a and 21b express the boundary conditions associated with the crack tip, and equations 21c and 21d express the boundary conditions at the contact point between the wedge and the DCB specimen. Using a simplified approach, the net effect of friction between the wedge and the beam has been represented by a force parallel to the wedge surface acting at the contact point and linked through μ to the reaction force of the wedge on the beam. The frictional force gives rise to a bending moment at the contact point which is zero in the absence of friction ($\mu = 0$).

The deflection profiles should also satisfy the continuity conditions at the end of the bridging zone ($\xi = -A_0$). The continuity conditions are:

$$W(\xi = -A_0) = W_u(\xi = -A_0), \qquad W^{'}(\xi = -A_0) = W_u^{'}(\xi = -A_0),$$

$$W^{''}(\xi = -A_0) = W_u^{''}(\xi = -A_0), \qquad W^{'''}(\xi = -A_0) = W_u^{'''}(\xi = -A_0). \qquad (22)$$

The governing equation (20), which has the general solution Eq. (13) in the domain $-A_0 < \xi \leq 0$, together with the boundary conditions (21) and the continuity conditions (22) determine the deflection profile of the beam. The problem is closed by setting three further conditions to determine A_0, L, and the equilibrium value, F, of the force per unit width acting on the wedge.

3.2   Determination of A_0, L and F

At the end of the bridging zone, the crack displacement must be the critical crack opening displacement, $w_c \equiv h\,W_c$, for failure of the bridging ligament:

$$W(\xi = -A_0) = W_c \qquad . \qquad (23)$$

The existence of the critical displacement and its attainment within the domain $-L < \xi < 0$ are necessary conditions for a steady state solution to exist.

The curvature at the crack tip (or the bending moment per unit width M) is related to the energy released at the crack tip by application of the dynamic J integral (see [38]):

$$G_{Tip} = \frac{12}{Eh^3}\left[M_{\xi=0}\right]^2 = \frac{Eh}{12}\left(\left.\frac{\partial^2 W}{\partial \xi^2}\right|_{\xi=0}\right)^2 \qquad . \qquad (24)$$

For crack propagation $G_{Tip} = G_0$, where G_0 is the critical inter-laminar energy release rate (or the intrinsic toughness of the laminate without through-thickness reinforcement) and thus

$$W''(\xi = 0) = \sqrt{\overline{G_0}} = \sqrt{\frac{12\,G_0}{Eh}} \qquad , \qquad (25)$$

where $\overline{G_0} = 12G_0 /(Eh)$ is the normalised interlaminar fracture energy. Finally, from the requirement of force balance for the wedge, the normalised force $\overline{F} = 12F /(Eh)$, required for driving the wedge is:

$$\overline{F} = \frac{12F}{Eh} = 2(\mu + \alpha)\,W_u'''(\xi = -L) \qquad . \qquad (26)$$

Equations 23, 25 and 26 determine A_0, L and F.

3.3   Crack Energetics

The energy release rate, G_{Total} determined through the total energy balance is:

$$G_{Total} = \left(\frac{\partial U_{ext}}{\partial a} - \frac{\partial U_s}{\partial a} - \frac{\partial U_k}{\partial a} - \frac{\partial U_d}{\partial a} \right) \qquad , \qquad (27)$$

where U_{ext} is the work done by the applied load, U_s is the strain energy, U_k is the kinetic energy, U_d is the dissipated energy and a is the crack length. The energy terms U_{ext}, U_s , U_k and U_d are defined per unit width of the beam. For steady state crack extension, these quantities are:

$$\frac{\partial U_{ext}}{\partial a} = \frac{1}{v} F \ v = F \qquad , \qquad (28a)$$

$$\frac{\partial U_s}{\partial a} = -\frac{12(M_{\xi=-L})^2}{E \ h^3} \qquad , \qquad (28b)$$

$$\frac{\partial U_k}{\partial a} = 2 \ \frac{1}{v} \frac{\partial}{\partial t} \left(\frac{1}{2} m \ v_n^2 \right) = \ \rho h v^2 \ Sin^2(\alpha) \ \approx \ \rho h v^2 \alpha^2 \qquad , \qquad (28c)$$

$$\frac{\partial U_d}{\partial a} = -2\mu Q\big|_{(\xi=-L)} Cos(\alpha) \approx \frac{\mu}{(\alpha+\mu)} F \qquad , \qquad (28d)$$

where m is the mass in the wake behind the wedge, v_n is velocity normal to the beam axis, F is the equilibrium force required to drive the wedge at the constant velocity v, and Q is the transverse shear force in the beam. Equation (28b) accounts for the strain energy released by the material as it slides up the wedge beyond the contact point. This term is not zero in the presence of friction because of the discontinuity in the bending moment and the consequent discontinuity in the strain energy density at the contact point. In the absence of friction, the strain energy density in the unbridged region is a quadratic function of ξ which vanishes at $\xi = -L$, since $M_{\xi=-L} = 0$ and the shear deformations are neglected, and therefore $\partial U_s/\partial a$ is zero. The equality between Q and F in Eq. (28d) follows by balancing forces on the wedge.

The available energy for crack extension is therefore,

$$G_{Total} = \left(\frac{\alpha}{\alpha+\mu}\right) F + \frac{3}{4(1+\alpha/\mu)^2} \frac{F^2}{Eh} - \rho h v^2 \alpha^2 \qquad . \quad (29)$$

Here the second term, which introduces a non-linear dependence on F, results from the consideration of the energy associated with relief of the bending moment at the load point, as described in the previous paragraph. Since its magnitude relative to the first term varies as F/Eh, it is always small, but it is necessary to obtain complete consistency. In the absence of crack bridging, $G_{Total} = G_{Tip} = G_0$. However, with crack bridging, $\Delta G_b = G_{Total} - G_0 \neq 0$. The energy difference, ΔG_b, is the extra work done in fracturing the bridging ligaments. For the steady state configuration and bridging tractions that do not depend explicitly on time (or rate), application of the dynamic J-integral yields:

$$G_{Total} = G_0 + \Delta G_b = G_0 + 2\int_0^{w_c} p(w)\,dw \qquad , \qquad (30)$$

where $p(w)$ is the bridging relation. The result of Eq. (30) holds only if unloading does not occur in the bridging mechanism, i.e., if, for an increasing or hardening bridging relation ($\partial p/\partial w > 0$), w is a monotonically increasing function of $-\xi$. This restriction can come into play in cases of interest.

Equations 29 and 30 imply that the equilibrium wedge force that sustains the steady state configuration is:

$$F = \frac{Eh}{12}\left(\frac{8\alpha(\alpha+\mu)}{\mu^2}\right)\left(\sqrt{1 + \frac{3\mu^2}{Eh\alpha^2}\left(G_0 + 2\int_0^{w_c} p(w)\,dw + \rho h v^2 \alpha^2\right)} - 1\right). \quad (31a)$$

In terms of the normalized parameters of the linear relation (Eq. (12)) the force is:

$$\overline{F} = \frac{8\alpha(\alpha+\mu)}{\mu^2}\left(\sqrt{1 + (\overline{G}_0 + \Delta\overline{G}_b)\frac{\mu^2}{4\alpha^2} + \frac{\mu^2 V^2}{4}} - 1\right) \quad , \qquad (31b)$$

which in the case of no friction, $\mu = 0$, becomes:

$$\overline{F} = \left(V^2\alpha^2 + \overline{G}_0 + \Delta\overline{G}_b\right) \quad , \qquad (31c)$$

where $\Delta\overline{G}_b = 2P_0^2 W_c + B^2 W_c^2$ for the linear bridging relation examined here. As expected, equations (31a,b,c) show that the force required for driving the wedge at a constant velocity does not depend on the details of the bridging traction relation but only on the area beneath the curve ΔG_b. Moreover, the force F increases as the square of the velocity, reflecting the contribution of the kinetic energy of the beam arms.

The equilibrium force F can alternatively be determined by considering force equilibrium on the wedge, but this requires knowledge of the shear force at $\xi = -L$ and therefore of the displacement profile, W (equation 26). The availability of the simpler energy-based result of Eq. (31) is a characteristic of the DCB geometry, the loading configuration (see also [39]), and the fact that the bridging tractions have been assumed to depend on the opening displacement only. If the bridging traction relation is explicitly time or rate dependent, as it will be in general dynamic cases (e.g., [37]), then Eq. (31) is inapplicable and the profile must be computed to solve for any aspect of the fracture process. The only dependence of the force, F, upon the wedge velocity in Eq. (31) is the quadratic term, $F \propto v^2$, which can be traced to the kinetic energy (i.e., the proportion of the total work done that must go to accelerating the beam arms). For a bridging relation that is time or rate dependent, more complicated relations between force and velocity will arise.

Figure 3 shows the variation of the equilibrium force, F, normalized by its value in the absence of bridging, F_u (Eq. (31b) with $\Delta\overline{G}_b = 0$), as a function of the normalized crack velocity, $\alpha V/\sqrt{\overline{G}_0}$ or $\alpha(v/c_l)\sqrt{G_0/Eh}$. The different curves correspond to different values of

the ratio $\Delta G_b/G_0$ and the normalized friction coefficient. The two set of curves (dashed and solid) define limit bounds for all possible solutions since they correspond to minimum and maximum values attainable in typical laminates. As the crack velocity increases, the normalized force decreases rapidly and approaches unity. Since the kinetic energy contribution to the equilibrium force increases with increasing velocity while other contributions do not increase, the equilibrium forces in the presence and absence of bridging must become asymptotically indistinguishable. Thus bridging has an important effect on crack dynamics only for small to moderate crack velocities. As $\Delta G_b/G_0$ increases at a fixed velocity, F increases, but the trends of Fig. 3 remain qualitatively unchanged. The kinetic energy dominates and bridging effects are small for all cases shown whenever the normalized velocity parameter $\alpha V / \sqrt{G_0}$ exceeds 10. For typical quasi-isotropic laminates of relatively low thickness, $h \approx 2\text{-}3$ mm, and $2\alpha = 10°$ this is true when $v/c_1 > 0.1$. For thick laminates the limit velocity will be lower.

Although energetics alone determine the equilibrium force for the DCB configuration (Eq. 31b), the bridging zone length A_0 and distance between the wedge and the crack tip L can only be found by solving the transcendental Eqs. 23 and 25 (which is equivalent to obtaining the full crack profile). Before numerical solutions for A_0 and L are presented, two limiting cases are identified, which provide a helpful framework for understanding the general case.

3.4   Small Scale Bridging and High Velocity Limits

If the crack is sufficiently long compared to the length of the bridging zone, the small scale bridging (SSB) limit can be approached, in which the profile of the unbridged portion of the crack becomes independent of the details of the profile in the bridging zone. In a general crack geometry, such as a crack in an infinite body, and for a non-steady state crack problem, such as a crack whose length grows in time, the SSB limit is also characterized by the work done against the bridging ligaments, ΔG_b, becoming independent of the crack length. The crack exhibits the augmented apparent tip toughness, $G_0 + \Delta G_b$. Thus the effect of the bridging zone can be represented in the SSB limit as a point process concentrated at the crack tip, leading to the formulation commonly referred to as Linear Elastic Fracture Mechanics (LEFM). In the case of

the DCB specimen and the steady-state crack configuration, the work done against the bridging ligaments is invariant with respect to the relative lengths of the bridging zone and the crack (Eq. 27), and so this condition cannot be an indicator of the SSB limit, but one can still search for the SSB limit in the behavior of the crack profile. Thus, in the SSB limit, defined as the limit in which the effect of bridging can be represented by a point process at the crack tip, the equilibrium length L_{ssb} should take a value determined by solving the unbridged problem (see Appendix A):

$$\sqrt{\overline{G_T}} \; = \; \alpha V \; \frac{(\; Sin(V L_{ssb}\;) - \dfrac{\mu V}{2} Cos(V L_{ssb}\;)\;)}{(1 - Cos(V L_{ssb}\;) - \dfrac{\mu V}{2} Sin(V L_{ssb}\;))} \qquad , \qquad (32a)$$

where the normalised total crack energy release rate $\overline{G_T} = \overline{G_0} + \Delta\overline{G_b} = 12(G_0 + \Delta G_b)/(E\,h)$ is:

$$\overline{G_T} = \overline{G_0} \; + 2P_0^2 W_c + B^2 W_c^2 \qquad . \qquad (32b)$$

In the absence of friction at the load point ($\mu = 0$), the equilibrium length, L, in the SSB limit becomes (Appendix A)

$$L_{ssb} = \frac{2}{V} Tan^{-1}\left[\frac{\alpha V}{\sqrt{\overline{G_0} + \Delta\overline{G_b}}}\right] \qquad . \qquad (32c)$$

The second limiting case is the high velocity limit that arises when the energy required to accelerate the beam arms during crack propagation, $\partial U_k / \partial a = h E \alpha^2 V^2 / 12$, dominates both the intrinsic fracture toughness, G_0, and the work required to break the bridging ligaments, ΔG_b. The crack profile in the high velocity limit becomes independent of G_0 and the bridging parameters; it can be derived from the profile for the SSB limit by setting $G_0 = \Delta G_b = 0$ (Appendix A). Thus, for example, the value of L in the high velocity limit, L_v, will be given by

$$L_V = \frac{1}{V}\left(\pi + Tan^{-1}\left(\frac{\mu V}{2}\right)\right) \qquad (V/\sqrt{\overline{G}_0 + \Delta\overline{G}_b} \to \infty) \quad , \qquad (33)$$

with the correct branch of $\tan^{-1}$ being that for which $L_v \to \pi/V$ when $\mu \to 0$.

3.5 Characteristics of Steady-State Crack Propagation

The following numerical examples refer exclusively to the case where bridging is characterized by a linear hardening bridging relation ($\beta > 0$ or $S = B^2 > 0$).

Figure 4 shows typical families of crack displacement profiles for four different crack speeds, including a nearly stationary crack ($V = 0.001$, which approaches the static limit), and values of the bridging parameters that might be representative of a stitched polymer laminate with a low intrinsic fracture toughness, G_0. The solid curves in both Figs. 4a and 4b are exact results, while the dashed curves in Fig. 4a and 4b show the approximations of SSB or the high velocity limit respectively. For all crack velocities examined, $V < \sqrt{2B}$ or $v^2/c_l^2 < \sqrt{\beta h/3E}$), Equation (18) predicts the crack opening displacement to be oscillatory with exponential decay. In all cases, the equilibrium distance L is such that the profiles are monotonically increasing functions of distance from the crack tip, ξ, i.e., no oscillations are observed (see Section 3.6).

The SSB limit provides profiles in rough agreement with the exact results at all velocities for the cases shown, but underestimates the equilibrium distance, L (Appendix A). Furthermore, the approximation worsens as the crack velocity increases. For the equilibrium conditions imposed by the constraint of steady state propagation, the SSB limit becomes usefully accurate only when the critical displacement, W_c, is small.

Figure 4b compares the exact profiles with estimates based on the high velocity limit (bridging and intrinsic toughness effects negligible – Appendix A). The two sets of curves are widely different at vanishing velocity (the static limit), being separated by nearly two orders of magnitude in the value of L; but as the relative velocity rises to even moderately high values,

e.g., $V = 0.2$ or $v/c_1 = 0.06$ in the case of Fig. 4b, the high velocity approximation approaches the exact results increasingly closely.

Figure 5 shows further details of the variations in the steady-state wedge-crack tip separation, L. The solid curves show exact results, the dashed curves the SSB approximation of Eq. (29c) and the thick dashed curve the high velocity limit of Eq. (33). In the figure L is normalised by its value, $L_u\big|_{v=0}$, for a unbridged crack with tip toughness, G_0, in the static limit ($V = 0$), given by Eq. (A.6a), and is plotted as a function of the velocity for a range of values of the bridging stiffness parameter, B. The values taken for the bridging parameters B, P_0, and W_c are again representative of a stitched laminate with a moderate value of G_0. The figure shows that L decreases monotonically with increasing velocity and with increasing bridging stiffness, B. Since P_0 and W_c are fixed in Fig. 5, increasing B leads to increasing the contribution to the toughness due to the bridging mechanisms, ΔG_b. The SSB approximation always under-predicts L, which can be expected from the equilibrium of moments – the distributed action of the bridging ligaments in the exact solution will offset a larger moment from the applied force and therefore imply a larger distance, L. The high velocity limit is always approached by any of the other curves as V increases. The velocity at which L approaches the limit to within any specified fractional error rises with the value of B, because higher B implies higher work, ΔG_b, to fracture the bridging ligaments (with other bridging parameters held fixed) and therefore higher velocities to achieve dominance of the kinetic energy.

Figure 6 shows the variation of the bridging zone length, A_0, with velocity for the same cases as in Fig. 5; with A_0 normalised by the zone length, $A_0^u\big|_{v=0}$, for an unbridged quasi-static crack ($V = 0$) in the limit that $B \to 0$ and $P_0 \to 0$. This limit can be obtained by setting $W(\xi = -A_0) = W_c$ in the profile of an unbridged crack, Eq. (A.1). The high velocity limit, i.e., in the absence of bridging or intrinsic toughness (Appendix A), is also shown by a dashed line. Consistently with the behaviour of L, A_0 is a monotonically decreasing function for increasing velocity or bridging stiffness. Once again, the high velocity limit is approached at a velocity whose value increases as B increases.

Calculations not reported in this paper have shown that increasing the wedge angle, α, or the interfacial friction, μ, at fixed velocity leads to larger values of L. Increasing α also leads to a reduction of the zone length, A_0 which, on the other hand, is relatively insensitive to μ.

As the velocity increases, the ratio A_0/L always increases monotonically from a non-zero value for the static case. This behavior, which is exemplified by Fig. 7a, follows directly from the numerical result that the opening displacement at the wedge loading point, $W(-L)$, is a monotonically decreasing function of velocity (see Figure 4a). A limit value of the crack velocity, which depends on material and geometrical parameters, corresponds to the condition A_0 $/L = 1$, where the bridging ligaments remain intact over the whole interval between the crack tip and the point of contact with the wedge. The limit velocity increases on increasing the wedge angle and the coefficient of friction. No meaningful solutions to the steady state crack problem exist above the limit velocity. For the material parameters assumed in the figure and a wedge angle of 7.5°, for instance, the limit velocity is $V = 0.235$ or $v/c_1 = 0.07$.

Figures 7b and 8 illustrate this behavior further. Figure 7b shows the ratio A_0/L as a function of the bridging stiffness parameter B. The ratio A_0/L increases, which favors the creation of a domain of forbidden velocities or the extension of an existing domain, as the critical displacement, W_c, or the bridging stiffness parameter, B, increases (Figs. 7a and 7b). In Figure 8 the maximum permissible value, W_c^{max}, of W_c for steady state solutions to exist is plotted as a function of the bridging stiffness parameter, B, for fixed values of other bridging parameters. The parameter W_c^{max} is the value for W_c above which $A_0 \geq L$. Stiffer bridging imposes more stringent upper bound on W_c, since it reduces the crack opening, W; higher values of P_0 or the crack velocity also reduce W_c^{max}. For low velocities, $V = 0.1 - 0.2$, W_c^{max} is well above the critical displacement of typical laminates (see Table 1) for all B considered and therefore steady state propagation is always possible. However, for $V = 1$, which roughly corresponds to the Rayleigh wave speed of a common quasi-isotropic laminate, and similarly for all $V > 0.5$, W_c^{max} is in the range of feasible critical displacements (see Table 1). In summary, a bounding velocity will exist and lie at an experimentally accessible value for many cases of interest.

3.6 Oscillations in the crack displacement profile

Another question of interest is the possibility of oscillations arising in the crack displacement profile for steady state solutions. In Euler-Bernoulli beams, equations (13), (16) and (18) predict a transition in the crack opening displacement from purely oscillatory to oscillatory with exponential decay on varying the crack velocity, with $V = \sqrt{2B}$ or $v^2/c_l^2 = \sqrt{\beta h / 3E}$ the transition value. Therefore oscillations will arise in the crack profile if $\xi_{ext} < L$, with ξ_{ext} being the distance behind the crack tip at which the displacement function has a first extremum, $\partial W / \partial \xi = 0$. If $\xi_{ext} < A_0$ the first extremum will be within the bridged zone and the solutions derived above will contain a physical inconsistency, in that the displacement at the end of the bridged zone, where stitch failure is presumed to occur at a critical opening, w_c, will not be the maximum displacement.

The condition for the onset of oscillations is illustrated in Fig. 9 for typical values of the material parameters. The lower pair of curves in Fig. 9 shows typical variations in the bridging zone size, A_0, as a function of W_c at fixed crack velocity, obtained by solving the system of equations (20-23) and (25). The upper pair of curves shows the distance behind the crack tip, ξ_{ext}, at which the displacement function has a first extremum, $\partial W / \partial \xi = 0$, where W is the displacement function found for the bridging zone. In each pair of curves, the solid line corresponds to $B = 0.1$ and the dashed line corresponds to $B = 0.2$. The vertical line, $W_c = W_c^{max}$, shows the cutoff value for W_c above which $A_0 \geq L$.   In the cases shown, the cutoff is reached before any oscillation (extremum) is found in the bridging zone. The limit configuration would be defined by the intersection of the upper and lower curves. This characteristic is common to all numerical solutions that have been surveyed. Thus conditions for oscillations in the displacement profile are apparently not readily achieved in the steady state configuration for linear bridging.

4.   CONCLUSIONS

The dynamic mode I cracking behavior of a symmetric laminate containing possibly large bridging zones, constituted, for example, of through-thickness reinforcement, has been analyzed by beam theory. The character of the displacement profile shows features similar to those in the analogous static loading problem, including the possibility of oscillations extending far into the crack wake. However, the details of the functional form of the profile, including the existence of oscillations, depend not only on the sign and magnitude of the bridging stiffness parameter, but also on the crack velocity.

Steady state solutions, i.e., crack configurations propagating invariantly at constant velocity, have been proven to exist for significant parameter domains for the particular problem of a Double Cantilever Beam (DCB) specimen loaded by a flying wedge. The steady state crack propagation characteristics have been mapped out in terms of controllable loading and material parameters, including the wedge angle, the interlaminar fracture energy, and the properties of the through-thickness reinforcement. Interesting trends include the following.

For even moderately large crack velocities, typically $\alpha V / \sqrt{G_0} > 10$, kinetic energy dominates the fracture process and the relative effect of both the bridging contribution of the reinforcement and the intrinsic fracture toughness of the laminate are small. In typical quasi-isotropic laminates reinforced by through-thickness stitching this occurs when $v/c_1 > 0.1$. Our calculations and the diagram of Figure 4b show that in this limit, the crack profile is well estimated by the high velocity limit (absence of bridging and intrinsic toughness).

For small to moderate crack velocities, typically $\alpha V / \sqrt{G_0} < 5$, the steady state cracking characteristics are very strongly influenced by the bridging mechanism, which significantly enhances the delamination resistance of the structure. This is reflected both in the equilibrium force required to drive the wedge as well as in the wedge-crack tip separation distance, L. This regime is of the most practical significance, since low crack velocities will be favored for other loading configurations, such as normal impact on the laminate, to avoid the penalty of imparting high kinetic energy to the material. In crack propagation solutions where the crack tip is not constrained to travel at a given velocity, here the velocity of the wedge, it will seek an

energetically favourable velocity. Through-thickness reinforcement might thus be regarded as removing easy, low velocity fracture paths under certain dynamic conditions.

The steady state cracking configuration cannot be realized for all test and material parameters. In many cases, an upper bound to the admissible velocity exists, above which bridging ligament fracture, which is necessary for maintaining a zone of fixed length, will not occur before the wedge reaches the ligaments.

Since the load-point displacement and the equilibrium length depend fairly strongly on the velocity, the wedge angle, and the bridging parameters, the possibility arises of using measurements of the load point displacement and the equilibrium length during systematic variations of the velocity and the wedge angle to explore the dynamic constitutive behaviour of the through-thickness reinforcement. The simplicity of the wedge loaded DCB and the beam analysis makes this an attractive experimental approach.

Appendix A: **Solutions for an unbridged crack and limiting configurations**

In the absence of bridging, the deflection profile satisfying the equilibrium equation and the boundary conditions presented in equation 18 is:

$$W_u(\xi) = \frac{\alpha}{4V \, Sin(VL_u/2)} \frac{\left(\begin{array}{l} V(2\xi - \mu) \, Cos(VL_u) \; + \; V\mu \; Cos(V(L_u + \xi)) \\ + \; (2 + V^2\mu\,\xi)Sin(VL_u) \quad - \quad 2 \, Sin(V(L_u + \xi)) \end{array} \right)}{\left(Sin(VL_u/2) - \frac{\mu V}{2} Cos(VL_u/2) \right)} \quad . \quad (A.1)$$

Solution of the system of transcendental equations below (the conditions in Eqns. 19 and 20) yields L_u and $\overline{F}_u$ as dictated by equilibrium considerations and accounting for the energy flow into the crack tip region:

$$\sqrt{\overline{G}_0} = \frac{\alpha \, V(Sin(VL_u) - \frac{\mu V}{2} Cos(VL_u))}{1 - Cos(VL_u) - \frac{\mu V}{2} Sin(VL_u)} \quad , \quad (A.2a)$$

$$\overline{F}_u = \frac{2\alpha \, V^2(\alpha + \mu)}{1 - Cos(VL_u) - \frac{\mu V}{2} Sin(VL_u)} \quad . \quad (A.2b)$$

When $\mu = 0$, we obtain:

$$L_u = \frac{2}{V} \, Tan^{-1}\left(\frac{\alpha V}{\sqrt{\overline{G}_0}} \right) \quad , \quad (A.3a)$$

$$\overline{F}_u = \overline{G}_0 + V^2\alpha^2 \quad . \quad (A.3b)$$

As expected the above approach to calculating the force is identical to that obtained with the energy balance approach (Eq. 28b).

High velocity limit

In the high velocity limit $V\!\big/\!\sqrt{\overline{G}_0} \to \infty$ (which can be approximated for $V < 1$ since $\overline{G}_0$ is typically $\sim 10^{-5}$ or less), taking the appropriate branch of Tan^{-1} in Equations (A.1) and (A.2) yields:

$$L_V = \frac{1}{V}\left(\pi + Tan^{-1}\left(\frac{\mu V}{2}\right)\right) \qquad , \qquad (A.4a)$$

$$\overline{F}_V = \frac{8\alpha\,(\alpha+\mu)}{\mu^2}\left(\sqrt{1+\frac{\mu^2 V^2}{4}}\;-\;1\right) \qquad , \qquad (A.4b)$$

$$W_V = -\frac{\alpha}{2V}\;\frac{(V\xi - \sin V\xi)\sqrt{1+\dfrac{\mu^2 V^2}{4}}}{Cos^2\!\left(\dfrac{1}{2}Tan^{-1}\!\left(\dfrac{\mu V}{2}\right)\right)\left(1+\dfrac{\mu V}{2}Tan\!\left(\dfrac{1}{2}Tan^{-1}\!\left(\dfrac{\mu V}{2}\right)\right)\right)} \qquad (-L < \xi < 0)\,.$$

$$(A.4c)$$

When $\mu = 0$ and when $V\!\big/\!\sqrt{\overline{G}_0} \to \infty$, Equations (A.1) and (A.2) yield:

$$L_V = \frac{\pi}{V} \qquad , \qquad (A.5a)$$

$$\overline{F}_V = V^2\alpha^2 \qquad , \qquad (A.5b)$$

$$W_V = -\frac{\alpha}{2V}(V\xi - \sin V\xi) \qquad (-L < \xi < 0) \quad . \qquad (A.5c)$$

Quasi-static limit

When $V \to 0$, Equations (A.1) and (A.2) yield:

$$L_{V=0} = \frac{2\alpha + \mu\sqrt{\overline{G}_0} + \sqrt{4\alpha^2 + \mu^2\overline{G}_0}}{2\sqrt{\overline{G}_0}} \qquad , \qquad (A.6a)$$

$$\overline{F} = \frac{8\alpha(\alpha+\mu)}{\mu^2}\left(\sqrt{1 + \overline{G}_0\frac{\mu^2}{4\alpha^2}} - 1\right) \quad , \tag{A.6b}$$

$$W_{V=0} = \frac{1}{6\mu^2}\left(3\mu^2\sqrt{\overline{G}_0}\xi^2 - 4\alpha\xi^3 + 2\sqrt{4\alpha^2 + \mu^2\overline{G}_0}\,\xi^3\right) \qquad (-L < \xi < 0). \tag{A.6c}$$

When $\mu = 0$ and when $V \rightarrow 0$, Equations (A.1) and (A.2) yield:

$$L_{V=0} = \frac{2\alpha}{\sqrt{\overline{G}_0}} \quad , \tag{A.7a}$$

$$F_{V=0} = \overline{G}_0 \quad , \tag{A.7b}$$

$$W_{V=0} = \frac{1}{12\alpha}\left(\overline{G}_0\xi^3 + 6\alpha\sqrt{\overline{G}_0}\,\xi^2\right) \qquad (-L < \xi < 0) \quad . \tag{A.7c}$$

Small scale bridging limit

The small scale bridging limit (SSB) is obtained from the equations above by substituting $\overline{G}_T = \overline{G}_0 + \Delta\overline{G}_0$ for $\overline{G}_0$.

REFERENCES

1. K. Dransfield, C. Baillie, and Y.-W. Mai, "Improving the delamination resistance of CFRP by stitching - a review", *Comp. Science and Tech*., **50**, 305-317, (1994)

2. Cartié, D. D. R., and Partridge, I. K., "Z-Pinned Composite Laminates: Improvements in Delamination Resistance", *Proc. DFC5 Conference*, I. Mech. E., March, (1999)

3. Jain, L.K., Mai, Y.-W., "Analysis of stitched laminated ENF specimens for interlaminar mode-II fracture toughness", *Int. Journal of Fracture* **68**(3), 219-244, (1994)

4. Jain, L.K., Mai, Y-W., Determination of mode II delamination toughness of stitched laminated composites, *Composite Science and Technology*, **55**, 241-253, (1995)

5. A. P. Mouritz and B. N. Cox, " A Mechanistic Approach to the Properties of Stitched Laminates," *Composites*, **A31**, 1-27 (2000).

6. M. He and B. N. Cox, "Crack Bridging by Through-Thickness Reinforcement in Delaminating Curved Structures", *Composites A*, **29**[4] 377-93, (1998)

7. R. Massabò and B. N. Cox, "Concepts for Bridged Mode II Delamination Cracks," *J. Mech. Phys. Solids*, **47**, 1265-1300 (1999).

8. R. Massabò and B. N. Cox, "Unusual Characteristics of mixed mode delamination fracture in the presence of large scale bridging", *Mech. Comp. Mater. Structures,* **8**(1), 61-80, (2001)

9. B. N. Cox, "Delamination and Buckling in 3D Composites," *J. Comp. Mater.*, **28**, 1114-26, (1994)

10. B. N. Cox, R. Massabò, and K. T. Kedward, "Suppression of Delaminations in Curved Structures by Stitching," *Composites Part A*, **27A**, 1133-1138 (1996).

11. K.L. Rugg, Cox, B.N. and Massabò, R., Mixed mode delamination of polymer composite laminates reinforced through the thickness by z-fibers, C*omposites*, *part A*, **33/2**, 177-190 (2001).

12. B. N. Cox, R. Massabò, D. R. Mumm, A. Turrettini, and K. Kedward, "Delamination Fracture in the Presence of Through-Thickness Reinforcement," plenary paper in *Proc. of 11th Int. Conf. Composite Materials*, Gold Coast, Australia, 1997, ed. M. L. Scott (Technomic Publishing, Lancaster, Pennsylvania, 1997). pp. I-159 - I-177.

13. R. Massabò, D. Mumm, and B. N. Cox, "Characterizing Mode II Delamination Cracks in Stitched Composites," *Int. J. Fracture*, **92**, 1-38 (1998).

14. B. N. Cox and N. Sridhar, "A Traction Law for Inclined Fibre Tows Bridging Mixed Mode Cracks," *Mechanics of Composite Materials and Structures*, **9**, 299-331 (2002).

15. B. N. Cox, "Simple, Conservative Criteria for Buckling and Delamination Propagation in the Presence of Stitching," *J. Composite Materials*, **34**, 1136-47 (2000).

16. K. Rugg, B. N. Cox, K. Ward, and G. O. Sherrick, "Damage Mechanisms for Angled Through-Thickness Rod Reinforcement in Carbon-Epoxy Laminates," *Composites Part A* **29A**, 1603-1613, (1998)

17. A.P.Mouritz, and Jain, L.K., Interlaminar fracture properties of stitched fibreglass composites, In *Proc. 11th Int. Conf. Comp. Mat.*, 14-18 July 1997, ed. M. L. Scott (Technomic Publishing, Lancaster, Pennsylvania, 1997) pp. V-116 to V-127.

18. B.V. Sankar, Dharmapuri S. M., (1998), "Analysis of a stitched Double Cantilever Beam", *J Compos Mater* (24): 2203-2225 1998

19. S. Timoshenko, *Strength of materials*, Part II, MacMillan and Co., Limited, Lancaster Press, Inc., Lancaster, PA, USA, (1936).

20. E. B. Glennie, 'A strain-rate dependent crack model', *J. Mech. Phys. Solids*, **19**, 255-272 (1971)

21. E. B. Glennie, 'The unsteady motion of a rate-dependent crack model', *J. Mech. Phys. Solids*, **19**, 329-338 (1971)

22. L. B. Freund, and Lee, Y. J., 'Observations on high strain rate crack growth based on a strip yield model', *Int. Journal of Fracture*, **42**, 261-276 (1990)

23. X.-P. Xu, and Needleman, A., 'Numerical simulations of fast crack growth in brittle solids' , *J. Mech. Phys. Solids*, **42**, 1397-1434 (1994)

24. B. Yang, and Ravi-Chandar, K., 'On the role of the process zone in dynamic fracture', *J. Mech. Phys. Solids*, **44**, 1955-1976 (1996)

25. F. Costanzo, and Walton, J. R, 'A study on dynamic crack growth in elastic materials using a cohesive zone model', *Int. J. Engng. Sci.,* **35**, 1085-1114 (1997)

26. F. Costanzo, and Walton J. R., 'Steady growth of a crack with a rate and temperature sensitive cohesive zone', *J. Mech. Phys. Solids*, **50**, 1649-1679 (2002)

27. O. Samudrala, Huang Y., and Rosakis A. J., 'Subsonic and intersonic mode II crack

propagation with a rate-dependent cohesive zone', *J. Mech. Phys. Solids*, **50**, 1231-1268 (2002)

28. Y. L. Cui, 'Dynamic matrix cracking in fiber reinforced ceramics', *J. Mech. Phys. Solids*, **43**, 1875-1886 (1995)

29. L. B. Freund, A simple model of the double cantilever beam crack propagation specimen, *J. Mech. Phys. Solids*, **25**, 69-79. (1977)

30. K. Hellan, Debond dynamics of an elastic strip, I: Timoshenko-beam properties and steady motion, *International Journal of Fracture*, **14** [1], 91-100. (1978)

31. K. Hellan, Debond dynamics of an elastic strip, II: Simple transient motion, *International Journal of Fracture*, **14** [2], 91-100. (1978)

32. K. Hellan, "An alternative one-dimensional study of dynamic crack growth in DCB test specimens", *International Journal of Fracture*, **17** [3], 311-319. (1981)

33. Z.J.Bilek, and S.J.Burns, Crack propagation in wedged double cantilevered beam specimens, *J. Mech. Phys. Solids*, **22**, 85-95. (1974)

34. M.F. Kanninen, A dynamic analysis of unstable crack propagation and arrest in the DCB test specimen. *International Journal of Fracture*, **10** [3], 415-430. (1974)

35. D. D. Cartié, Ph. D. Thesis, Cranfield University, UK, 2001; D. D. Cartié, B. N. Cox, and N. A. Fleck, "Mechanisms of crack bridging by composite and metallic pins," to be submitted to *Composites.*

36. A. Turrettini, Thesis for Masters Degree, Department of Mechanical Engineering, University of California, Santa Barbara, 1996.

37. B. N. Cox, N. Sridhar, and I. J. Beyerlein, "Inertial Effects in the Pullout Mechanism During Dynamic Loading of a Bridged Crack," *Acta Mat*er., **49,** 3863-3877 (2001).

38. L.B.Freund, "Dynamic Fracture Mechanics", *Cambridge University Press*, New York (1993)

39. Z. Suo, G. Bao, and B. Fan, "Delamination R-Curve phenomena due to damage," *J. Mech. Phys. Solids*, **40** [1], 1-16. (1992)

Figure Captions

1. (a) Schematic of beam element in equilibrium. (b) Schematic of through-thickness reinforced DCB specimen loaded with a flying wedge where 2α is the wedge angle, l is the distance between the wedge and crack tip, a_0 is the length of the bridging zone, a is the total crack length, h is the thickness of the beam arm, and v is velocity of the wedge. The co-ordinate system is chosen such that $X = 0$ is the crack tip and $X = -l$ is the wedge-beam contact point.

2. Map of types of solution for the crack opening profile: T = trigonometric functions; H = hyperbolic functions; T + H = sums of trigonometric and hyperbolic functions; TH = product of hyperbolic and trigonometric functions. (a) Timoshenko beam. (b) Euler-Bernoulli beam.

3. Variation of the force applied to the wedge, F, normalized by the force applied to the wedge in the absence of bridging, F_u, as a function of the normalized velocity parameter $\alpha V / \sqrt{\overline{G_0}}$ for different values of the parameter $\Delta G_b / G_0$. Also shown is the variation with the friction coefficient parameter, $\mu^2 \overline{G_0} / 4\alpha^2$.

4. Normalized deflection profile of the DCB arm for different values of the normalized velocity. (a) Comparison of the exact solutions (solid lines) with profiles obtained by SSB approximation (dashed lines) (b) Comparison of the exact solutions (solid lines) with profiles obtained by the high velocity approximation (dashed lines). When $V = 0.001$, the length $L = 907$.

5. Variation of L, normalized by the unbridged quasi-static value, $L_u|_{v=0}$, as a function of the normalized crack velocity, V. Comparison of the exact solution (solid lines) with

solution obtained by SSB approximation (dashed line) is shown. L_v, the length in the high velocity limit, is also shown (the thick dashed line).

6. Variation of the bridging zone length, A_0, normalized by its value for a static unbridged crack, $A_0^u\big|_{v=0}$, as a function of the normalized crack velocity, V. Comparison of the exact solutions (solid lines) with the high velocity approximation (dashed line).

7. Variation of the bridging zone length, A_0, normalized by L, as a function of the (a) normalized crack velocity, V and (b) the bridging stiffness parameter B.

8. Variation of W_c^{max}, the maximum allowable value for W_c, as a function of the bridging parameter B. For all values of W_c greater than W_c^{max}, steady state crack propagation is not possible since bridging ligaments remain intact in the wedge wake ($A_0 \geq L$). Curves correspond to different values of the crack velocity, V, and the bridging parameter P_0.

9. Variation of the bridging zone length, A_0, and the maximum allowable bridging zone length, ξ_{ext}, as a function of the bridging ligament failure condition, W_c. The lower curve is the equilibrium value A_0. The upper curve corresponds to ξ_{ext} above which crack face oscillations will start to occur. The vertical line is the maximum allowable value for W_c, above which steady state crack propagation is not possible since bridging ligaments remain intact in the wedge wake ($A_0 \geq L$).

$$Q + \frac{\partial Q}{\partial x} dx$$

$$M + \frac{\partial M}{\partial x} dx$$

z

ϕ

h

x

dx

M

Q

$p(w,t)$
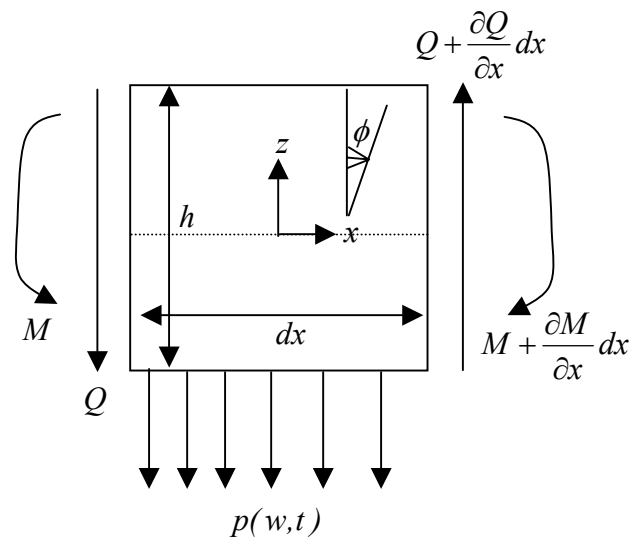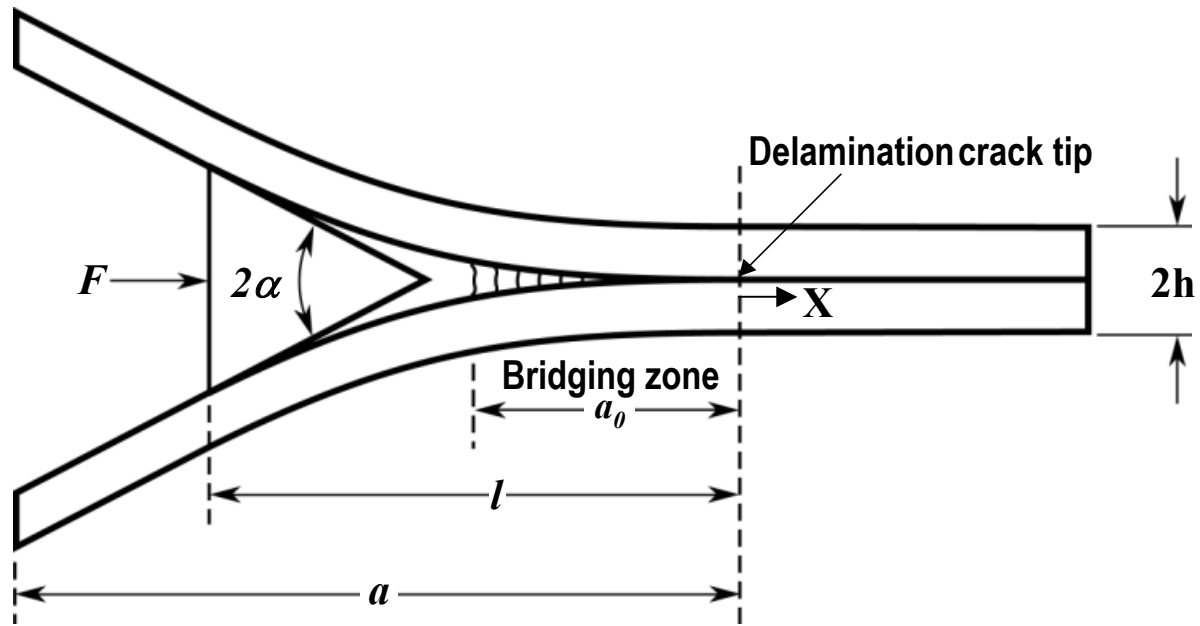
Figure 1a

Figure 1b

Figure 2a

$$S = 36\frac{v^4}{c_l^4}$$
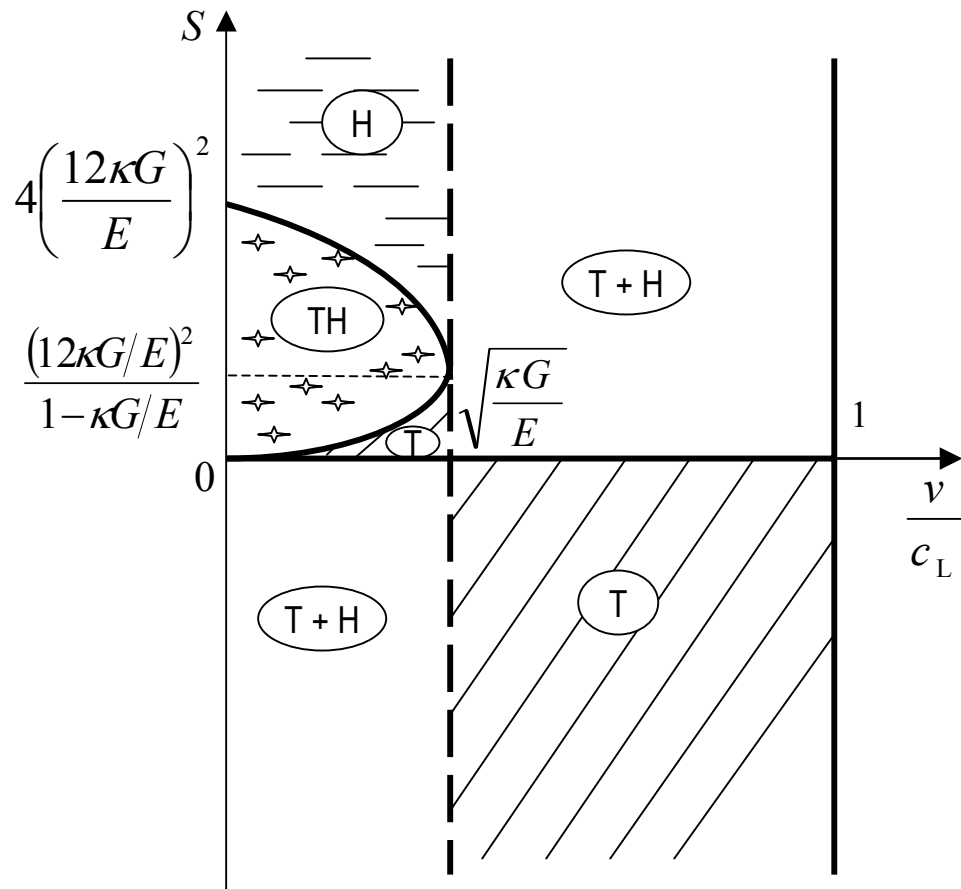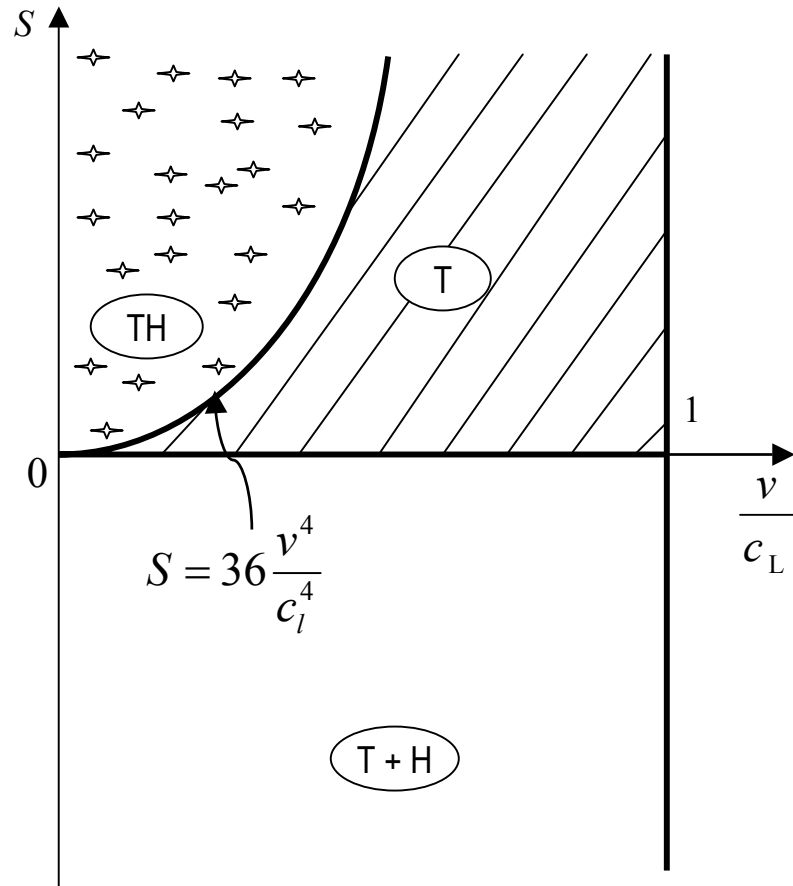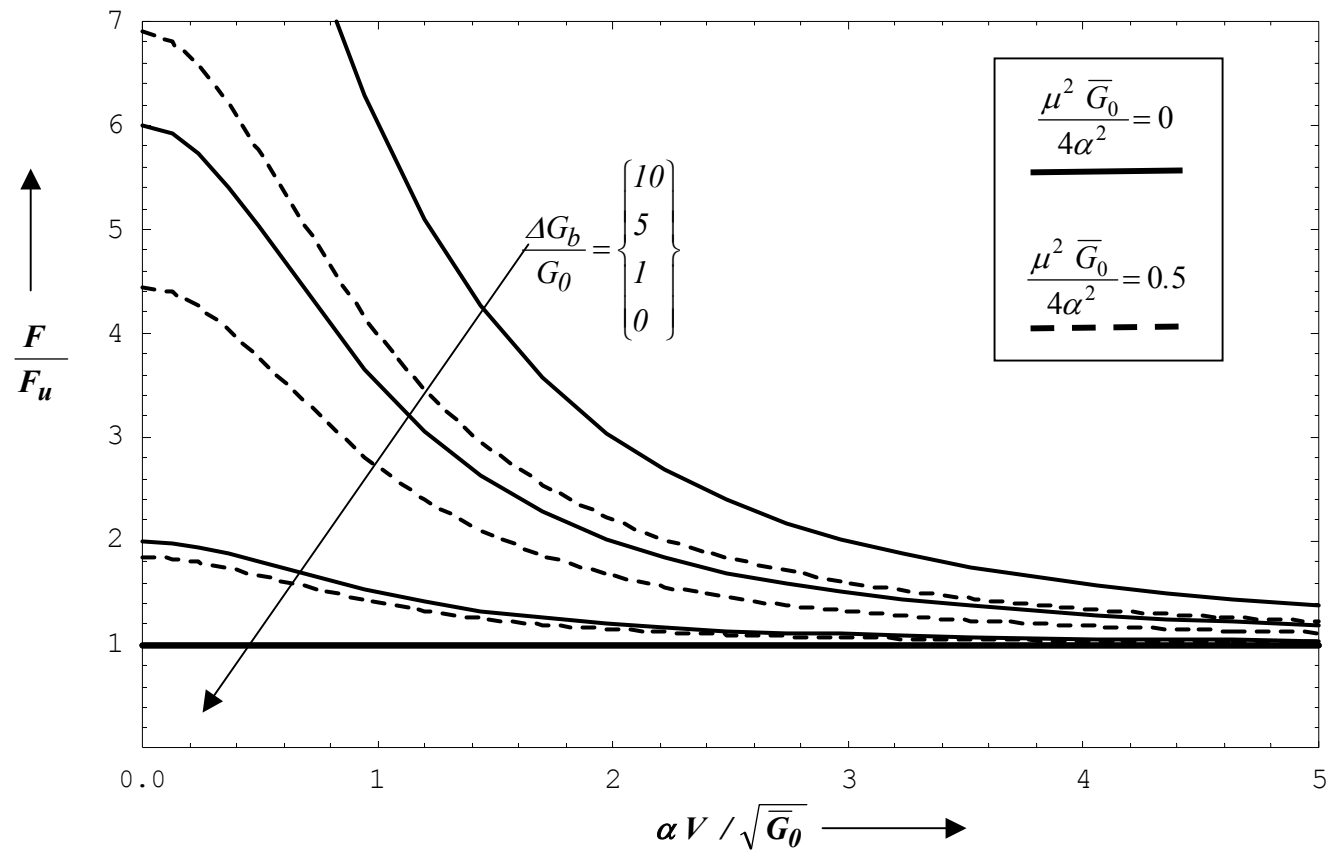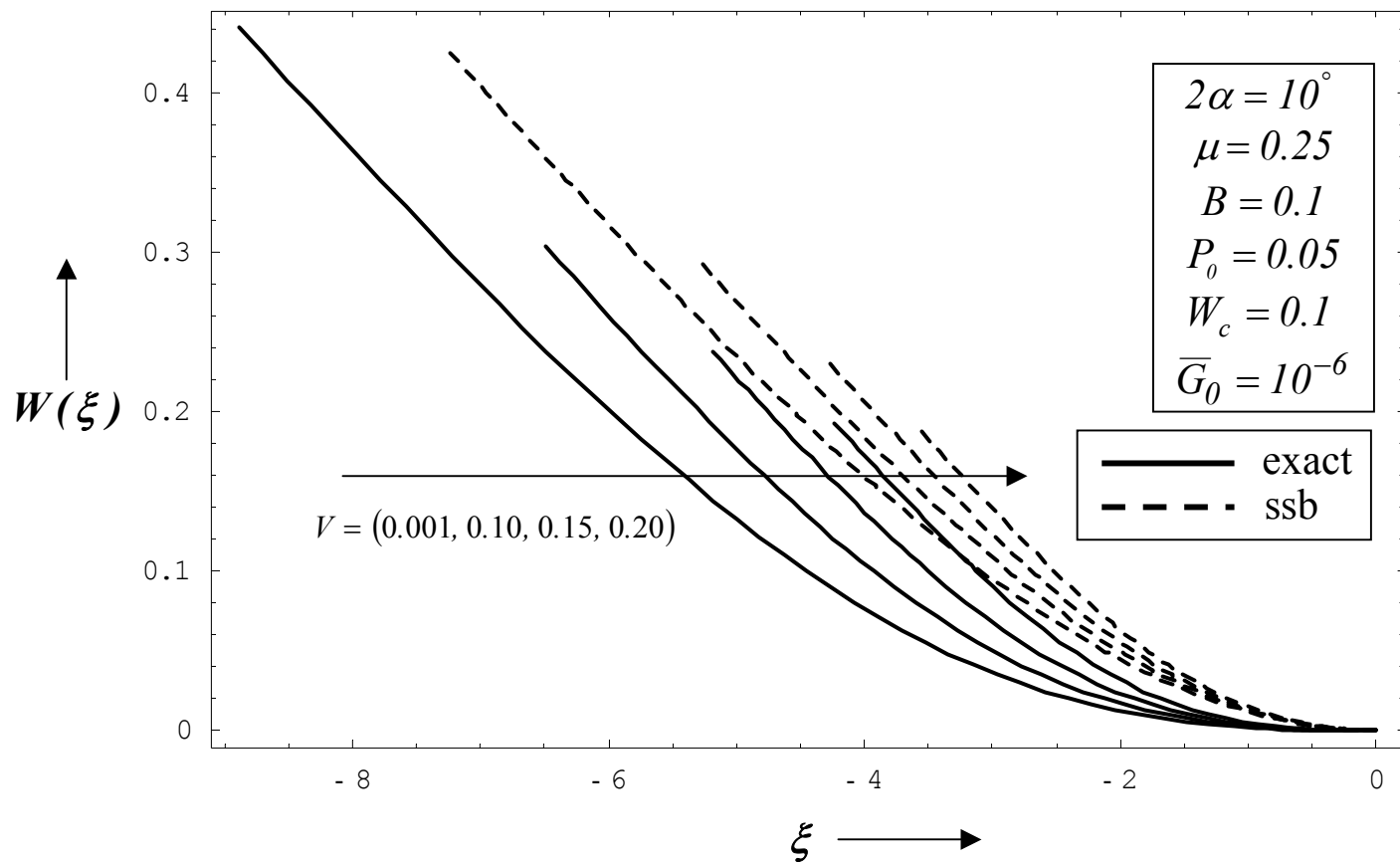
Figure 2b

Figure 3

Figure 4a

Figure 4b

Figure 5

$$\frac{A_0}{A_0^u}\bigg|_{v=0}$$

1.2

1

0.8

0.6

0.4

$B = 0.0$

0.05

0.10

0.20

0.50

$2\alpha = 10^\circ$

$\mu = 0.25$

$P_0 = 0.0$

$W_c = 0.1$

$\overline{G}_0 = 50 \: X \: 10^{-6}$

$V \longrightarrow$
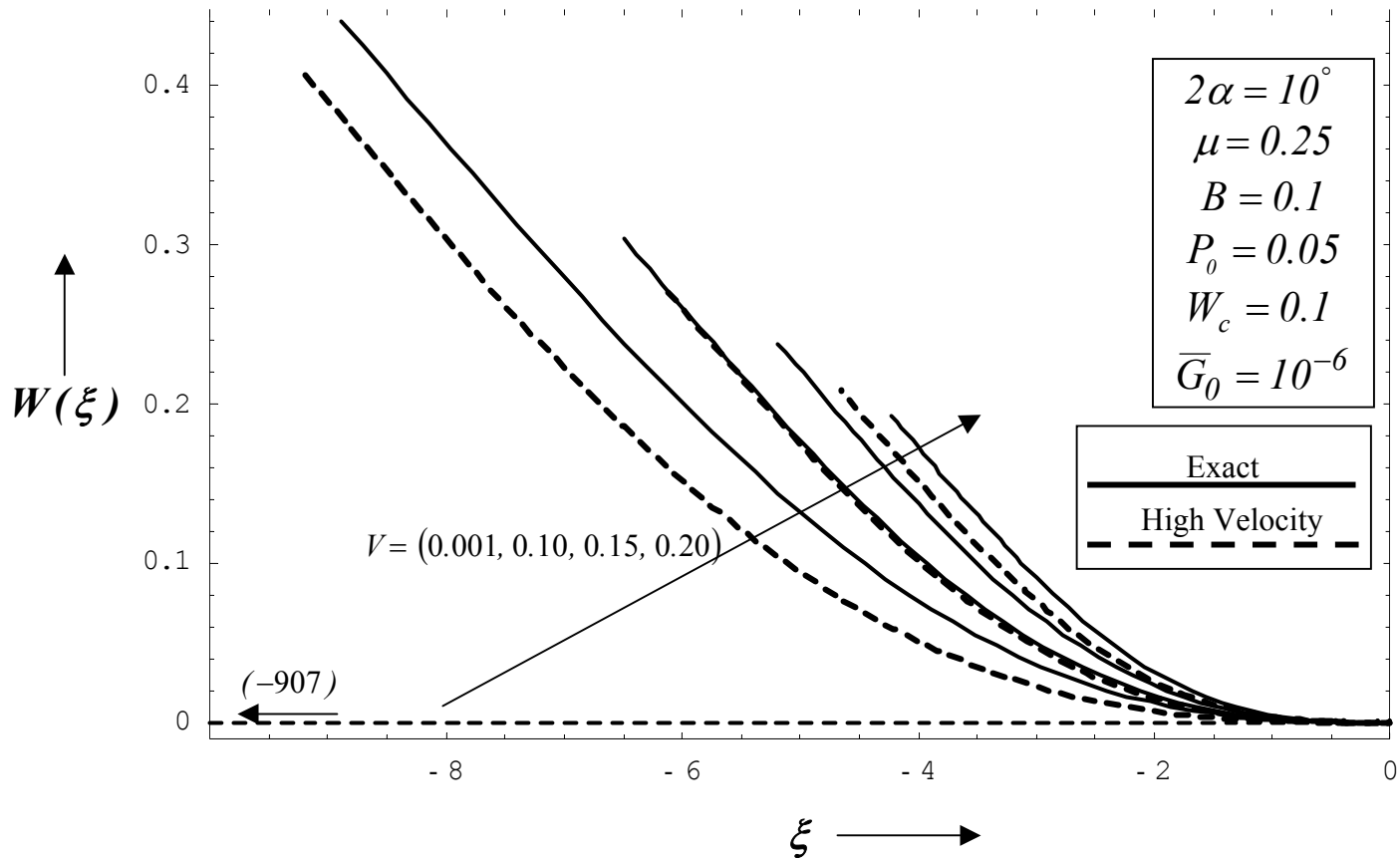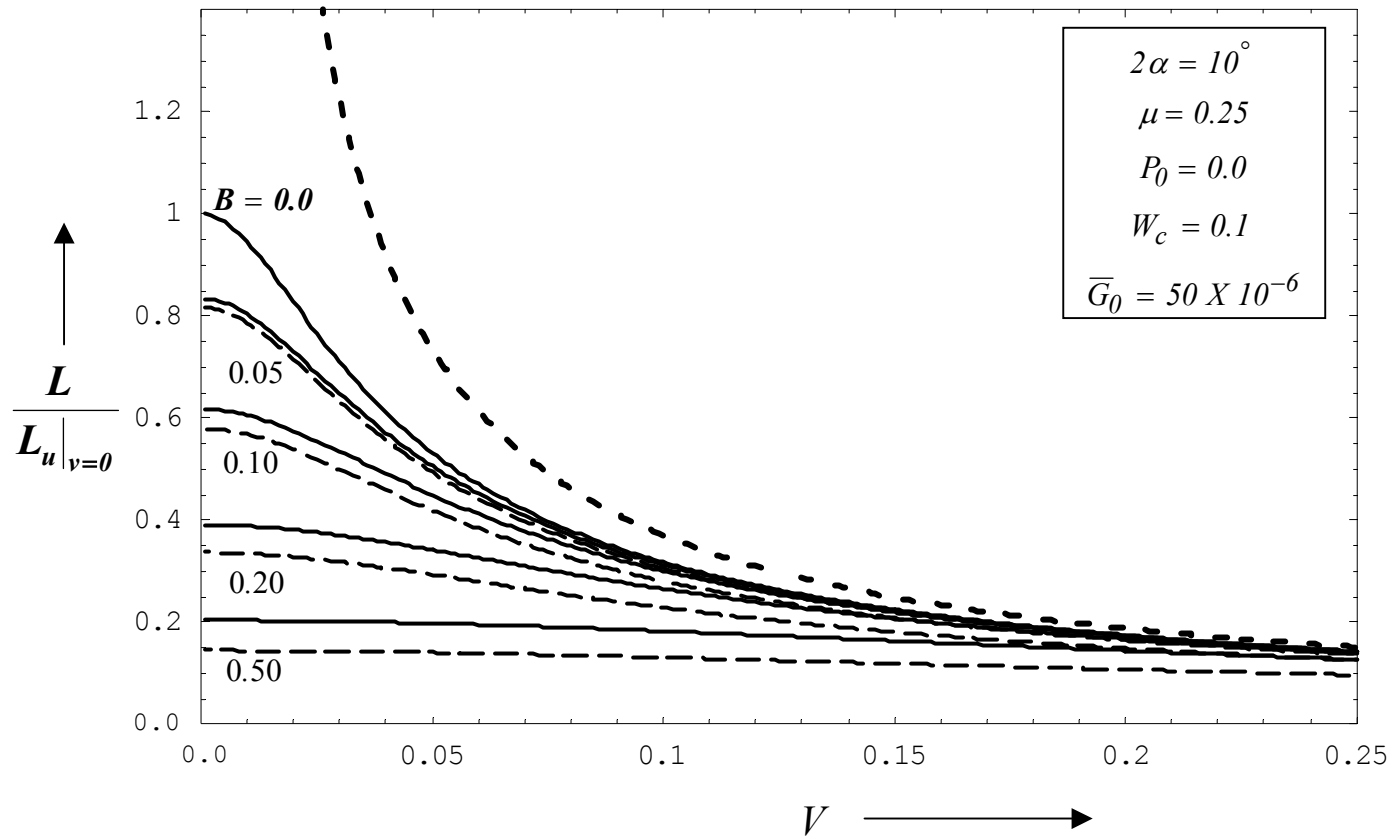
0.0   0.05   0.1   0.15   0.2   0.25
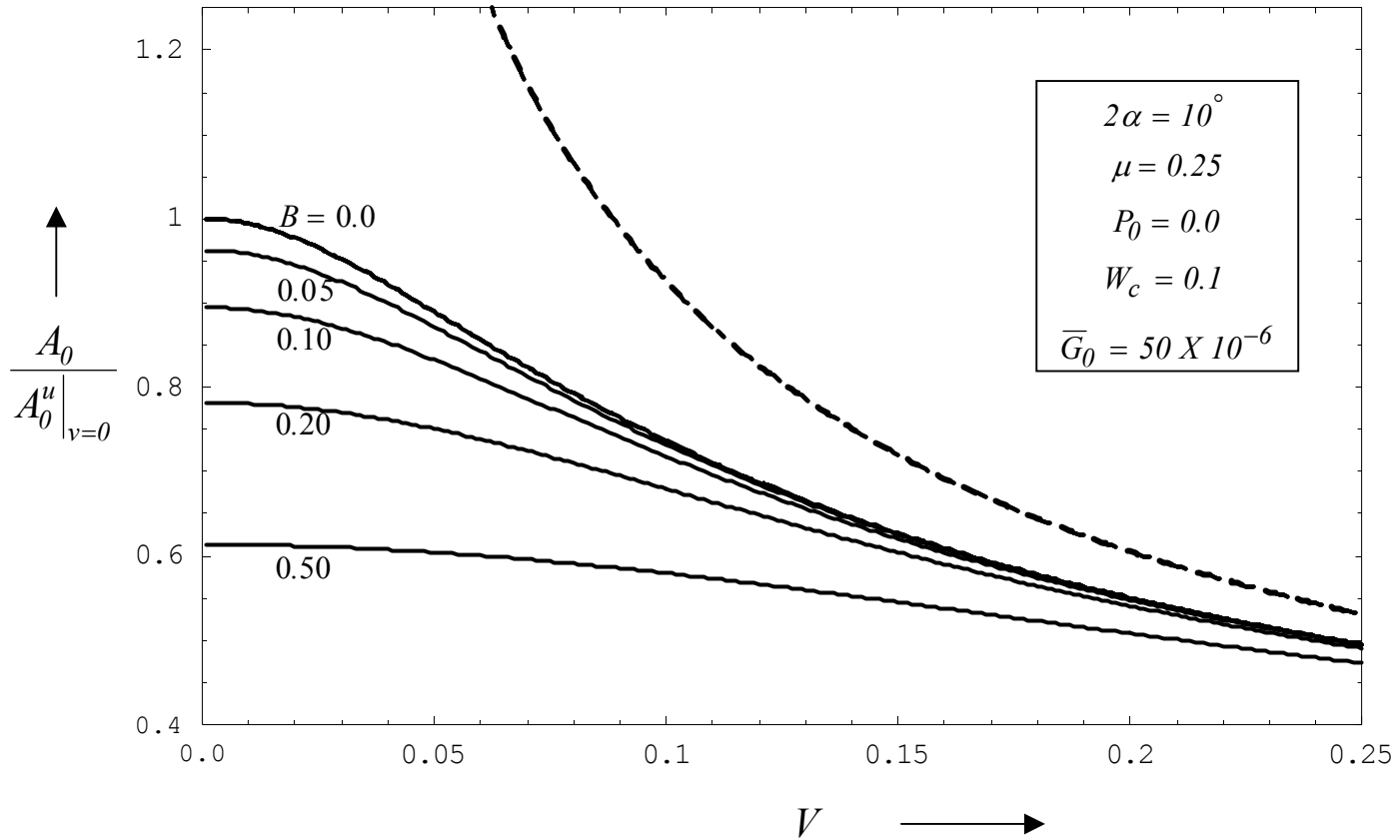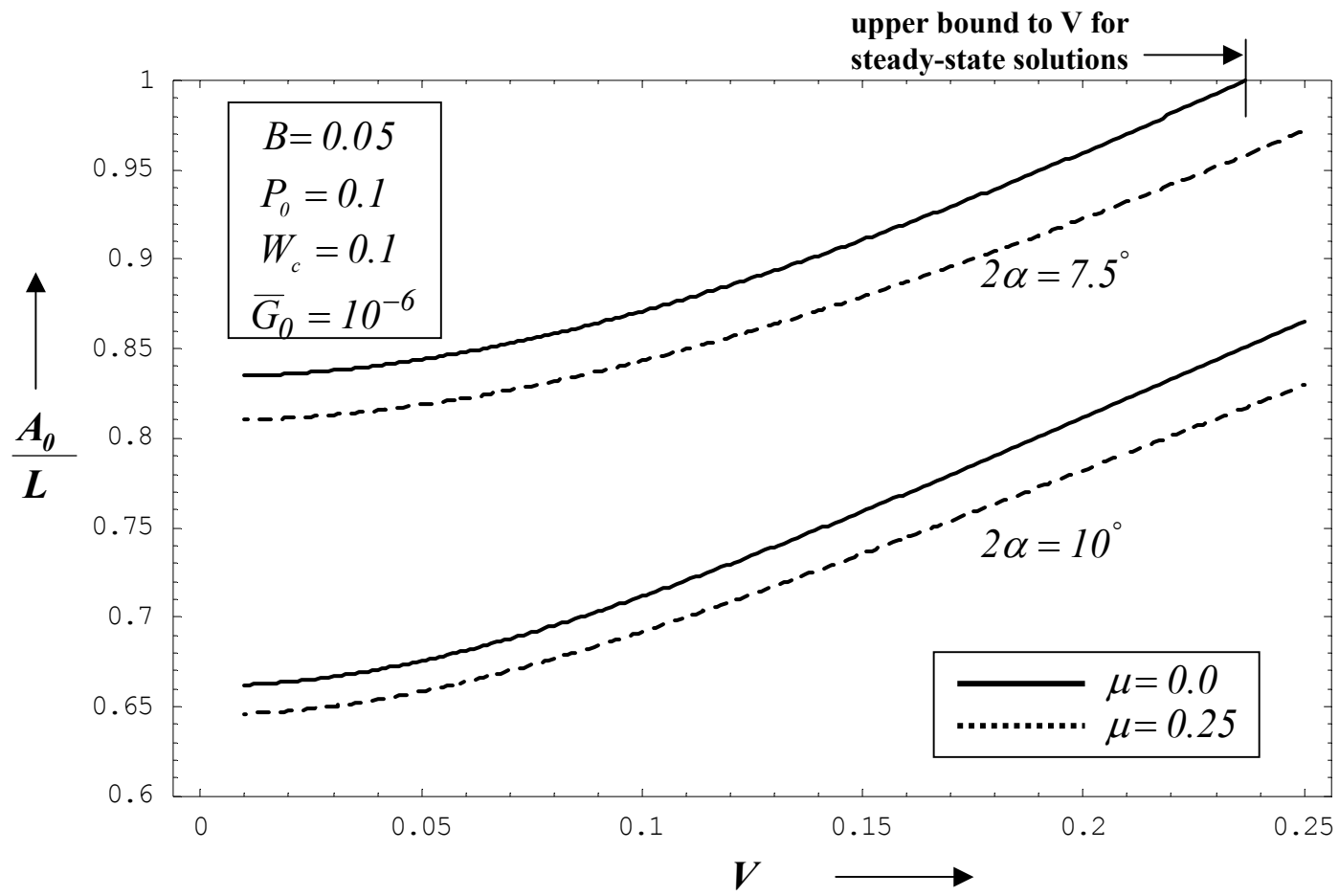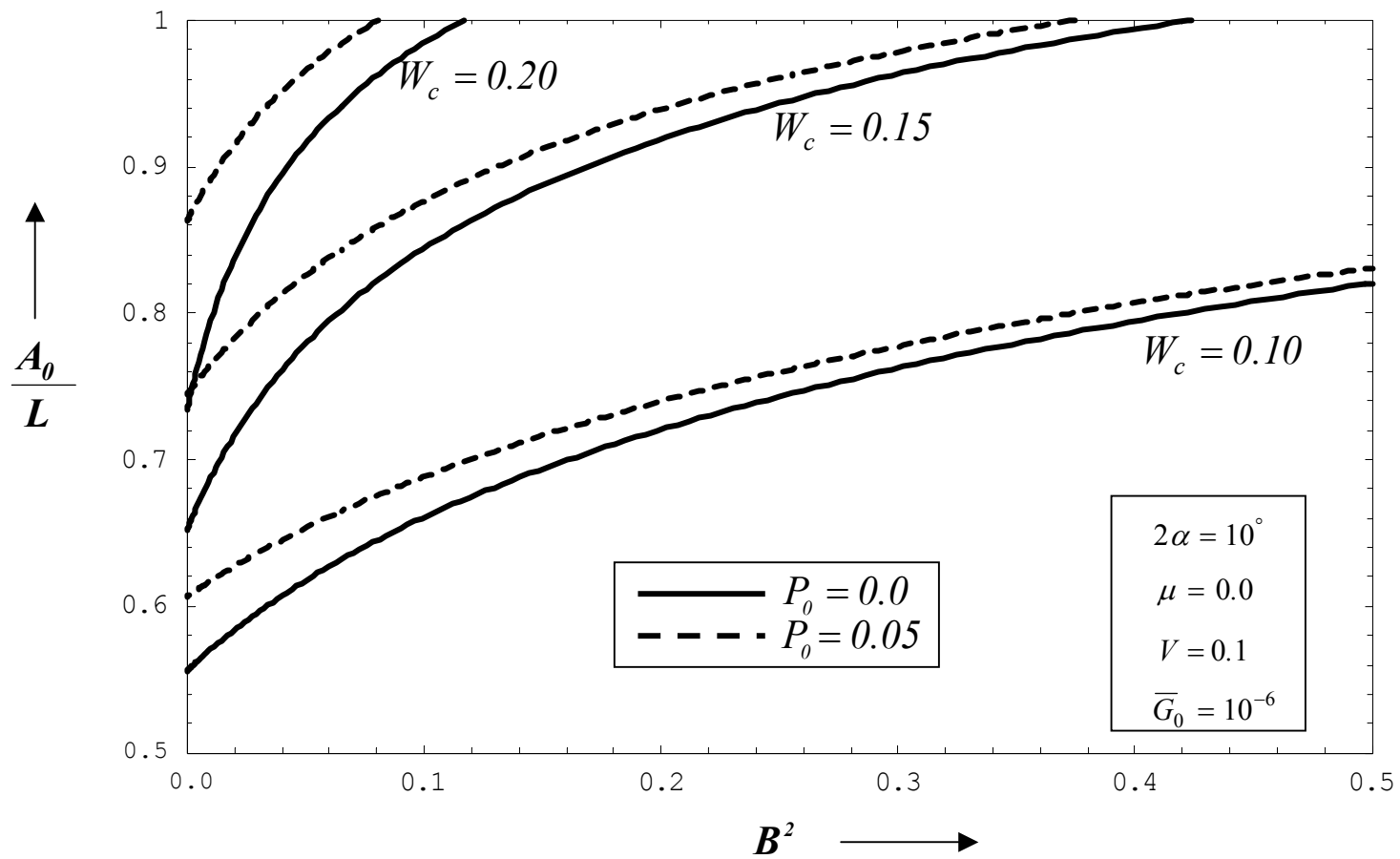
Figure 6

Figure 7a

Figure 7b
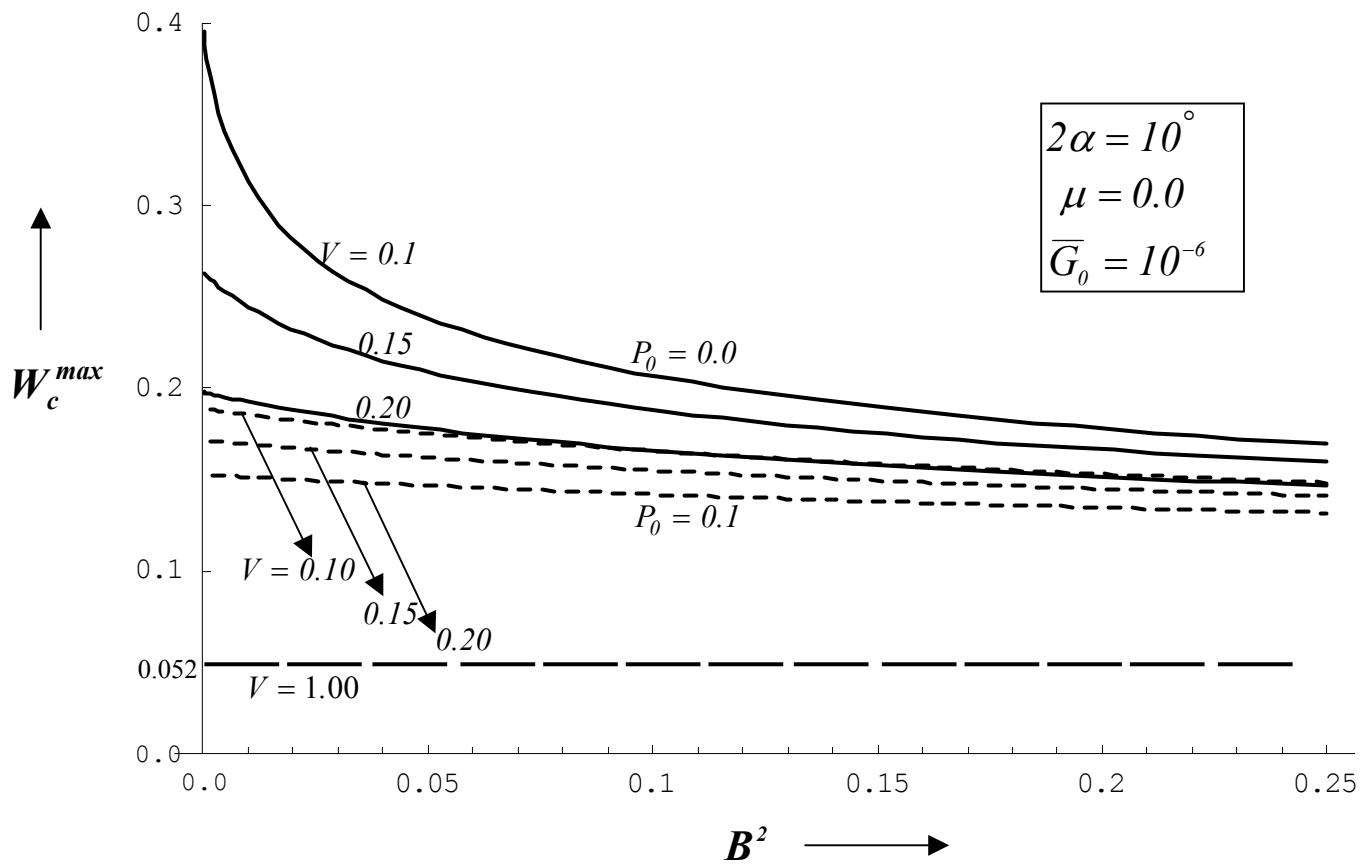
Figure 8
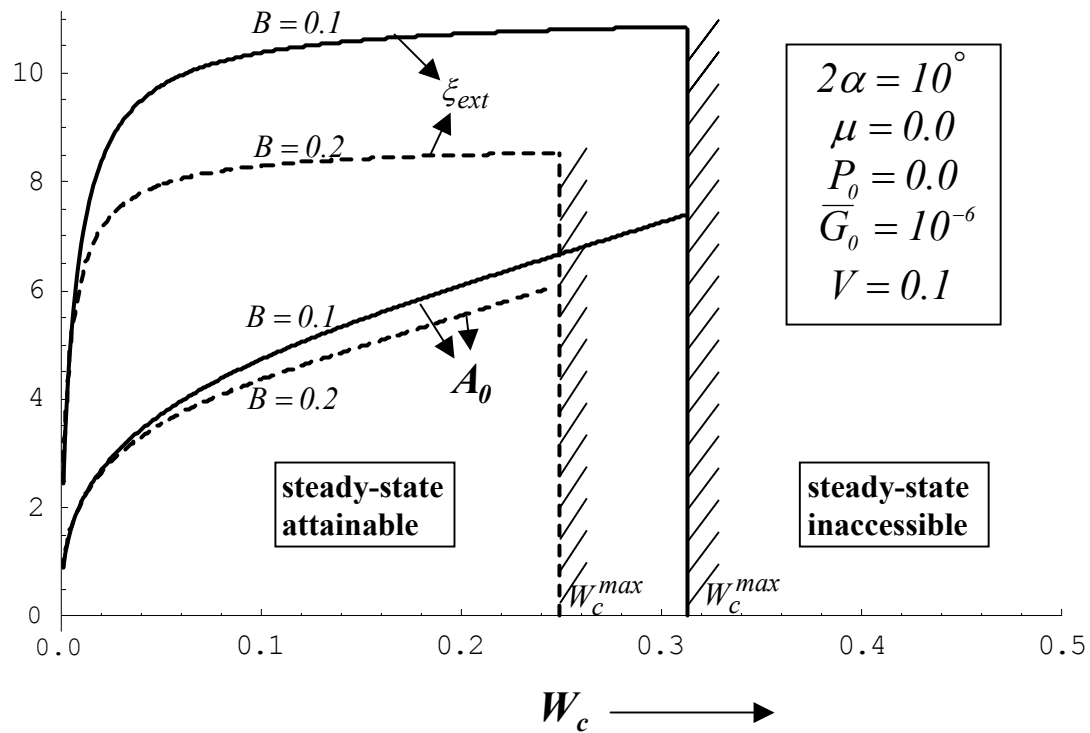
Figure 9

Slip, stick, and reverse slip characteristics during dynamic fibre pullout

N. Sridhar*, Q.D. Yang, B.N. Cox

Rockwell Scientific, 1049 Camino Dos Rios, Thousand Oaks, CA 91360, USA

Abstract

Inertial effects in the mechanism of fibre pullout (or push-in) are examined, with emphasis on how the rate of propagation of stress waves along the fibre, and thence the pullout dynamics, are governed by friction and the propagation of companion waves excited in the matrix. With a simple shear lag model (assuming zero debond energy at the fibre/matrix interface), the effect of uniform frictional coupling between the fibre and the matrix is accounted for in a straightforward way. Analytical solutions are derived when the pullout load increases linearly in time. The process zone of activated material is generally divided into two or three domains along the axis of the fibre. Within these domains, slip in the sense implied by the load, slip in the opposite sense (reverse slip), and stick may be observed. The attainable combinations define three regimes of behavior, which are realized for different material parameter values. The elastodynamic problem is also solved more accurately using a plane stress finite element method, with friction represented by an interfacial cohesive zone. The predictions of the shear lag theory are broadly confirmed. © 2003 Elsevier Science Ltd. All rights reserved.

Keywords: Dynamics; Friction; Fibre-reinforced composite material; Finite elements

1. Introduction

The mechanics of pullout have been much studied and are well understood for static loading. Simple analytical forms are available for $p(\delta)$, the relationship between the pullout load, p, and the displacement, δ, of the fibre's end, when the frictional coupling of the reinforcement to the matrix is uniform and slip extends over distances that are large compared to the reinforcement diameter (Marshall et al., 1985; McCartney, 1989; Hutchinson and Jensen, 1990). In this limit, which is a common case in ceramic

---

* Corresponding author. Tel.: +1-805-373-4774; fax: +1-805-373-4017.
  E-mail address: sridhar@rwsc.com (N. Sridhar).

composites and textile polymeric composites, the shear lag model of load transfer between the reinforcement and the matrix is accurate.

The success of shear lag models in matching numerical calculations and experiments for static pullout, given appropriate restrictions, encourages the viewpoint that similarly simple models might reveal some key aspects of pullout under dynamic loads. Prior work on the problem of a dynamically loaded rod subject to uniform friction has revealed some interesting characteristics of the effect of friction on the propagation of stress waves (Nikitin and Tyurekhodgaev, 1990). For end-loading that rises continuously from zero, the stress front propagates at velocities less than the bar wave speed by a factor that depends on the loading rate. Only for step loading does the front propagate at the bar wave speed. This strong effect of friction results in significant stiffening of the response of the bar, measured as its end displacement for a given load, relative to the static loading case. On the other hand, when motion ceases following step loading, the net fibre displacement is exactly twice that expected for static loading to the same load—in this case, dynamic effects lead to effective softening of the response (Nikitin and Tyurekhodgaev, 1990). The front configuration and front speed for this simple bar problem can be explained by considering energy conservation and kinetic constraints at the front.

When the fibres are embedded in an elastic matrix, the problem is complicated by the interaction between the stress waves in the fibre and those excited in the matrix. The front conditions must then be expected to exhibit new characteristics and consequently the load–displacement relationship for the fibre end must be affected. The role of the matrix in dynamic pullout is the topic of this paper.

In a previous study (Cox et al., 2001; Sridhar et al., 2001) a shear lag model that was directly analogous to that used successfully in static pullout problems (Hutchinson and Jensen, 1990) was extended to high loading rates with loading boundary conditions that were appropriate to the context of a bridged crack: the load was specified as a far-field condition within the body of the fibre/matrix system, rather than at the fibre end. Here new solutions are derived using a shear lag formulation with conditions appropriate to fibre pullout: the load is specified as a condition on the fibre end, with the far-field being stress-free. This configuration, as well as being interesting as a theoretical study, is representative of laboratory experiments that might be used to study frictional effects during pullout (Rosakis and Owen, 2003).

Friction is assumed here to be spatially uniform and independent of time or rate. Generally, friction in fibre pullout can be influenced by (1) Poisson's effect, which causes the fibre to shrink radially when it is pulled and thereby lowers the normal pressure at the interface; (2) initial residual compressive strains across the interface (e.g., due to mismatching thermal shrinkage during cool-down from processing); (3) interface roughness effects, which tend to increase the normal pressure at the interface when the fibre slides relative to the matrix (the interface being pushed apart by mismatching asperities); and (4) dynamic effects. The interplay of all these factors can be complex. Poisson's effect and roughness effects tend to cancel one another out; in one material system, presumably by happy accident, the cancellation appears to be fairly exact (Parthasarathy et al., 1994). In other, recent experiments where dynamic effects were anticipated, the curious result appeared that, in the system studied, the friction

remained unchanged for short times ($\sim 1\ \mu s$) after a change of state, but changed over longer times (Rosakis and Owen, 2003). Short times are relevant to the problem studied here. But in spite of these two interesting results, assuming uniform friction is a simplification. Generalization to non-uniform friction may affect the qualitative nature of some aspects of solutions to dynamic problems and will need to be addressed in due course.

The assumption of uniform friction should be distinguished from any assumption that Poisson's ratio is zero. In fact, shear lag results are derived here for general isotropic elasticity in the fibres and matrix. Assuming that friction is uniform speaks to the physics of the friction process, which may be influenced by other phenomena, as outlined above.

Provided friction is approximately uniform in a given system, the shear lag results derived here are equally applicable to fibre push-in, with appropriate changes of sign. Fibre pullout and push-in experiments are widely used in static loading problems to characterize friction and composite behaviour. A prime attraction of the methods is the simplicity of both the phenomena involved and their (accurate) analysis by shear lag approximations. Therefore, strong motivation exists for seeking extensions of these experiments in the dynamic regime.

Some interesting new characteristics of stress wave propagation are discovered for the particular case of a load that increases linearly in time. The regime of validity of the shear lag approximation is then assessed by finite element calculations of a fibre/matrix system in which friction is represented as a cohesive zone.

2. Shear lag approximation

The shear lag approximation in the axisymmetric problem of the pullout of a cylindrical fibre may be stated as the assumption that the displacements and stresses in any section normal to the z-axis (the axis of the fibre) are characterized by Lamé-like solutions, generalized to allow variations with z (Hutchinson and Jensen, 1990). Thus all displacements are separable functions of z and the radial variable, r; and the dependence on r has a known, simple form. For static loading, shear lag is an accurate approximation as long as the slip distance, l_s, is large compared to the fibre diameter, d. This is equivalent to requiring that the axial stress in the fibre and the matrix should vary slowly over distances comparable to the fibre radius (Nairn, 1997). The shear lag approximation is quite accurate in the static case over a wide range of fibre/matrix modulus ratios, and fibre volume fractions (Freund, 1992; Nairn, 1997). In the analysis that follows, the shear lag approximation is shown to work well for the dynamic problem as well. The analytical solutions obtained with the shear lag assumption are attractively simple and insightful and provide limits against which three-dimensional (3D) numerical solutions can be compared.

For the static pullout problem, Lamé-like solutions have also been developed with a non-zero debond energy included (energy required for separation of the fibres and the matrix) (Freund, 1992). Here, the debond energy is assumed to be zero (fibres and matrix already chemically separated). In many materials, the work done against friction

dominates and solutions in which the debond energy is included must then approach those obtained here asymptotically. Models of the static behaviour of composites with weak interfaces, especially ceramic composites, often ignore the debond energy successfully. Dynamic analysis of materials in which the debond energy is not small could be significantly more complicated.

3. Micromechanics of dynamic pullout

When friction is the only active force of resistance, the dynamic pullout problem is one of wave propagation along a fibre in the presence of frictional retardation. For simplicity of language, the presentation of shear lag results will be confined to an axisymmetric problem. However, the plane problem of a plate-like fibre and matrix has identical form in the shear lag approximation, with an appropriate redefinition of the radius variable in terms of a thickness variable (Appendix A).

The pullout problem can be idealized as follows. A representative volume (Fig. 1) consists of a cylindrical fibre of radius R_f embedded in a matrix ($z \geqslant 0$). The matrix is represented by a cylindrical shell whose thickness corresponds to a fibre volume fraction, f, with appropriate boundary conditions on its outer surface. Both media are assumed to be isotropic, with Young's moduli E_f and E_m, Poisson's ratios μ_f and μ_m, and densities ρ_f and ρ_m (subscript m denoting matrix and f fibre). The axial displacement, strain, and stress of the fibre and the matrix are denoted u_f and u_m, ε_f and ε_m, and σ_f and σ_m, respectively. Following the strategy of shear lag for axisymmetric problems, the wave problem can be reduced to equations in the spatial variable, z, only; variations in any section transverse to the z-axis are solutions of the Lamé problem.

The fibre is coupled to the matrix by the friction stress τ_f where

$$\tau_f = \begin{cases} \tau_0 & \text{(when } \dot{u}_f - \dot{u}_m < 0\text{)}, \\ \tilde{\tau} & \text{(when } \dot{u}_f - \dot{u}_m = 0\text{)}, \\ -\tau_0 & \text{(when } \dot{u}_f - \dot{u}_m > 0\text{)}. \end{cases} \tag{1a}$$

The friction stress is assumed to be uniform and constant where relative motion exists and indeterminate, with the bound $|\tilde{\tau}| < \tau_0$, where there is no relative motion. With such a friction law, the dynamic wave equations for the fibre and the matrix subject to the shear-lag approximation are (see Appendix A):

$$\frac{\partial^2 u_f}{\partial z^2} = -\frac{2\tau_f}{R_f \hat{E}_f} + \frac{1}{c_f^2} \frac{\partial^2 u_f}{\partial t^2} \quad \text{(fibre)}, \tag{2a}$$

$$\frac{\partial^2 u_m}{\partial z^2} = \frac{2f}{1-f} \frac{\tau_f}{R_f \hat{E}_m} + \frac{1}{c_m^2} \frac{\partial^2 u_m}{\partial t^2} \quad \text{(matrix)}, \tag{2b}$$

where $c_i = \sqrt{\hat{E}_i / \rho_i}$, $\hat{E}_i = E_i(1 - \mu_i)/((1 + \mu_i)(1 - 2\mu_i))$, $i = $ m or f. The traction boundary conditions at $z = 0$ are that the matrix is stress-free, while the fibres sustain the axial
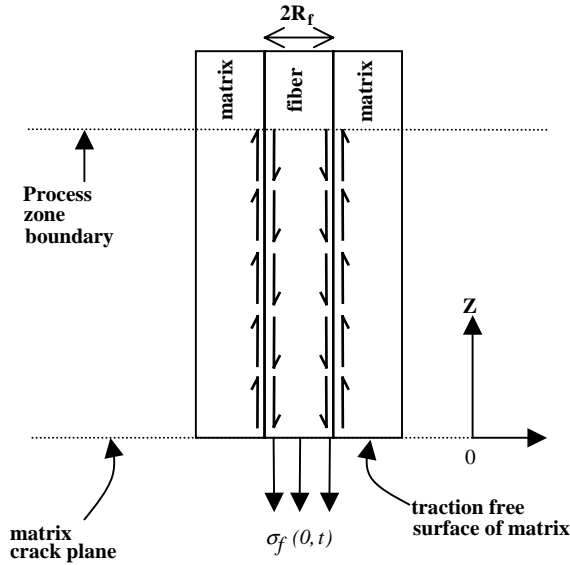
Fig. 1. Schematic of the dynamic pullout problem in a composite near the fracture plane.

traction $\sigma_f(0, t) = p(t)$. In a crack problem, shear tractions may arise along the vertical boundaries of the representative volume (parallel to z), but these are neglected.

The following normalizations are introduced: $Z = z/R_f$, $T = c_f t/R_f$, and $U = u/R_f$. Combining Eqs. (1) and (2) yields

$$\frac{\partial^2 U_f}{\partial Z^2} = \frac{\partial^2 U_f}{\partial T^2} - \tau \, \text{Sign}(\dot{U}_m - \dot{U}_f), \tag{3a}$$

$$\frac{\partial^2 U_m}{\partial Z^2} = C^2 \frac{\partial^2 U_m}{\partial T^2} + \varphi\tau \, \text{Sign}(\dot{U}_m - \dot{U}_f), \tag{3b}$$

where the dimensionless parameters include the wave speed ratio C, the modulus ratio φ, and the normalized interfacial friction stress τ:

$$C^2 = \frac{c_f^2}{c_m^2} = \frac{\hat{E}_f/\rho_f}{\hat{E}_m/\rho_m}, \tag{4a}$$

$$\varphi = \frac{f E_f}{(1 - f)E_m}, \tag{4b}$$

$$\tau = \frac{2\tau_0}{E_f}. \tag{4c}$$

4. Boundary fibre stress rising linearly in time

Finding solutions to Eqs. (3) and (4) for general loading histories is complicated by the non-linearity inherent in the friction term. However, analytical results can be

obtained for special cases, including that of a load rising linearly in time. Since a linear loading history has some practical importance, solutions for this case will be described here to explore various interesting characteristics of the dynamic pullout phenomenon and for assessing the validity of the shear lag approximation. The solutions were found by observing that the boundary conditions admitted only quadratic functions of position and time; and seeking self-consistent patterns of motion (slip, stick, and reverse slip) by heuristic arguments.

Let the linear loading function be

$$p(t) = \sigma_0 t / t_0, \tag{5a}$$

where σ_0 / t_0 is constant. The following further normalized parameter is employed:

$$k = \frac{\tau_0 c_f t_0}{\sigma_0 R_f}, \tag{5b}$$

where k is the inverse loading rate.

Solutions to the linear loading problem are characterized by the existence of either two or three domains of z, depending on the magnitudes of C and φ. Displacements are continuous and smooth within each domain; but, since the friction stress can be discontinuous at a domain boundary, the displacements need only be continuous, not smooth, at domain boundaries.

The domains will be denoted $[0, l_1]$, $[l_1, l_2]$, and, if a third domain exists, $[l_2, l_3]$. The domain boundaries move linearly in time, i.e., $l_i = \eta_i c_f t$ ($i = 1, 2$ or 3), where the constants η_i depend on the material and geometrical parameters. Thus the furthest propagation of the stress disturbance lies at the front $z = l_{total}$ (where $l_{total} = l_2$ or l_3 depending on the value of C and φ) where, for end loading of the fibre, the additional boundary condition holds, that $\dot{u}_f = \dot{u}_m = 0$. The domain $[0, l_{total}]$, i.e., the entire of domain of activated material, will be referred to as the process zone, rather than the slip zone, since in some cases part of it will not be actively slipping.

The displacements are always piecewise quadratic functions of axial position, z. The stresses are therefore linear in z. In exhibiting the solutions in the following, only the displacements will be described in detail, for brevity.

Three different regimes of physically distinct behavior can be identified for different values of the dimensionless wave speed ratio C, as follows.

4.1. Regime I: pure slip ($C > C_U$)

In this regime, two domains are present ($l_{total} = l_2$). The regime is defined by the wave speed ratio, C, exceeding an upper critical value, C_U, which is specified in Section 4.4. The displacement solutions to the wave equation subject to the initial and boundary conditions are

$$U_f(Z, T) = \frac{\tau(-Z + T\eta_2)(Z(k + \eta_2) - T(1 - k\eta_2))}{2k(1 + \eta_2^2)} \quad (0 \leqslant Z \leqslant \eta_2 T), \tag{6a}$$
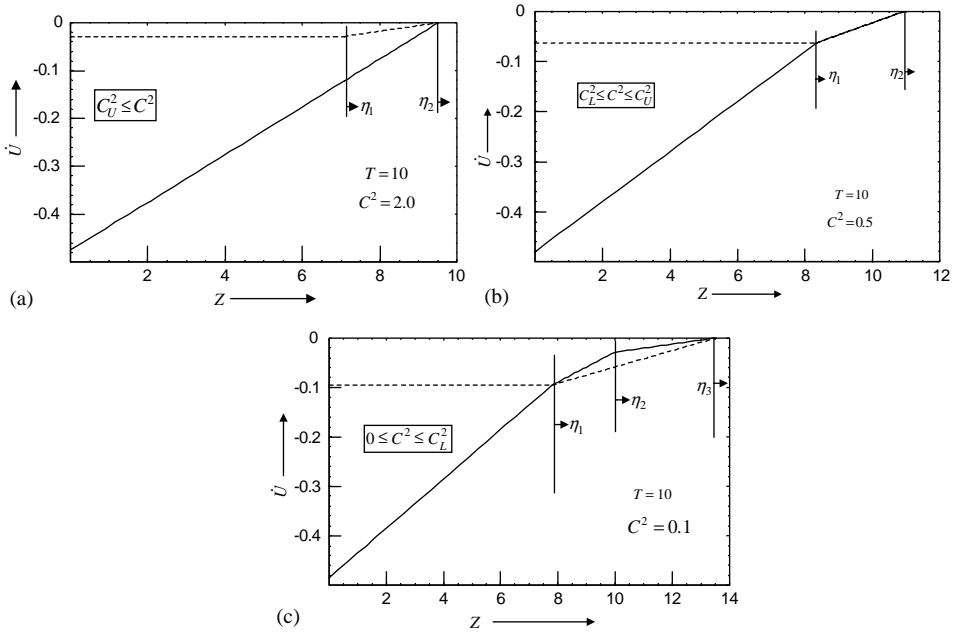
Fig. 2. Spatial variation of the particle velocity when (a) $C_U \leqslant C$ (b) $C_L \leqslant C \leqslant C_U$ and (c) $0 \leqslant C \leqslant C_L$. This variation is shown for both the fibre (solid lines) and the matrix (dashed lines) for $\varphi = 2.00$, $k = 0.05$, $\tau = 0.005$ and when $T = 0.1$.

$$
U_{\mathrm{m}}(Z,T) = \begin{cases} \dfrac{\tau\varphi \left(\begin{array}{c} Z^2(1 + \eta_1^2 C^2 - 2\eta_1\eta_2 C^2) \\ + T^2(\eta_2^2 - 2\eta_1\eta_2 + \eta_1^2\eta_2^2 C^2) \end{array} \right)}{2(1 + \eta_1^2 C^2)(1 - \eta_2^2 C^2)} & (0 \leqslant Z \leqslant \eta_1 T), \\[4mm] \dfrac{\tau\varphi}{2(1 - \eta_2^2 C^2)}(Z - \eta_2 T)^2 & (\eta_1 T < Z \leqslant \eta_2 T). \end{cases} \tag{6b}
$$

The front speeds η_1 and η_2 are given by

$$
\eta_1 = \frac{1}{C}, \tag{7a}
$$

$$
\eta_2 = \sqrt{1 + k^2} - k \tag{7b}
$$

and are independent of time.

   The particle velocity variation is shown in Fig. 2a as a function of position for two different times. As time increases, the process zone grows and the particle velocity at a given material point increases in both the fibre and the matrix. The matrix particle velocity is greater than the fibre particle velocity ($\dot{u}_{\mathrm{m}} > \dot{u}_{\mathrm{f}}$) over the entire process zone; and hence both domains, $[0, l_1]$ and $[l_1, l_2]$ are slip zones with $\tau_{\mathrm{f}} = \tau_0$. At fixed time, the particle velocity decreases linearly with position z, whereas the particle velocity in the matrix is spatially uniform in the domain, $[0, l_1]$, but then decreases

linearly to zero in the domain, $[l_1, l_2]$. The normalized front speed η_1 depends only on C and the normalized front speed η_2 depends only on k (Eq. (7)). Both η_1 and η_2 are independent of φ and thus of the fibre volume fraction.

4.2. Regime II: slip-stick ($C_L \leqslant C \leqslant C_U$)

The second limiting value, C_L, is also specified in Section 4.4. When the wave speed ratio is bounded by $C_L \leqslant C \leqslant C_U$, there are again two domains ($l_{\text{total}} = l_2$) and the displacement solutions to the wave equation subject to the prescribed initial and boundary conditions are

$$
U_{\text{f}}(Z,T) = \begin{cases} \tau \dfrac{\left(\begin{array}{c} -Z^2(2k + \eta_1 + \eta_2) + 2ZT(1 + \eta_1\eta_2) \\ +T^2(2k\eta_1\eta_2 - \eta_1 - \eta_2) \end{array} \right)}{4k(1 + \eta_1\eta_2)} & (0 \leqslant Z \leqslant \eta_1 T), \\[20pt] \dfrac{\tau(\eta_1^2 + 2k\eta_1 - 1)(Z - \eta_2 T)^2}{4k(1 + \eta_1\eta_2)(\eta_2 - \eta_1)} & (\eta_1 T < Z \leqslant \eta_2 T), \end{cases}
$$

$$\text{(8a)}$$

$$
U_{\text{m}}(Z,T)
$$
$$
= \begin{cases} \tau \dfrac{\left(\begin{array}{c} Z^2((\eta_1^2 + 2k\eta_1 - 1)(\eta_2 - \eta_1)C^2 + 2k\varphi(1 + \eta_1\eta_2)) \\ +T^2((\eta_1^2 + 2k\eta_1 - 1)(\eta_2 - \eta_1) - 2k\varphi\eta_1^2(1 + \eta_1\eta_2)) \end{array} \right)}{4k(1 + \eta_1\eta_2)(1 + \eta_1^2 C^2)} & (0 \leqslant Z \leqslant \eta_1 T), \\[20pt] \dfrac{\tau(\eta_1^2 + 2k\eta_1 - 1)(Z - \eta_2 T)^2}{4k(1 + \eta_1\eta_2)(\eta_2 - \eta_1)} & (\eta_1 T < Z \leqslant \eta_2 T). \end{cases}
$$

$$\text{(8b)}$$

The process zone front speed η_2 is

$$
\eta_2 = \sqrt{\frac{1 + \varphi}{C^2 + \varphi}} \tag{9a}
$$

while η_1 is obtained by solving the cubic equation:

$$
(\eta_1^2 + 2k\eta_1 - 1)(1 + C^2\eta_1\eta_2) + 2k\varphi(1 + \eta_1\eta_2)\eta_1 = 0. \tag{9b}
$$

Analysis shows that η_1 has only one real positive root which always lies in $(0,1)$. The spatial particle velocity variation is shown in Fig. 2b. The matrix particle velocity in the domain $[0, l_1]$ is greater than the fibre particle velocity ($\dot{u}_{\text{m}} > \dot{u}_{\text{f}}$) for any z, and hence slip is occurring. However in $[l_1, l_2]$, the particle velocity is the same in the fibre and the matrix and hence in this domain the fibre and matrix stick. The interfacial

friction stress in this stick zone is

$$\tau_f = \tilde{\tau} = \tau_0 \frac{(\eta_1^2 + 2k\eta_1 - 1)(1 - C^2)}{2k(\eta_1(1 - C^2) + (1 - \eta_1^2)\sqrt{(C^2 + \varphi)(1 + \varphi)})} \tag{10}$$

where η_1 has been obtained by solving Eq. (9b). This expression for the friction stress always satisfies $|\tau_f| < |\tau_0|$.

4.3. Regime III: slip-reverse slip $C \leqslant C_L$

In this case, the wave speed ratio, C, obeys the bound $C \leqslant C_L$ and three domains exist ($l_{total} = l_3$). The displacement solutions to the wave equation subject to the initial and boundary conditions are

$$U_f(Z, T) = \begin{cases} \tau\dfrac{\left(\begin{array}{c} Z^2(2k(\eta_1 - 2\eta_3 - 1) - (1 + \eta_1)(1 + \eta_3)) \\ -T^2(1 + \eta_3 + 2k\eta_3 + \eta_1(1 + \eta_3 - 2k(\eta_3 + 2))) \\ +2ZT(1 + \eta_1)(1 + \eta_3) \end{array}\right)}{4k(1 + \eta_1)(1 + \eta_3)} & (0 \leqslant Z \leqslant \eta_1 T), \\[2em] \tau\dfrac{\left(\begin{array}{c} Z^2(1 + \eta_3 - \eta_1^2(1 + \eta_3) + 2k(\eta_1^2 - 1 - 2\eta_1(1 + \eta_3))) \\ +T^2((\eta_1^2 - 1)(1 + \eta_3) + 4k\eta_1 + 2k\eta_3(\eta_1^2 + 2\eta_1 - 1)) \\ +2ZT(\eta_1^2 + 4k\eta_1 - 1)(1 + \eta_3) \end{array}\right)}{4k(\eta_1^2 - 1)(1 + \eta_3)} & (\eta_1 T < Z \leqslant \eta_2 T), \\[2em] \dfrac{\tau(Z - \eta_3 T)^2}{2k(1 - \eta_3^2)} & (\eta_2 T < Z \leqslant \eta_3 T) \end{cases} \tag{11a}$$

$$U_m(Z, T) = \begin{cases} \tau\varphi\dfrac{\left(\begin{array}{c} Z^2(1 + \eta_1^2 C^2 - 4\eta_1\eta_3 C^2 + 2\eta_3^2 C^2) \\ +T^2(\eta_3^2 - 4\eta_1\eta_3 + 2\eta_1^2\eta_3^2 C^2 + 2\eta_1^2) \end{array}\right)}{2(1 - \eta_1^2 C^2)(1 + \eta_3^2 C^2)} & (0 \leqslant Z \leqslant \eta_1 T), \\[2em] \dfrac{\tau\varphi(Z - \eta_3 T)\left(\begin{array}{c} Z(1 - \eta_1^2 C^2 + 4\eta_1\eta_3 C^2) \\ +T(\eta_3 - \eta_1^2\eta_3 C^2 - 4\eta_1) \end{array}\right)}{2(\eta_1^2 C^2 - 1)(\eta_3^2 C^2 + 1)} & (\eta_1 T < Z \leqslant \eta_3 T). \end{cases} \tag{11b}$$

The front speed η_2 is

$$\eta_2 = 1 \tag{12a}$$

while η_1 and η_3 are obtained by solving the cubic equations:

$$\eta_3 - \eta_1^2 \eta_3 C^2 + 2\eta_1(\eta_3^2 C^2 - 1) = 0, \tag{12b}$$

$$\frac{(\eta_1 - 1)}{(\eta_1 + 1)} + \frac{1}{(\eta_3 + 1)} - \frac{\varphi(\eta_3^2 - 4\eta_1\eta_3 + \eta_1^2\eta_3^2 C^2 + 2\eta_1^2)}{(1 - \eta_1^2 C^2)(1 + \eta_3^2 C^2)} = \frac{(1 - \eta_1)}{2k}. \tag{12c}$$

The particle velocity varies with z as shown in Fig. 2c. The matrix particle velocity over $0 \leqslant Z \leqslant \eta_1 T$ is greater than the fibre particle velocity ($\dot{u}_m > \dot{u}_f$) whereas in the region $\eta_1 T \leqslant Z \leqslant \eta_3 T$ the fibre particle velocity is greater than the matrix particle velocity ($\dot{u}_f > \dot{u}_m$). As a consequence, the interfacial friction stress between the fibre and the matrix in the slip region is $\tau_f = \tau_0$ whereas in this second region it is $\tau_f = -\tau_0$. This second region is termed the "reverse slip" region since the relative velocity of the fibre and the matrix has the opposite sense to that implied by the sense of the load. The front speed of the slip region η_1 and that of the reverse slip region η_2 are functions of C, φ, and k, and are obtained by solving Eq. (12).

4.4. Map of regimes of behavior

Regimes of pure slip, slip-stick and slip-reverse slip are determined by the material and loading parameters C, φ, and k. For the transition from slip-stick to pure slip, the friction stress within the stick zone (where $\dot{u}_f = \dot{u}_m$) in the stick-slip problem should reach the critical value of $\tau = \tau_0$. Thus from Eq. (10)

$$\frac{(\eta_1^2 + 2k\eta_1 - 1)(1 - C_U^2)}{2k(\eta_1(1 - C_U^2) + (1 - \eta_1^2)\sqrt{(C_U^2 + \varphi)(1 + \varphi)})} = 1, \tag{13}$$

where $\eta_1(C_U, \varphi, k)$ is obtained by solving Eq. (9b). Eq. (13) determines the critical velocity ratio, C_U. For a transition from the slip-stick regime to the slip-reverse slip regime, the friction stress within the stick zone (where $\dot{u}_f = \dot{u}_m$) in the slip-stick problem should reach the critical value of $\tau = -\tau_0$. Thus from Eq. (8):

$$\frac{(\eta_1^2 + 2k\eta_1 - 1)(1 - C_L^2)}{2k(\eta_1(1 - C_L^2) + (1 - \eta_1^2)\sqrt{(C_L^2 + \varphi)(1 + \varphi)})} = -1, \tag{14}$$

where $\eta_1(C_L, \varphi, k)$ is obtained by solving Eq. (9b). Thus C_L is determined.

Regimes of pure slip, slip-stick and slip-reverse slip are mapped in Fig. 3 in terms of the normalized wave speed ratio, C, and the modulus ratio, ϕ, for different values of the inverse loading rate parameter, k. When C is large (the wave speed of the fibre is much larger than that of the matrix), pure slip is expected. In the limit that $\varphi \to 0$ there are only two regimes: the pure slip and slip-stick regimes, depending on the value of C. A finite value of φ has to be exceeded in order for the three different regimes to be accessible for a specified k. As k increases, the pure slip regime and the slip-reverse slip regime shrink and the slip-stick regime enlarges.
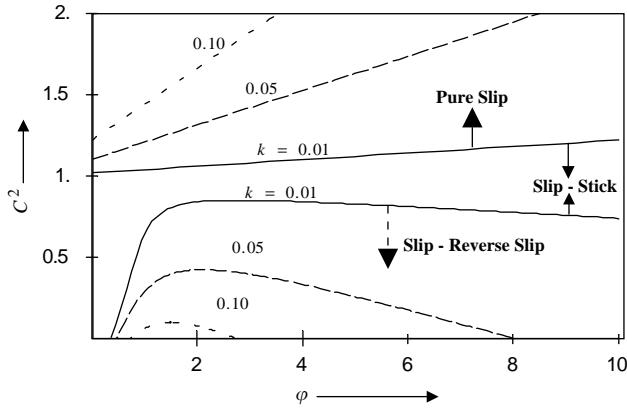
Fig. 3. Regimes of *pure slip*, *slip-stick* and *slip-reverse slip* mapped in the space of the normalized wave speed ratio C^2 and the modulus ratio φ for different k, the specified inverse loading rate.

4.5. The load–displacement relation

The relationship, $p(\delta)$, between the pullout load, p, and the displacement, δ, of the fibre end is determined through

$$\delta = \frac{1}{R_f} \int_0^{l_{\text{total}}(t)} (\varepsilon_{zz}^{\text{f}} - \varepsilon_{zz}^{\text{m}}) \, dz. \tag{15}$$

Normalizing by the displacement, $\delta_s = p^2/[2\tau(1+\varphi)E_f^2]$ for the static limit (Appendix B), one obtains thence the following displacements for each of the three different solution regimes:

Pure slip $(C > C_U)$:

$$\frac{\delta}{\delta_s} = 2k(1+\varphi)\frac{(\sqrt{1+k^2}(2C^2k - C + 2k\varphi) - 2k^2\varphi - C(C - k + 2Ck^2))}{C((Ck-1) - C\sqrt{1+k^2})}. \tag{16a}$$

Slip-stick $(C_L \leqslant C \leqslant C_U)$:

$$\frac{\delta}{\delta_s} = \frac{2k(1+\varphi)^2}{(C^2+\varphi)} \frac{\eta_1(2+\eta_1^2(C^2+\varphi)(1-2k\eta_2-\eta_2^2)+\eta_1\eta_2(1+C^2-2C^2k\eta_2-2k\eta_2\varphi))}{\eta_2^2(1+\eta_1\eta_2)(1+C^2\eta_1)}, \tag{16b}$$

where the front speeds η_1 and η_2 are obtained from Eq. (9).

Slip-reverse slip $(C \leqslant C_L)$:

$$\frac{\delta}{\delta_s} = 2k^2(1+\varphi)\left(\frac{1}{k} + \frac{4}{1+\eta_1} - \frac{2}{1+\eta_3}\right.$$
$$\left. - \frac{2\varphi(\eta_3^2 + \eta_1^2(C^2\eta_3^2+2) - 4\eta_1\eta_3)}{(1-C^2\eta_1^2)(1+C^2\eta_3^2)} - 2\right), \tag{16c}$$

where the front speeds η_1 and η_2 are obtained by solving Eqs. (12b) and (12c).
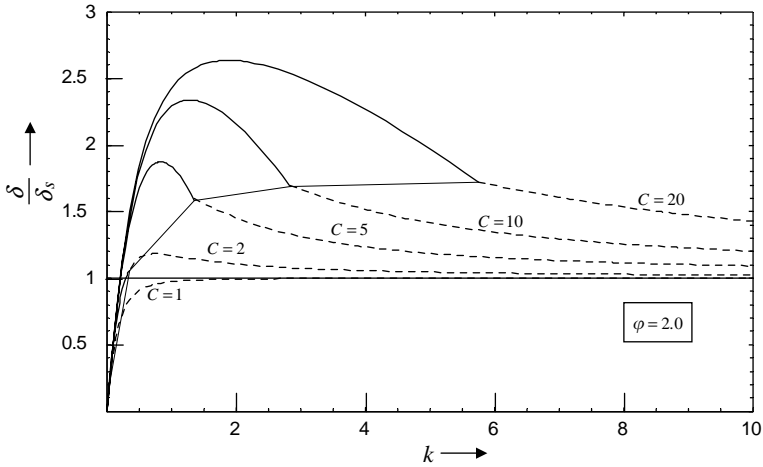
Fig. 4. The normalized pullout displacement δ/δ_s, where δ_s is the corresponding static value, as a function of k for various values of C. The solid curves are when the solution falls in the pure slip regime and the dashed lines are when the solution lies in the slip-stick regime. The normalized pullout displacement asymptotically reaches 1 as $k \to \infty$. Also shown is the contour line that demarcates pure slip from stick-slip.

The normalized pullout displacement, δ/δ_s, as a function of k is exemplified by Fig. 4 for the parameter value $\varphi = 2.00$. When $C \geqslant 1$, the map of Fig. 3 shows that, for any value of φ, there are only two possible regimes: for small k, pure slip (solid lines in Fig. 4); and for large k, slip-stick regime (dashed lines in Fig. 4). The static limit, $\delta = \delta_s$, is approached as $k \to \infty$. For rapid loading (small k), the dynamic response is relatively stiff ($\delta < \delta_s$); but for slow loading (intermediate and large values of k), inertial effects lead to an increased fibre-end displacement ($\delta > \delta_s$). When $C < 1$ (not shown in Fig. 4), one always has $\delta < \delta_s$.

Since the pullout displacement is a non-smooth function of k when $C > 1$, the transition from pure slip to slip-stick behavior could possibly be identified in experimental load–displacement data for different loading rates.

The prediction of fibre end displacements being enhanced in certain conditions by inertial effects is perhaps counterintuitive. Inspection of the solutions shows that it is accompanied by an increase in the length of the process zone (more particularly, of the domain in which slip occurs), with commensurate decrease in the stress gradients. This suggests that, when the fibre wave speed is relatively high, the inertia built up in the fibre enables the stress disturbance to propagate further before it is offset by frictional deceleration, than it would under static loading. An analogue of this effect is known for step loading of a fibre in a rigid matrix (Nikitin and Tyurekhodgaev, 1990; Cox et al., 2001).

4.6. Prevalence of inertial effects

For $C < 2$, inspection of Fig. 4 suggests that the onset of inertial effects can be correlated approximately with the rise of the curve δ/δ_s vs. k towards $\delta/\delta_s = 1$.

Introducing a threshold value, k_t, one can write that, as a rule of thumb, inertial effects are strong when $k < k_t$. For $C < 2$

$$k_t = 0.5 \quad (C < 2). \tag{17a}$$

For $C > 2$, inertial effects might be said to begin when δ/δ_s rises to 1.25 as k decreases from large values; for this condition, the asymptotic analysis of Appendix B for large k implies

$$k_t = 2.5 \frac{\left(C^2 - 1\right)\varphi}{(1 + \varphi)^2} \sqrt{\frac{1 + \varphi}{C^2 + \varphi}} \quad (C > 2). \tag{17b}$$

It is not difficult to meet these conditions experimentally.

5. Numerical confirmation

Numerical calculations based on finite element methods (FEM) were carried out to assess the accuracy of the shear lag approximation. Of particular interest are (1) the result that the rate of propagation of the stress disturbance is generally not the bar wave speed, but some lower speed that depends on the loading rate and the interfacial frictional stress; and (2) the separation of the deformation into distinct domains, including stick and reverse slip domains. Propagation at speeds lower than the bar wave speed has already been predicted for the loading of a bar in a rigid matrix (Nikitin and Tyurekhodgaev, 1990). However, the details of stress distributions in such a retarded front have not been investigated previously. The curious effect of reverse slip due to distributed friction is newly predicted.

5.1. Model formulation

The shear lag results were discussed for an axisymmetric system. However, because of the simplified representation of stress fields in the shear lag approximation, the shear lag results apply equally to a laminar, plane system, with a trivial redefinition of the radius parameter, R_f, and the volume fraction, f, i.e., $R_f = 2h$ and $f = h/H$, where h and H are the half-thickness of fibre layer and the total matrix/fibre model, as indicated in Fig. 5 (see Appendix A). Furthermore, when axial displacements dominate, the field equations of the plane and axisymmetric problems in the limit in which thin shell theory is valid become indistinguishable (Appendix A). Therefore, where the shear lag approximation is proven valid by simulations for a plane geometry, it is consistent to expect the validity to extend to the axisymmetric cases.

Therefore, confirmation by numerical methods is sought with a plane stress model, which was preferred here because it allowed a simpler treatment of interfacial friction in the FEM code being used.[1] Since the system is symmetric about $x = 0$, only the

---

[1] ABAQUS (5.8) by Hibbit, Karlsson & Sorensen, Inc. The numerical model includes 6400 4-point bilinear elements and 200 cohesive zone elements. The problem was solved using the direct-integration method. Automatic incrementing was used and each increment took an average of about 2.5 s (CPU time) to converge.
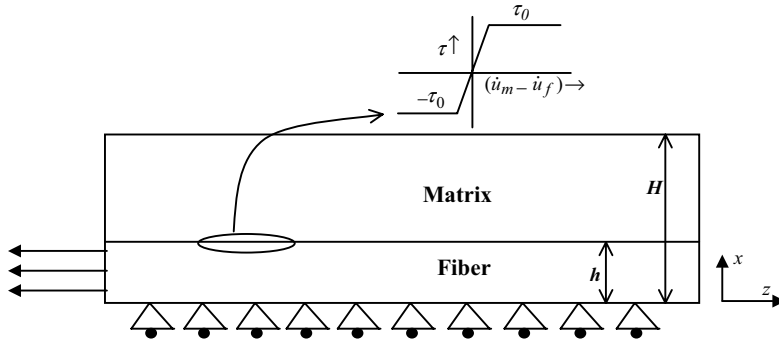
Fig. 5. Schematic of the FEM model and the cohesive law that describes the interfacial tractions during sliding in the numerical simulations.

top half is modeled with the normal displacement and the shear traction set to zero on this plane. The dimensions h and H were chosen to create a fibre volume fraction of 0.4. Friction was mimicked by cohesive elements that link the matrix and fibre along the bi-material. The friction law employed is

$$\tau_f = \begin{cases} \tau_0 & \text{(when } \dot{u}_m - \dot{u}_f > \omega), \\ \tau_0 \dfrac{(\dot{u}_m - \dot{u}_f)}{\omega} & \text{(when } -\omega \leqslant \dot{u}_m - \dot{u}_f \leqslant +\omega), \\ -\tau_0 & \text{(when } \dot{u}_m - \dot{u}_f < -\omega) \end{cases} \tag{18}$$

which is slightly different from the friction law used in the shear lag analysis (Eq. (1a)) in that the positive ($+\tau_0$) and negative friction ($-\tau_0$) regimes are linked by a linear transition regime of finite slope. This is necessary to avoid numerical difficulties associated with the jump discontinuity in Eq. (1a). (The difficulty of obtaining numerical solutions is further motivation for developing analytical approximations.) The parameter ω is chosen to be small, so that the effect on the solutions of not having a step change in the friction is negligible in most cases, with exceptions that affect only minor details of the solutions, as described below. In the region $-\omega \leqslant \dot{u}_m - \dot{u}_f \leqslant +\omega$, the interfacial friction stress $|\tau_f| \leqslant \tau_0$.

In the numerical simulations, Poisson's ratio for both fibre and matrix are set to zero. Under the assumption of uniform friction, the role of Poisson's ratio in the shear lag solutions is reduced to a scaling factor in certain elastic constants (Eq. (2) and Appendix A). Therefore, no generality is lost by this assumption in the numerical work, beyond that already lost by the restriction of uniform friction.

5.2. Character of the solutions

Pure slip: Fig. 6 shows particle velocities and shear stresses for a case that should lie in the pure slip regime, according to the shear lag analysis ($C^2 = 10$; $k = 0.1$; $\varphi = 1.11$;
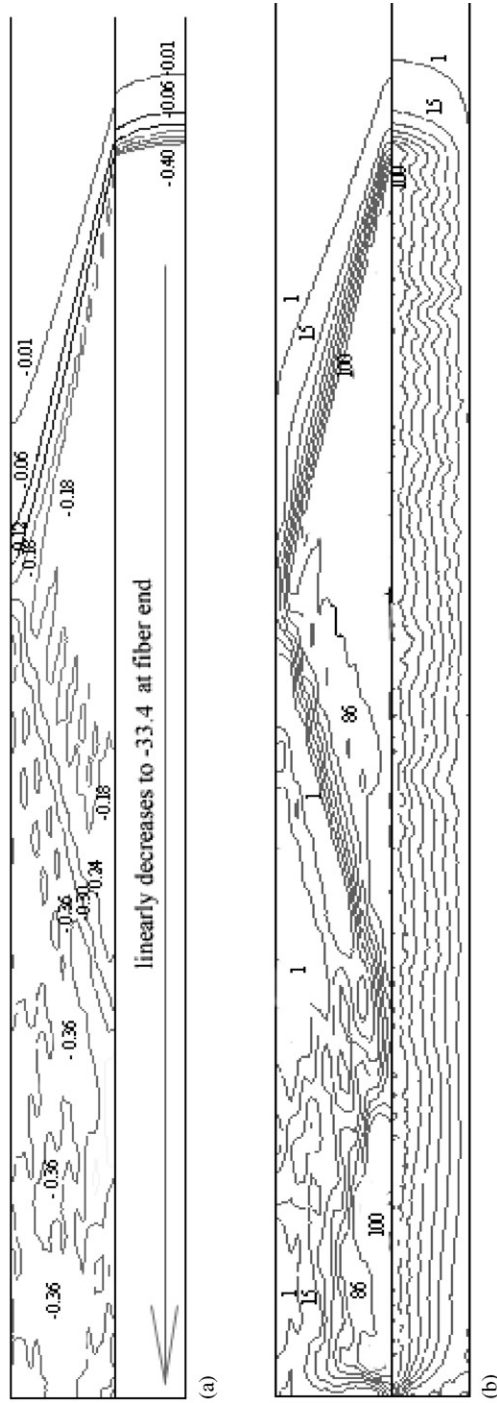
Fig. 6. FEM predicted contours of (a) the longitudinal velocity and (b) the shear stress for the pure slip case both within the fibre and in the matrix at time $T = 19.1$. The normalized parameters are $k = 0.1$, $\tau = 0.002$, $C^2 = 10$ and $\varphi = 1.11$.

$\tau = 0.002$—see Fig. 3). The velocity contours in Fig. 6a shows a clearly defined 2D structure in the fibre and matrix. In the matrix the leading contour indicates a straight wave front inclined at an angle to the interface. The contours of higher magnitude (0.06–0.18 m/s) appear to form a second straight front inclined at a smaller angle. This second front is characterized by high contour gradients that indicate a strong shock front. Far behind this zone the matrix velocity is fairly uniform, both in the thickness direction and in the axial direction. The velocity contours in the fibre are relatively uniform across the thickness although slightly inclined near the interface. Away from the wave front, the magnitude of the fibre velocity increases linearly as the distance to the wave front increases (not shown in Fig. 6a).

The angled front structures in the matrix are also evident in the shear stresses (Fig. 6b). The shear stress near the interface region remains 100 MPa, which is the specified interface friction strength, τ_0. Contours of lower shear stress (1–30 MPa) form the first wave front; larger shear stress contours (45–100 MPa) form the second front in a highly concentrated in a narrow band. In the matrix far behind the wave fronts, the shear stress does not reach a constant value independent of the vertical position x. Instead, it oscillates in the x-direction owing to reflection by the matrix boundary. The related transverse motion is neglected in the shear lag analysis.

The above observations are consistent with the literature on wave propagation near interfaces. While stress waves within the body of the fibre or the matrix do travel at characteristic wave speeds determined by the material properties, the velocity of propagation of the active frictional zone along the interface (also referred to as the trace velocity, c_{tr} (Eringen and Suhubi, 1975)), is not necessarily limited to the characteristic wave speeds. Instead, the trace velocity is related to the longitudinal and shear wave speeds in the fibre/or matrix by the inclination angles of the wave fronts. In the case analyzed, the longitudinal wave speed of the fibre is much faster than that of the matrix ($c_f/c_m = C = \sqrt{10}$). Therefore the trace velocity is much faster than the longitudinal wave speed of matrix, yet slightly slower than the longitudinal wave speed of the fibre: the friction zone front moves supersonically with respect to the matrix but subsonically with respect to the fibre. Two shock fronts, one associated with the longitudinal wave and the other associated with the shear wave, must exist in the matrix (Eringen and Suhubi, 1975). The inclination angles of the shock fronts are

$$\sin \beta_d = \frac{c_m}{c_{tr}} = \frac{1}{C\eta_{tr}} \quad \text{(longitudinal)}, \tag{19a}$$

$$\sin \beta_s = \frac{c_m / \sqrt{2}}{c_{tr}} = \frac{1 / \sqrt{2}}{C\eta_{tr}} \quad \text{(shear)}, \tag{19b}$$

where $\eta_{tr} = c_{tr}/c_f$. For the matrix, the external loading comes from interfacial shear stress caused by the friction. Therefore the shear shock front should be the stronger and the longitudinal shock front the weaker. This is confirmed in Fig. 6.[2] Furthermore,

---

[2] The numerical scheme used in this study cannot represent the abrupt jump associated with a shock, but the high gradients near the front of velocity profile are indicative of a shock-like field.

the calculated angles of inclination, 20° and 14°, imply via Eq. (20) that $\eta_{tr} = 0.92$. This is very close to the shear lag prediction, as will be discussed below.

Recent experimental observations seem to support the notion that the trace velocity is a function of the loading rate and the level of the interface friction stress (Rosakis and Owen, 2003). The shear crack propagation velocity along bimaterial interfaces also is a strong function of the loading rate (impact rate) (Needleman and Rosakis, 1999). The problem studied here can be interpreted alternatively as a dynamic shear cracking problem with zero fracture energy but a persistent wake frictional stress. Thus when the fibre radius decreases, the nominal wave speed within the fibre becomes increasingly dominated by the interfacial trace velocity and hence dependent on the loading rate and interfacial friction stress level.

Slip-stick: Fig. 7 shows the particle velocity and shear stress for parameters in which shear lag predicts behavior in the slip-stick regime ($C^2 = 0.1$; $k = 0.1$; $\varphi = 0.44$; $\tau = 0.002$—see Fig. 3). In Fig. 7a, a wave front of high contour gradients may be seen in the fibre, preceded by a long zone of low gradient (diverging contours). This unusual characteristic is associated with two distinct friction zones manifested by the shear stress contours (Fig. 7b). The first friction zone, in which the friction stress takes the limit value, $\tau_0 = 100$ MPa, is associated with slip between the matrix and fibre (Fig. 7a). The second zone, dominated by negative interfacial friction stresses of magnitude less than τ_0, is a stick zone (particle velocity continuous across the interface—Fig. 7a). [3] The negative sign of the interfacial friction clearly demonstrates that in this zone, the fibre is loaded by the matrix, despite the fact that it is the fibre end that is dynamically loaded.

No shock fronts are evident in the fibre in either Fig. 7a or b, although the front of the stick zone travels supersonically with respect to the fibre. This is probably due to the fact that the magnitude of the frictional stress decreases exponentially along the axial direction in the stick zone, which is again a consequence of the finite slope of the friction law used for the FEM simulations, Eq. (19). The shear lag model predicts a constant frictional stress of a magnitude smaller than τ_0 in this region (68 MPa in this particular case). Increasing the slope of the friction law would improve agreement with the shear lag result, but the computational cost increases exponentially.

Slip-reverse slip: The normalized parameters used for this case study are $C^2 = 0.025$; $k = 0.1$; $\varphi = 1.5$; $\tau = 0.002$. The velocity and shear stress contour plots for the numerical simulation are not shown here because they are not too much different from Fig. 7a and b. Because of the nature of the friction law used in the simulations (Eq. (18)), the shear stress at the interface is non-uniform in the stick zone in the slip-stick regime and therefore there can be no sudden transition to slip-reverse slip, as there is in the shear lag results. Numerical solutions in the anticipated slip-reverse slip regime therefore show a continued presence of the stick zone and gross features that are quite similar to solutions in the slip-stick regime. However, a reverse-slip zone, characterized by a uniform negative interfacial friction stress of $-\tau_0$ (-100 MPa), does exist within the

---

[3] In the FEM results, "stick" is defined by the relative velocity between the fibre and the matrix being smaller than ω (Eq. (19)).
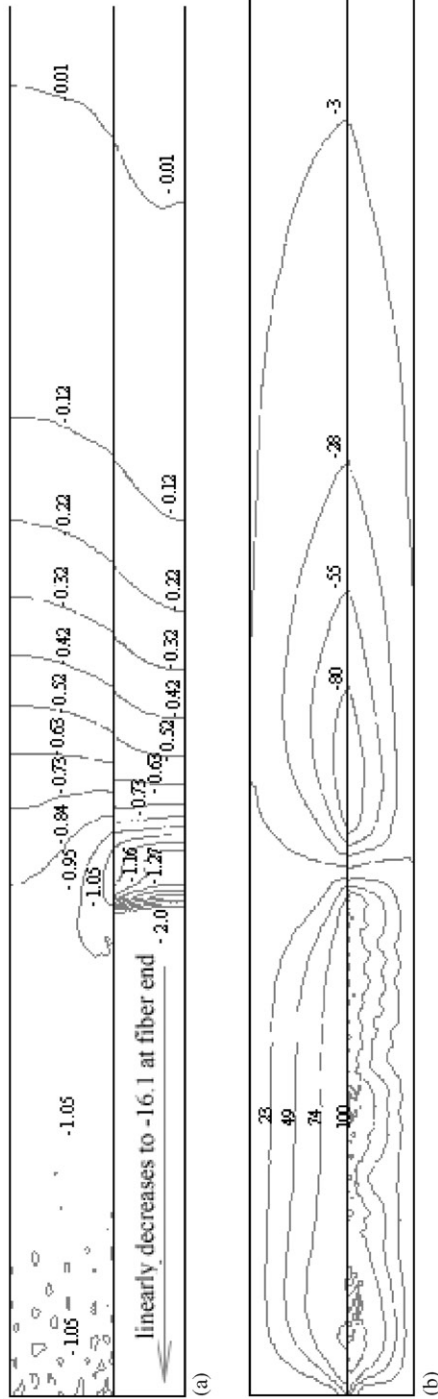
Fig. 7. FEM predicted contours of (a) the longitudinal velocity and (b) the shear stress for the slip-stick case both within the fibre and in the matrix at time $T = 8.3$. The normalized parameters are $k = 0.1$, $\tau = 0.002$, $C^2 = 0.1$ and $\varphi = 0.44$.

stick zone. This confirms the shear lag prediction as well as might be expected given the model formulation.

5.3. Confirmation of shear lag predictions

Despite the very complex 2D wave propagation characteristics in Figs. 6 and 7, the simple shear lag analysis does an excellent job of capturing the basic characteristics in an average sense. To demonstrate this, consider averages over the spatial variable, x, of the stress or particle velocity fields that are calculated in the FEM simulations. Fig. 8a compares such averages of the longitudinal particle velocity with the corresponding shear lag predictions, as functions of axial position at two different times, for the same case as Fig. 6. The general features of the pure-slip solution of the shear lag model are confirmed by the FEM results. The shear lag model also predicts quite accurately both the front location and the slope of the velocity profiles in the fibre. [4] It also predicts the form of the velocity variation in the matrix, including the locations of the domain boundaries, η_1 and η_2: predicted values are $\eta_1 = 0.32$ and $\eta_2 = 0.91$ by shear lag; and $\eta_1 = 0.32$ and $\eta_2 = 0.93$ by FEM. However, shear lag overestimates the magnitude of matrix velocity (inset of Fig. 8a). This is not surprising because in the shear lag model all the energy transmitted into the matrix is assumed to propagate only in the longitudinal direction, while in the FEM model part of the energy goes into the transverse direction as well. This error should decline as the fibre volume fraction rises.

Fig. 8b shows similar comparisons for the case of behavior in the slip-stick regime (the case of Fig. 7). The shear lag results agree well with the FEM results within the slip zone except that the velocity magnitude in the matrix is again over-predicted. However, owing to the finite slope of the cohesive law used in the FEM calculations, the numerical velocity profiles in the stick zone are different from the shear lag prediction. As mentioned above, the finite slope leads to an exponentially decaying velocity profile in the stick zone, while shear lag predicts a piecewise linear profile. The calculated speeds of the domain boundaries are $\eta_1 = 0.82$ and $\eta_2 = 1.63$ by shear lag; and $\eta_1 = 0.90$ and $\eta_2 = 2.23$ by FEM. In the slip-reverse slip regime, the calculated speeds of the domain boundaries are $\eta_1 = 0.68$ and $\eta_3 = 1.30$ by shear lag; and $\eta_1 = 0.77$ and $\eta_3 = 1.47$ by FEM; agreement is again reasonable.

5.4. Range of validity of the shear lag approximation

The question of when the shear lag approximation is accurate can be addressed in a practical way by looking at the predicted fibre end velocity, $\dot{U}_f(0,T)$, as a function of the applied stress, $\sigma_f(0,T)/E_f$. (For linear loading, the applied stress may also be regarded as a measure of time.) The results predicted by FEM and shear lag are plotted in Fig. 9a for the same case studies of Figs. 6 and 7 (pure slip and slip-stick). Evidently

---

[4] The small deviation from linearity in the FEM results near wave fronts (inset of Fig. 8a) is caused by the finite slope used in the cohesive law, which leads to an exponentially decaying velocity profile instead of a linear one.
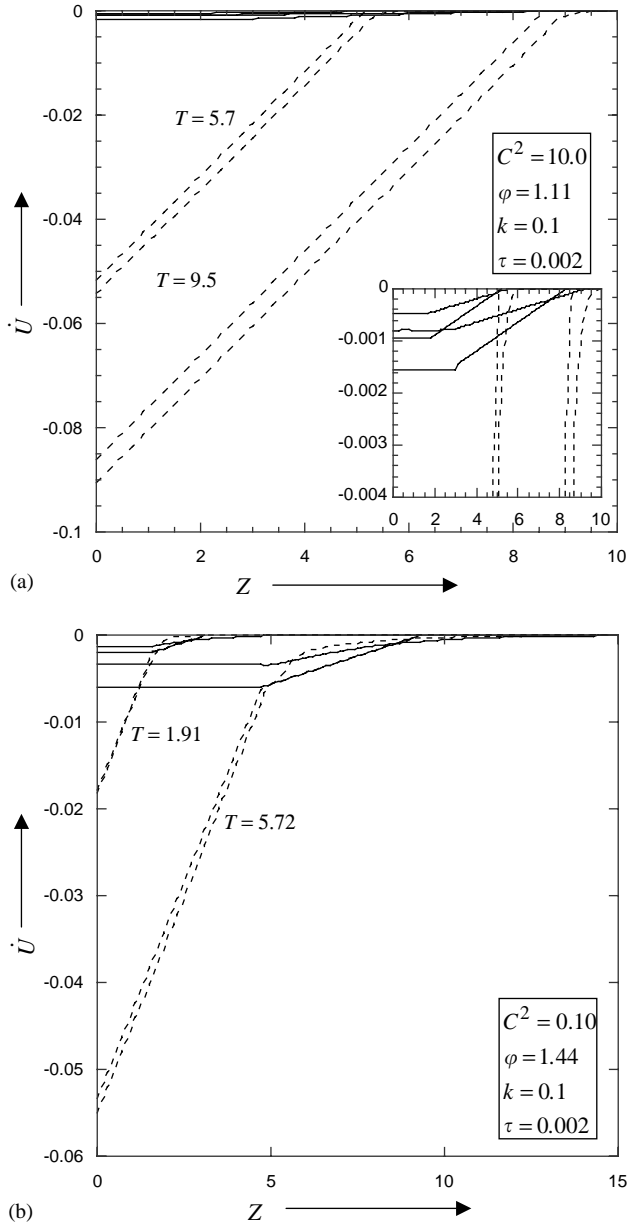
Fig. 8. Spatial variation of the particle velocity when (a) $C^2 = 10$ and $\varphi = 1.11$ and (b) when $C^2 = 0.1$ and $\varphi = 0.44$. This variation is shown for both the fibre (dashed lines) and the matrix (solid lines). Also comparison between FEM (thick lines) and shear lag (thin lines) are shown for two different times.
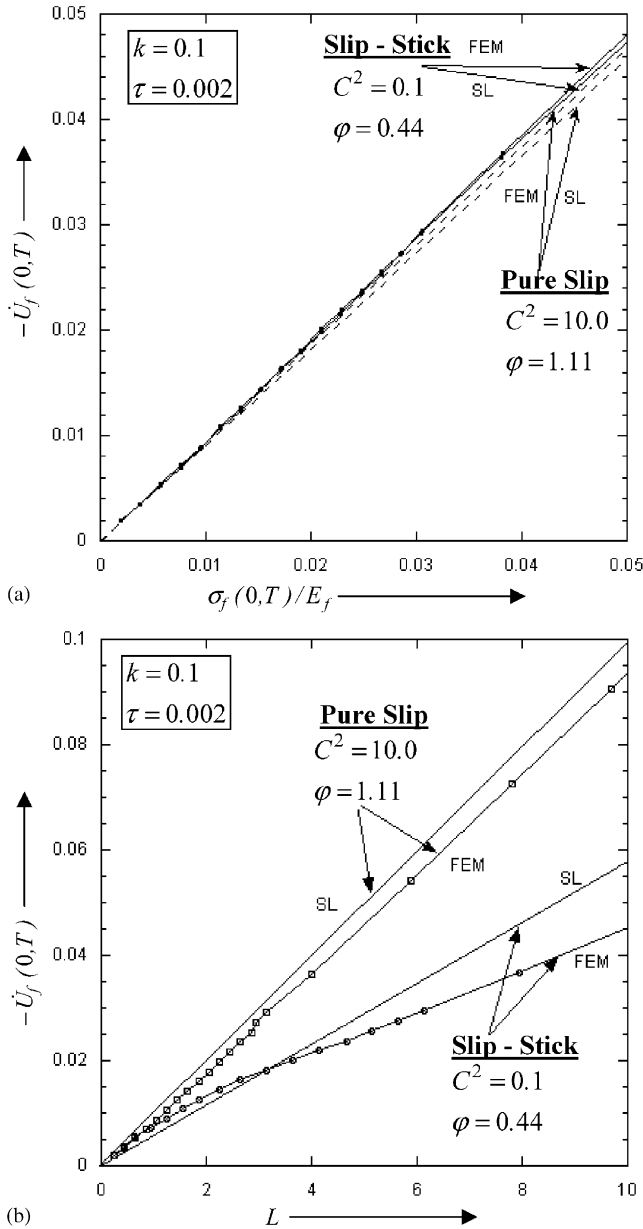
Fig. 9. The variation of the fibre end point velocity, $-\dot{U}_{\mathrm{f}}(0,T)$, as a function of the (a) applied boundary stress, $\sigma_{\mathrm{f}}(0,T)/E_{\mathrm{f}}$ and (b) the process zone length, $L = l_2(t)/R_{\mathrm{f}}$, for results obtained with shear lag (SL) and FEM. The variation is shown for two different sets of parameters, representative of pure slip and stick-slip conditions.

shear lag does an excellent job in both cases: for example, the slopes predicted by shear lag is $\eta_2 = 0.91$ for the pure slip case and $(\eta_1 + \eta_2 - 2k\eta_1\eta_2)/(1 + \eta_1\eta_2) = 0.93$ for the slip-stick case. The slip-stick velocity is always slightly higher than the corresponding pure slip velocity under the same inverse loading rate, k, and interface frictional strength, τ, due to the contribution of the stick zone. For predicting the load displacement history, shear lag appears to be useful from the onset of linear loading, regardless of whether the length of the process zone has exceeded the fibre radius.

If the length of the process zone is of interest, then conditions for the accuracy shear lag may be more restrictive. The shear lag and FEM predictions of the end displacement vs. the process zone length, $L = l_2/R_f = \eta_2 T$, are shown in Fig. 9b for the same case studies of Figs. 6 and 7 (pure slip and slip-stick). For the pure slip case, shear lag predicts a linear relationship between $\dot{U}_f$ and L, with slope $-\tau/2k$. The FEM results show that a constant slope that is almost identical to the shear lag prediction is established when L exceeds about 3. For the slip-stick case, shear lag again predicts a linear relation between $\dot{U}_f(0, T)$ and L, with slope $\tau(\eta_1 + \eta_2 - 2k\eta_1\eta_2)/(2k\eta_2(1 + \eta_1\eta_2))$. The FEM analysis predicts that a linear relationship is established when L is larger than 4. However, due to the finite slope in the friction law, FEM predicts a more extensive stick zone (see above) and therefore a larger value of η_2 (2.23) than that obtained with shear lag (1.63). From the pure slip case, where the effects of the friction law in the FEM simulations are minor, one infers that shear lag predicts the process zone length fairly accurately provided that it is greater than about 3–4 times the fibre radius.

6. Discussion

6.1. Nature of interfacial friction

The correct characterization of frictional sliding of a fibre embedded in a matrix remains an open issue. Several theoretical studies have examined the dynamics of sliding of two surfaces when the interfacial response is moderated by different friction behavior. Kosterin and Kragel'skii (1960) analyzed the stability of a one-degree-of-freedom elastic system and concluded that steady sliding is unstable when the rate of change of the friction stress with respect to velocity is negative. Rice and Ruina (1983) investigated steady frictional sliding when the interfacial shear stress has a fading memory of the velocity history and found under certain conditions instabilities in sliding occur. Adams (1995, 1998) investigated sliding of two different elastic half-spaces, and showed that this configuration is dynamically unstable due to the destabilization of the frictional slip waves. He also demonstrated that the stick-slip motion due to interfacial slip waves allows the bodies to slide with an apparent coefficient of friction, which is less than the specified interfacial coefficient of friction. For the simple friction law used in this study, a conclusion similar to that of Adams (1995, 1998) is reached in that stick-slip behavior can occur even under monotonic loading conditions. Further, the shear lag analysis points out that for a range of material and loading parameters, slip-reverse slip zones can also be established for a nominally tensile applied load on the fibre end.

6.2. More general loading histories

Inspection of the solutions to the wave equations shows that, as long as the loading history is piecewise linear, but not necessarily continuous, satisfaction of displacement continuity at the boundaries of domains that might arise is possible only if the displacements are quadratic functions of position and time. Thus if any loading history is represented by a piecewise linear approximation, some configuration of quadratic domains should exist as the solution. However, consideration of even quite simple loading functions, such as a bilinear function or a step function, shows that the domain pattern can become quite complicated, with domains of slip, stick, and reverse slip appearing and disappearing. Systematic prediction of the time evolution of the domains is challenging. Furthermore, since the domain patterns found in some simple trial cases appear to fragment as time passes (unlike the linear-loading case presented here, where they remain fixed in time), the suspicion arises that the response may be chaotic—small changes in the loading history may lead to unpredictable, large changes in the domain pattern at future times.

6.3. Relation to crack bridging by fibres

In static loading, the problems of fibre pullout (or push-in) and the bridging of a mode I matrix crack by fibres coupled to the matrix by friction are very closely related algebraically. Apart from a factor that distinguishes the fibre end displacement in the fibre pullout problem from the crack opening displacement in the crack bridging problem, which arises from energy considerations, the constitutive laws in the two cases are identical for similar physical models (Marshall et al., 1985; McCartney, 1989; Hutchinson and Jensen, 1990). In dynamic loading, in contrast, the two problems work out quite differently. The crack bridging problem is defined by a loading condition applied to the end of the process zone by the moving composite, with that composite motion determined by the far-field conditions of the propagating crack (Cox et al., 2001). The pullout problem is defined by a stress (or displacement) condition on the fibre end. In static loading, this leads to the same solutions. In dynamic loading, the evolution of wave motion is not the same. In particular, for linear loading in time, the solution to the bridged crack problem exhibits no stick or reverse slip domains (Cox et al., 2001). Furthermore, different conditions for the onset of strong inertial effects arise. The conditions obtained in (Cox et al., 2001) (Eqs. (16) and (18) in that work), amount to the following in the current notation:

$$k_t = 2\frac{C}{\varphi} \quad \text{(large } \varphi\text{)}, \tag{20a}$$

$$k_t = 2\frac{C}{\varphi^3} \quad \text{(small } \varphi\text{)}. \tag{20b}$$

which have little similarity to Eq. (17).

7. Conclusions

The fibre pullout problem is examined when the inertia of the fibre and the matrix are taken into account. Frictional sliding between the fibre and the matrix is described by a constant interfacial friction stress, the sign of which depends on the relative particle velocity of the fibre and the matrix. Analytical solutions are derived when the pullout load increases linearly in time.

Three regimes of behavior are distinguished, corresponding to different parameter values, in which the relative motions of the fibres and the matrix differ in two or three domains. The parameters include the ratio of the fibre and matrix wave speeds, the fibre and matrix moduli, and the loading rate. A map of the regimes has been determined analytically.

Numerical results encourage the use of the shear lag approximation in dynamic pullout problems, where quantities that have been averaged in the direction normal to the fibre axis are of interest. The shear lag approximation appears to be at least as viable for dynamic problems as it has proven for static problems. Good agreement in the load–displacement relation, for example, is found from the onset of linear loading. Agreement in the predicted length of the process zone is obtained as long as the process zone length is 2–4 times the fibre radius. Since the evolution of domains of slip, stick, and reverse slip can become very complicated for general loading histories, an analytical approach could be particularly valuable.

Because of the simple treatment of friction and Poisson's effect, all results here are equally applicable to fibre push-in, with appropriate changes of signs.

Appendix A. Elastodynamic equations

A.1. Axisymmetric problem

The elastodynamic equation that the fibre satisfies is (Graff, 1991):

$$\frac{\partial N_{\mathrm{f}}}{\partial z} = \frac{\rho_{\mathrm{f}}}{\hat{E}_{\mathrm{f}}} \frac{\partial^2 u_{\mathrm{f}}}{\partial t^2} - \frac{2\tau_{\mathrm{f}}}{R_{\mathrm{f}}}, \tag{A.1}$$

where

$$N_{\mathrm{f}} = \frac{2}{R_{\mathrm{f}}^2} \int_0^{R_{\mathrm{f}}} \sigma_{\mathrm{f}} r \, \mathrm{d}r$$

$$= \frac{E_{\mathrm{f}}(1 - \mu_{\mathrm{f}})}{(1 + \mu_{\mathrm{f}})(1 - 2\mu_{\mathrm{f}})} \left(\frac{\partial u_{\mathrm{f}}}{\partial z} + \frac{2\mu_{\mathrm{f}}}{R_{\mathrm{f}}^2} \int_0^{R_{\mathrm{f}}} \left(\frac{\partial w_{\mathrm{f}}}{\partial r} + \frac{w_{\mathrm{f}}}{r} \right) r \, \mathrm{d}r \right) \tag{A.2}$$

and where u_f, and w_f, are the fibre displacements in the longitudinal, and radial directions; R_f is the fibre radius and the areal fraction of the fibre cross sectional area; τ_f is the interfacial friction stress; and E_f, μ_f, and ρ_f are Young's modulus, Poisson's ratio, and the density of the fibre, respectively. In problems in which the fibre slides relative to the matrix, the coupling between the radial displacement and the longitudinal displacement is weak, because the radial displacement, w_f, will be much smaller than the axial displacement, u_f, over the zone of sliding. In the limit $w_f/u_f \to 0$, Eq. (A.1) simplifies to Eq. (2a). The radial and axial displacements can also be decoupled by assuming Poisson's ratio is zero, but this condition is unnecessary when w_f/u_f is small. The limit that w_f/u_f is small is included in this paper as one of the defining assumptions of the shear lag approximation. Similar assumptions for the matrix, i.e., w_m/u_m small, result in Eq. (2b).

A.2. Plane problem

The shear lag model for the plane or plate configuration is

$$\frac{\partial^2 u_f}{\partial z^2} + \mu_f \frac{\partial w_f}{\partial y} = \frac{\rho_f}{\hat{E}_f} \frac{\partial^2 u_m}{\partial t^2} - \frac{\tau_f}{h\hat{E}_f}, \tag{A.4a}$$

$$\frac{\partial^2 u_m}{\partial z^2} + \mu_m \frac{\partial w_m}{\partial y} = \frac{\rho_f}{\hat{E}_m} \frac{\partial^2 u_m}{\partial t^2} + \frac{f}{(1-f)} \frac{\tau_f}{h\hat{E}_m}, \tag{A.4b}$$

where $f = h/H$, h and H are the half-thickness of fibre layer and the total matrix/fibre model, as indicated in Fig. 7, and where u_f and w_f, are the displacements in the z and x directions respectively; $\hat{E} = E/(1-\mu^2)$ for plane stress and $\hat{E} = E(1-\mu)/((1+\mu)(1-2\mu))$ for plane strain. In the limit $w/u \to 0$, Eq. (A.4) simplifies to Eq. (2b) with a trivial redefinition of the radius parameter, $R_f = 2h$.

Thus the shear lag models for axisymmetric and plane problems are both represented by Eq. (2).

Appendix B. Static limit

The manner in which the dynamic solutions approach the static limit is interesting. In the limit, $k \equiv \tau_0 c_f t_0/(\sigma_0 R_f) \to \infty$, corresponding to very slow loading, the solution to the dynamic problem always lies in the slip-stick regime. Retaining the leading order term when $k \to \infty$ yields front speeds of

$$\eta_1 = \frac{1}{2k(1+\varphi)} - \frac{(1-C^2)\varphi}{4k^2(1+\varphi)^2\sqrt{(1+\varphi)(C^2+\varphi)}} + \Theta\left(\frac{1}{k^3}\right), \tag{B.1a}$$

$$\eta_2 = \sqrt{\frac{1+\varphi}{C^2+\varphi}} \tag{B.1b}$$

and the displacement fields are

$$U_f(Z,T) = \begin{cases} \tau \left(-\dfrac{Z^2}{2} + \dfrac{p}{E_f} Z - \dfrac{p}{E_f} \dfrac{T\varphi}{2(1+\varphi)} \sqrt{\dfrac{1+\varphi}{C^2+\varphi}} \right) & (0 \leqslant Z \leqslant \eta_1 T), \\[4mm] \dfrac{\tau\varphi}{(1+\varphi)} \left(-\dfrac{Z^2}{4k} \sqrt{\dfrac{C^2+\varphi}{1+\varphi}} + \dfrac{ZT}{2k} - \dfrac{T^2}{4k} \sqrt{\dfrac{1+\varphi}{C^2+\varphi}} \right) & (\eta_1 T < Z \leqslant \eta_2 T), \end{cases}$$

$$\tag{B.2a}$$

$$U_m(Z,T) = \begin{cases} \tau\varphi \left(\dfrac{Z^2}{2} - \dfrac{p}{E_f} \dfrac{T}{2(1+\varphi)} \sqrt{\dfrac{1+\varphi}{C^2+\varphi}} \right) & (0 \leqslant Z \leqslant \eta_1 T), \\[4mm] \dfrac{\tau\varphi}{(1+\varphi)} \left(-\dfrac{Z^2}{4k} \sqrt{\dfrac{C^2+\varphi}{1+\varphi}} + \dfrac{ZT}{2k} - \dfrac{T^2}{4k} \sqrt{\dfrac{1+\varphi}{C^2+\varphi}} \right) & (\eta_1 T < Z \leqslant \eta_2 T). \end{cases}$$

$$\tag{B.2b}$$

where $p(t) = \sigma_0 t/t_0$ is the boundary load. The friction stress within the slip zone is $\tau_f = \tau_0$ and the friction stress within the stick zone for large k is

$$\tau_f = \tilde{\tau} = \tau_0 \frac{(C^2-1)\varphi}{2k(1+\varphi)^{3/2}\sqrt{C^2+\varphi}}, \tag{B.3}$$

where the friction stress always satisfies $|\tau_f| < |\tau_0|$ and the boundary load $p(t) = \sigma_0 t/t_0$.

For $0 \leqslant Z \leqslant \eta_1 T$, the first two terms in (B.2a) and the first term in (B.2b) can be recognized as the displacements for the static case (e.g., appendix of Adams, 1995), for loading to the boundary load $p(t) = \sigma_0 t/t_0$. As the static limit is approached, the stick zone ($\eta_1 T < Z \leqslant \eta_2 T$) remains non-zero in length, but the stress gradient along it becomes vanishingly small. The front in the static limit can be identified with the limiting position of the boundary between the slip and stick domains in the dynamic case, $\eta_1 c_f t$. The pullout displacement δ of the fibre end, to leading order in k, is

$$\frac{\delta}{\delta_s} = 1 - \frac{1}{2k} \frac{(1-C^2)\varphi}{(1+\varphi)^2} \sqrt{\frac{1+\varphi}{C^2+\varphi}} + \Theta\left(\frac{1}{k^2}\right), \tag{B.4}$$

where $\delta_s = p^2(t)/(4\tau_0 E_f(1+\varphi))$ is its value in the static limit

Appendix C. Rigid matrix limit

In the limit of fibre pullout from a rigid matrix ($C \to 0$ and $\varphi \to 0$), the solution is in the stick-slip regime. The friction stress is identically zero within the stick zone

and thus

$$\tau_f = \begin{cases} \tau_0 & (0 \leqslant Z \leqslant \eta_1 T), \\ 0 & (\eta_1 T \leqslant Z \leqslant \eta_2 T). \end{cases} \tag{C.1}$$

The front speeds and the end-point displacement in this limit are

$$\eta_1 = \sqrt{1 + k^2} - k, \tag{C.2a}$$

$$\eta_3 \rightarrow \frac{1}{C}, \tag{C.2b}$$

$$\frac{\delta}{\delta_s} = 2k(\sqrt{1 + k^2} - k). \tag{C.2c}$$

These results are consistent with those presented in Refs. (Cox et al., 2001; Eringen and Suhubi, 1975).

References

Adams, G.G., 1995. Self-excited oscillations of tow elastic half-spaces sliding with a constant coefficient of friction. J. Appl. Mech. 62, 867–872.

Adams, G.G., 1998. Steady sliding of two elastic half-spaces with friction reduction due to interface stick-slip. J. Appl. Mech. 65, 470–475.

Cox, B.N., Sridhar, N., Beyerlein, I.J., 2001. Inertial effects in the pullout mechanism during dynamic loading of a bridged crack. Acta Mater. 49, 3863–3877.

Eringen, A.C., Suhubi, E.S., 1975. Elastodynamics—II. Linear theory. Academic Press, New Year.

Graff, K.F., 1991. Wave Motion in Elastic Solids. Dover, New York.

Freund, L.B., 1992. The axial force needed to slide a circular fiber along a hole in an elastic material and implications for fiber pull-out. Eur. J. Mech. A/Solids 11, 1–19.

Hutchinson, J.W., Jensen, H.M., 1990. Models of fiber debonding and pullout in brittle composites with friction. Mech. Mater. 9, 139–163.

Kosterin, Iu.I., Kragel'skii, I.V., 1960. Relaxation oscillations in elastic friction systems. In: Krushchov, M. (Ed.), Friction and Wear in Machinery. ASME, New York, pp. 111–134.

Marshall, D.B., Cox, B.N., Evans, A.G., 1985. The mechanics of matrix cracking in brittle-matrix fiber composites. Acta Metall. 33, 2013–2021.

McCartney, L.N., 1989. New theoretical model of stress transfer between fibre and matrix in a uniaxially fibre-reinforced composite. Proc. Roy. Soc. London A 425, 215.

Nairn, J., 1997. On the use of shear-lag methods for analysis of stress transfer in unidirectional composites. Mech. Mater. 26, 63–80.

Needleman, A., Rosakis, A.J., 1999. The effect of bond strength and loading rate on the conditions governing the attainment of intersonic crack growth along interfaces. J. Mech. Phys. Solids 47, 2411–2449.

Nikitin, L.V., Tyurekhodgaev, A.N., 1990. Wave propagation and vibration of elastic rods with interfacial frictional slip. Wave Motion 12, 513–526.

Parthasarathy, T.A., Marshall, D.B., Kerans, R.J., 1994. Analysis of the effect of interfacial roughness and sliding in brittle matrix composites. Acta Metall. Mater. 42, 3773–3784.

Rice, J.R., Ruina, A.L., 1983. Stability of steady frictional sliding. J. Appl. Mech. 50, 343–349.

Rosakis, A.J., Owen, D., 2003. Manuscript in preparation.

Sridhar, N., Cox, B.N., Dunn, C.L., Beyerlein, I.J., 2001. Mechanics of crack bridging under dynamic loads. MRS Fall Meeting Proceedings, Boston, Vol. 653, p. Z2.5.1.

Rockwell
Science Center

INERTIAL EFFECTS IN THE PULLOUT MECHANISM DURING DYNAMIC LOADING OF A BRIDGED CRACK

B. N. Cox[1]
N. Sridhar[1]
and
I. J. Beyerlein[2]

[1]Rockwell Science Center
1049 Camino Dos Rios
Thousand Oaks, CA 91360
U.S.A.

[2]Los Alamos National Laboratory
Los Alamos, New Mexico
U.S.A.

ABSTRACT

Inertial effects in the mechanism of fibre pullout during the dynamic propagation of a bridged crack are examined by reposing simple shear lag models of pullout as problems of dynamic wave propagation. The only coupling considered between the fibres and the matrix is uniform, rate independent friction – no debond energy is included. Analytical solutions are found for the coupled waves propagating in the fibres and the matrix away from the fracture plane of the bridged crack as the bridging tractions increase with time. These solutions yield the time-dependent relationship between the crack opening displacement and the bridging traction. Engineering criteria for inertial effects being significant are deduced by comparing the dynamic bridging traction law with its counterpart for static loading, which is recovered as a limit of the dynamic case. The criteria are evaluated for two crack cases: the asymptotic limit of a long, fully bridged matrix crack propagating unstably through a fibrous composite under remote tension; and and a finite crack partially bridged by stitches or rods that delaminates a double cantilever beam under the impetus of a flying wedge. In both cases, the rate of increase of the crack opening displacement appears to be sufficient for inertial effects to be pronounced in the bridging (pullout) mechanism. Expected trends of the significance of inertial effects with material and geometrical parameters are identified.

1.   Introduction

The pullout mechanism is the fundamental source of toughening and fracture resistance in many composites. In brittle matrix composites, reinforcing fibres that are weakly bonded to the matrix can survive the passage of matrix cracks, across which they then provide bridging tractions that shield the crack tip from the applied load. The main mechanism of load transfer from the fibres to the matrix is interfacial friction. In polymeric laminates reinforced through the thickness by stitches or rods, analogous pullout phenomena are observed, but on the scale of fibre tows, which may be 1 mm in diameter, rather than on the scale of individual fibres (10 – 100 μm).   Scale considerations aside, the mechanics of pullout are very similar in the two cases. Other systems in which bridging entities are coupled to a matrix by friction include so-called self-reinforced polycrystalline ceramics, in which elongated grains bridge cracks; and ceramic layered systems, in which fractured layers slide past one another during failure.

For mode I cracks, which will be the topic of this paper, the shielding effect created by the pullout phenomenon can be summarised by a bridging traction law that relates the stress in the bridging entities at the fracture plane, T, to the crack opening displacement, $2u$. To a very good approximation in many cases, the tractions in the bridging entities can be replaced by an equivalent continuous traction, p, that is to be applied to the entire bridged interval of the fracture surfaces (e.g., Cox and Marshall, 1994). Predicting the traction law, $p(u)$, becomes one of the central problems of crack bridging theory.

The mechanics of pullout and the resulting traction law have been much studied and are well understood for static loading. Simple analytical forms are available for $p(u)$ when the frictional coupling of the reinforcement to the matrix is uniform and slip extends over distances that are large compared to the reinforcement diameter (Marshall, Cox, and Evans, 1985; McCartney, 1987).   In this limit, which is a common case in ceramic composites and textile polymeric composites, the shear lag model of load transfer between the reinforcement and the matrix is accurate. Simple extensions of models of this class are also available to deal with small but nonzero levels of the work required to debond the reinforcement from the matrix prior to slip (Hutchinson and Jensen, 1990).

Given the relationship, $p(u)$, the characteristics of crack propagation can be computed by solving a bridged crack problem. In composites in which the bridging mechanism is most effective, the zone of bridging can be comparable to the crack length and much larger than features such as notches (Bao and Suo, 1992; Cox and Marshall, 1994) or, in the case of delamination cracks, the laminate thickness (Jain and Mai, 1995; Massabò and Cox, 1999). Crack propagation then does not follow Linear Elastic Fracture Mechanics, in the sense that there is no single material parameter such as toughness that correlates with the crack growth. Instead, the bridged crack problem is one of large scale bridging and the characteristics of propagation show features peculiar to the form of the traction law, $p(u)$ [Cox, 1991].

This paper extends existing models of the mechanics of pullout to high loading rates. An approach to evaluating a traction law that takes account of the inertia of the reinforcement

and the matrix is formulated as a direct extension of the elementary static loading model of McCartney (1987) and Marshall, Cox, and Evans (1985). The chosen base model for static loading has proven consistent with experiments in many material systems and has been the foundation of major advances in understanding damage in composites. The spirit of the present work is to seek equivalent insight into dynamic damage by incorporating the influence of inertia into the simplest credible model. Thus not all aspects of the micromechanics of pullout that could be important in some cases will be addressed. Instead, attention will be focused on identifying a characteristic time for the frictional pullout problem that will allow rapid assessment of when inertial effects will be important. Although analytical solutions are not available for general loading histories, the characteristic time can be expressed analytically in terms of the material and geometrical parameters of the problem. Immediate insight into the magnitude of inertial effects is implied.

In this first study, the friction stress is assumed to be constant and spatially uniform. The assumption of spatial uniformity has been very successful in accounting for data from static pullout tests in various material systems. One must recognize, however, that this is a strong assumption for dynamic pullout problems, with possible consequences for the qualitative nature of solutions. With direct experimental tests still pending, the following analysis presents useful results that at least establish limits for the particular case that the friction becomes spatially uniform.

All considerations in this paper are restricted to mode I loading. The derived dynamic traction law is used to analyse two illustrative cases. One is the formation of a fully-bridged, steady state (semi-infinite) crack, which is known by static considerations to propagate in an unstable manner (dynamically). This case is representative of large scale bridging problems. The other is the case of a dynamic crack with a bridging zone of fixed, limited length in a double cantilever beam specimen, which may propagate under either small or large scale bridging conditions. For both cracks, inertial effects are likely to be significant for plausible crack parameters.

2. Idealisation of the Bridged Crack problem

The crack propagation and pullout problems are depicted schematically in Fig. 1a. A matrix crack propagates on the plane $z = 0$ and is bridged by intact fibres in its wake. (For simplicity of expression, the term fibre from here on will be used to refer to bridging entities of any kind, including stitches, rods, and bridging grains.) Upon the passing of the crack tip, a debond crack propagates along the length of each fibre away from the fracture plane. Propagation of the debond crack is governed by the fracture energy associated with the separation of the matrix and the fibre at the debond crack tip and the work done against friction in displacing the debonded fibre along its axis. In many composites, the debond energy is small and pullout is dominated by friction over much of the range of pullout displacements. Therefore, in this first dynamic pull-out model the debond energy will be ignored.

The modeling assumptions to be used here for the dynamic crack propagation and pullout problems will in many respects be the same as those used in simple but successful models developed for the static problem. As for static loading, the crack propagation problem can be idealised by replacing the process zone by elastic composite material down to the fracture plane and representing the phenomena within the process zone by bridging tractions applied continuously on the fracture surfaces (Fig. 1b). The bridging tractions, p, are related to the axial stress, T, in the fibres at the fracture plane by $p = fT$, where f is the area fraction of the fibres on the plane $z = 0$. For aligned continuous reinforcement, f is also the volume fraction of the fibres. The total crack opening displacement, $2u$, in the idealisation should be defined as the difference in the actual displacement evaluated across the process zone and the displacement that would be expected if the material in the process zone were elastic.

In static models, the traction law, $p(u)$, is derived by considering the micromechanics of the phenomena occurring within the process zone, which is to say the micromechanics of frictional sliding. The micromechanical problem can be represented by a small volume of material, e.g., the material bounded by one of the dotted rectangles in Fig. 1a. The traction boundary conditions for the representative volume are usually set as follows. At $z = 0$, the matrix is traction-free, while the fibres sustain the axial traction T. At $z = l_s$, the strain in the fibres and the matrix must equal the average strain in the composite adjacent to the process zone ($z > l_s$). Shear tractions may arise along the vertical boundaries of the representative volume (parallel to z), but these are neglected.

In the problem of a crack propagating under static loading, the traction at $z = l_s$ for the representative volume associated with a fixed volume of material is assumed to rise from zero when the material is immediately behind the crack tip to increasing values as the material passes further back into the wake (Marshall et al., 1985). The tractions are not truly zero right at the crack tip, since the fibres are not stress-free, but assuming they are leads to reasonable results for the bridged crack problem as long as the fibres remain intact over sufficiently long distances into the crack wake. Then shielding of the crack tip is dominated by the bridging tractions acting in the further crack wake, where the boundary conditions are correct.

Further details of the micromechanical analysis of the static problem may be found in McCartney (1987) and the appendix to Marshall et al. (1985).

In dynamic loading, similar steps are followed, but the boundary conditions at the boundary of the process zone involve displacement and displacement rates as well as stress or strain conditions.

3. The Micromechanics of Dynamic Pullout

When friction is the only active force of resistance, no debond crack tip or crack tip field exists to be considered. The dynamic problem is one of waves propagating along a fibre and in the surrounding matrix, the two wave motions being coupled by friction.

The archetypal problem is illustrated in Fig. 2. A representative volume consists of cylindrical fibres of radius R and volume fraction f embedded in a matrix ($z \geq 0$). The fibre and the matrix have axial Young's moduli E_f and E_m and densities ρ_f and ρ_m respectively. The axial displacement, strain, and stress of the fibre and the matrix are denoted u_f and u_m, ε_f and ε_m, and σ_f and σ_m, respectively. The axial displacements will be assumed to be the only nonzero displacement components induced by loading and to be uniform across any section of the fibre or the matrix. Thus the displacement, strain, and stress in the fibre and the matrix are functions of z and t only. These are the usual assumptions of shear lag theory with the simplest conditions of elasticity (Poisson's effect omitted). They are consistent with assuming that the friction forces are constant (unaffected by fibre contraction or dilation due to axial stresses).

There is no initial bond between the fibres and the matrix. The fibres are coupled to the matrix by friction tractions, τ_f, which are assigned the following properties. If relative motion exists between the fibres and the matrix, then

$$\tau_f = \tau \qquad\qquad (\dot{u}_f < \dot{u}_m) \qquad\qquad\qquad (1a)$$

$$\tau_f = -\tau \qquad\qquad (\dot{u}_f > \dot{u}_m) \qquad\qquad\qquad (1b)$$

where a dot indicates time differentiation, τ is a positive constant, and $\tau_f > 0$ indicates friction tractions acting on the fibres in the positive z direction. When the fibres and the matrix are not in relative motion, the friction tractions may support stress gradients in the fibres and the matrix, provided that the required magnitude of τ_f does not exceed τ. Thus, by equilibrium considerations,

$$\left|\frac{\partial \sigma_f}{\partial z} - \rho_f \frac{\partial \dot{u}_f}{\partial t}\right| \leq \frac{2\tau}{R} \quad \& \quad \left|\frac{\partial \sigma_m}{\partial z} - \rho_m \frac{\partial \dot{u}_m}{\partial t}\right| \leq \frac{2f}{1-f}\frac{\tau}{R} \quad (\dot{u}_f = \dot{u}_m). \quad (1c)$$

Here the possibility is included that the matrix and the fibres have the same non-zero velocity and may also be accelerating together, although solutions of such generality will not be exhibited in this paper. With such a friction law, the dynamic wave equations describing those parts of the fibres and the matrix that are in relative motion may be written approximately as

$$\frac{\partial^2 u_f}{\partial z^2} = -\frac{2\theta\tau}{RE_f} + \frac{1}{c_f^2}\frac{\partial^2 u_f}{\partial t^2} \qquad\qquad\qquad (2a)$$

and

$$\frac{\partial^2 u_m}{\partial z^2} = \frac{2f}{1-f}\frac{\theta\tau}{RE_m} + \frac{1}{c_m^2}\frac{\partial^2 u_m}{\partial t^2} \qquad\qquad\qquad (2b)$$

where $\theta = 1$ if $\dot{u}_m > \dot{u}_f$ and $\theta = -1$ otherwise; and c_f and c_m are the bar wave velocities in the fibres and the matrix, given by

$$c_f = \sqrt{\frac{E_f}{\rho_f}} \qquad \& \qquad c_m = \sqrt{\frac{E_m}{\rho_m}} \qquad . \tag{2c}$$

The approximation of using the bar wave velocities rather than the longitudinal wave velocities in the z direction in the wave equations is consistent with the simplified treatment of stresses and strains and the assumed uniformity of the friction stress.

Boundary conditions in the dynamic case are as follows. At the fracture plane,

$$u_f(0, t) = 0 \qquad \& \qquad \sigma_m(0, t) = 0 \qquad (z = 0). \tag{3}$$

At the boundary of the process zone (limit of relative fibre/matrix motion),

$$u_f = u_m = u_c \qquad\qquad (z = l_s) \tag{4}$$

where u_c is the displacement of the adjacent intact composite; and conditions also exist on stress or strain and particle velocities. These further conditions depend on the nature of the loading history, which can be expressed as the function $\varepsilon(t)$, where ε is the strain in the z direction in the intact composite adjacent to the process zone boundary. The bridging traction, p, is related to ε by

$$p = \varepsilon E \tag{5a}$$

where the composite modulus, E, is given by

$$E = f E_f + (1 - f) E_m \qquad\qquad . \tag{5b}$$

In the depiction of Fig. 1a, the process zone boundary will propagate away from the fracture plane as $\varepsilon(t)$ rises. In the case to be considered in this paper, $\varepsilon(t)$ will be assumed to rise continuously and monotonically from zero. Placing the origin of time, $t = 0$, at the onset of nonzero $\varepsilon(t)$, the location of the zone boundary at time t may then be written[1]

$$l_s = \eta(t) c_m t \tag{6a}$$

where the function $\eta(t)$ depends on material and geometrical parameters and the form of $\varepsilon(t)$ and will be shown to be bounded by

$$0 < \eta(t) \leq 1 \qquad\qquad . \tag{6b}$$

---

[1] It is easy to show that all the ensuing results for linearly rising loading, $\varepsilon = kt$, are unchanged if η is defined instead by writing $l_s = \eta(t) c_f t$; and thus do not depend on the relative magnitudes of c_f and c_m.

For the loading conditions considered, the additional boundary conditions at $z = l_s$ are:

$$\dot{u}_f = \dot{u}_m = \dot{u}_c \qquad\qquad (z = l_s) \qquad\qquad (7a)$$

and

$$\varepsilon_f = \varepsilon_m = \varepsilon(t) \qquad\qquad (z = l_s). \qquad\qquad (7b)$$

If the load history, $\varepsilon(t)$, possesses discontinuities, e.g., a step load, then discontinuities in stress and particle velocity will also propagate at the boundary of the process zone (e.g., Achenbach, 1973; see also Appendix A).

4.   Composite Stress Rising Linearly in Time

In the limit of infinite matrix stiffness, the problem stated above is equivalent to that of an isolated, end-loaded rod that is constrained by uniform friction acting on the domain of its surface that is in motion. Fairly general solutions of this special problem were presented some time ago (Nikitin and Tyurekhodgaev, 1990; and much earlier papers cited therein). A summary adapted to the present context is provided in Appendix A. This limit case gives some indication of what might be expected for general loading histories (Section 5 below), but it does not contain much of the essential physics of the composite problem. When the matrix has finite stiffness, fewer analytical solutions can be found, because of the complicated evolution of the relative motion of the fibers and the matrix. One tractable case of representative interest for dynamic bridged crack problems is that of a load or bridging traction that increases linearly in time. Solutions of this problem are presented here and are used to assess inertial effects in two bridged crack problems in Section 6.

A linearly increasing load might give insight, for example, into bridging effects in a specimen in which substantial bending arises, such as a standard double cantilever beam delamination specimen. In such specimens, the crack profile is often approximately linear and the rate of increase of the bridging tractions at any point might also therefore be approximately linear if the crack propagates at approximately constant speed. The bridging traction at a particular material point might be expected to rise from zero as the delamination crack first passes until a peak value is reached, perhaps corresponding to bridging fibre rupture. Analytical results can be found for linearly increasing loads.

Let

$$\varepsilon(t) = kt \qquad\qquad (8)$$

where k is constant and all displacements and boundary tractions are zero for $t < 0$. In this case, $\theta = 1$ and the wave equations have the solutions

$$u_\mathrm{f} = -\frac{k}{c_\mathrm{m}}\alpha z^2 + [1 + 2\eta\alpha]\varepsilon z \tag{9a}$$

$$u_\mathrm{m} = \frac{k}{c_\mathrm{m}}\frac{1}{2\eta}z^2 + \frac{1}{2}[1 + 2\eta\alpha]\varepsilon l_\mathrm{s} \tag{9b}$$

where η is independent of time and satisfies

$$\alpha\eta^3 + \tfrac{1}{2}\eta^2 + \beta\alpha\eta - \tfrac{1}{2} = 0 \tag{9c}$$

with the dimensionless parameters α and β given by

$$\alpha = \frac{\tau c_\mathrm{m}}{E_\mathrm{f}Rk} \qquad \& \qquad \beta = \frac{f}{1-f}\frac{E_\mathrm{f}}{E_\mathrm{m}} \qquad . \tag{9d}$$

Analysis shows that Eq. (9c) has only one real root, which always lies in (0,1).

The particle velocities and the strains for $0 \le z \le l_\mathrm{s}$ are given by

$$\dot{u}_\mathrm{f} = [1 + 2\eta\alpha]kz \tag{10a}$$

$$\dot{u}_\mathrm{m} = [1 + 2\eta\alpha]kl_\mathrm{s} \tag{10b}$$

$$\varepsilon_\mathrm{f} = \left[1 + 2\eta\alpha\left(1 - \frac{z}{l_\mathrm{s}}\right)\right]\varepsilon \tag{10c}$$

$$\varepsilon_\mathrm{m} = \frac{z}{l_\mathrm{s}}\varepsilon \tag{10d}$$

Some important features of these results are as follows. The matrix particle velocity is uniform and increases in proportion to l_s. The fibre velocity rises linearly through the process zone. A strain concentration, $\varepsilon_\mathrm{f}/\varepsilon$, propagates in the fibre behind the process zone front, while the matrix strain in the process zone is always less than ε. The strain distributions and velocities beyond the process zone, $z > l_\mathrm{s}$, need not be specified, provided the composite strain ε obeys the condition Eq. (7) on the process zone boundary.

The displacement, u, to be used in defining the traction law, $p(u)$, is given by the common fibre and matrix displacement, $u_1 = u_\mathrm{f}(z = l_\mathrm{s}) = u_\mathrm{m}(z = l_\mathrm{s})$ at the boundary of the process zone minus the displacement expected if the process zone material were elastic:

$$u = u_1 - \varepsilon l_\mathrm{s}$$

$$= \frac{c_{\mathrm{m}}}{k} \alpha \eta^2 \varepsilon^2$$

$$= \frac{c_{\mathrm{m}} \alpha \eta^2}{kE^2} p^2 \qquad . \qquad (11)$$

Equation (11) constitutes the traction law for the case of linearly rising loads.

Further physical insight may be obtained by considering limiting loading rates. The limit of very fast loading corresponds to $k \to \infty$, whereupon $\alpha \to 0$ and $\eta \to 1$, since the first and third terms in Eq. (9c) become negligible. The disturbance then propagates at the bar wave speed in the matrix.

Static loading is represented by the limit $k \to 0$ or $\alpha \to \infty$, for which the first two terms of Eq. (9c) become small and one has the asymptotic solution

$$\eta \to \frac{1}{2\alpha\beta} \qquad . \qquad (12)$$

For this limit, substituting Eq. (12) into Eqs. (6a) and (11) yields

$$l_{\mathrm{s}} \to \frac{1-f}{f} \frac{E_{\mathrm{m}} R}{2\tau} \varepsilon \qquad (13a)$$

$$u \to u^{(\mathrm{st})} = \left(\frac{1-f}{f}\right)^2 \frac{E_{\mathrm{m}}^2 R}{4 E_{\mathrm{f}} \tau} \varepsilon^2 \qquad (13b)$$

which coincide with the results obtained by McCartney (1987).[2]

A criterion for inertial effects being significant can be deduced by comparing results for the dynamic and static cases. Equations (10) and (13b) show that for loads that increase linearly with time, the form of the traction law is identical in the static and dynamic cases and

$$\frac{u}{u^{(\mathrm{st})}} = 2\alpha\beta\eta \qquad . \qquad (14)$$

Thus the strength of the effects arising from inertia is measured by the degree to which the limit of Eq. (12) is not approached. This can be conveniently summarised by comparing the product $2\alpha\beta\eta$ to unity.

---

[2] Marshall et al. (1985) derived expressions with different coefficients, but those of McCartney are to be preferred, since they correspond to a proper definition of the crack displacement and are consistent with conservation of energy.

Asymptotic results for large and small β offer further insight into the criterion of Eq. (14).

Large β. Asymptotic analysis of Eq. (9c) shows that in the limit $\beta \to \infty$, $2\alpha\beta\eta \to 2\left[\sqrt{(\alpha\beta)^4 + (\alpha\beta)^2} - (\alpha\beta)^2\right]$ (second, third, and fourth terms of Eq. (9c) dominant), which is a function of $\alpha\beta$ and not of β separately; and Fig. 3a shows that this limit is approached quite closely for $\beta > 1$, which is expected, for example, for composites containing relatively stiff fibres ($E_f > E_m$). Fig. 3a also suggests that, as an engineering estimate, inertial effects are large when

$$\alpha\beta \equiv \frac{f}{1-f}\frac{\tau}{Rk}\frac{c_m}{E_m} \le 2 \qquad (\beta > 1) \qquad . \qquad (15)$$

Remembering that k^{-1} is the time constant of the loading, this condition can be rewritten

$$k^{-1} < 2\frac{1-f}{f}\frac{E_m}{\tau}\frac{R}{c_m} \qquad (\beta > 1) \qquad . \qquad (16)$$

Small β. The limit of a relatively stiff matrix can be analysed by observing that $\alpha \propto E_m^{\frac{1}{2}}$ while $\beta \propto E_m^{-1}$; and that Eq. (9c) in the limit $E_m \to \infty$ therefore yields the limiting solution $\eta \to (2\alpha)^{-1/3}$ (first and last terms of Eq. (9c) dominant). Thus $2\alpha\beta\eta \to (2\alpha\beta)^{2/3}\beta^{1/3}$ when $\alpha\beta \to 0$. Figure 3b shows this approximation for three values of $\beta \le 1$. While the limit is approached only for $\alpha\beta$ so small that $2\alpha\beta\eta$ is also small, it can nevertheless be used as the basis for engineering estimates of the condition for significant inertial effects, i.e., the first significant departure of $2\alpha\beta\eta$ from unity. The construction of Fig. 3b suggests that inertial effects will be significant when $\alpha\beta < 4(\alpha\beta)_1$, where $(\alpha\beta)_1$ is the value of the product $\alpha\beta$ at which the equation $(2\alpha\beta)^{2/3}\beta^{1/3} = 1$ is satisfied; i.e.,

$$\alpha\beta < \frac{2}{\beta^2} \qquad (\beta < 1). \qquad (17)$$

This leads to the criterion for significant inertial effects for composites with relatively stiff matrices that

$$k^{-1} < 2\left[\frac{1-f}{f}\right]^3 \frac{E_m^2}{E_f^2}\frac{E_m}{\tau}\frac{R}{c_m} \qquad (\beta < 1) \qquad . \qquad (18)$$

The criteria of Eqs. (16) and (18) coincide when $\beta = 1$.

Since $2\alpha\beta\eta < 1$ always, inertial effects increase the stiffness, dp/du, of the traction law for loads that increase linearly in time.

5.   Fibre Pullout from a Rigid Matrix

Analytical results have not been obtained for other loading histories for the composite problem. However, results for the pullout of a single fibre from a rigid matrix to which it is coupled by friction can be found for step loads as well as linearly increasing loads. While this limiting case omits much of the physics of the composite problem, its solutions offer some further insight into expected behaviour.

The problem considered for a rigid matrix is as shown in Fig. 4. The fibre is loaded on the fracture plane by tractions, $T(t)$, which can be represented by the boundary condition, $\varepsilon_0(t)$, for the axial strain in the fibre at $z = 0$. The response of the system that is of interest is wholly represented by the load point displacement, i.e., the displacement, $u_0(t)$, of the fibre at $z = 0$, since the matrix is rigid (motionless). Specifying a boundary condition on the fracture plane, rather than at the end of the slip zone, as for the composite problem, is preferred here because it allows a simpler statement of the step loading case.

Full solutions of this problem for step and linearly increasing loads are given in (Nikitin and Tyurekhodgaev, 1990) and Appendix A. For the present discussion, the most interesting features are the following.

While the load point displacement is reduced by inertial effects for linearly increasing loads, for a step load it is increased. For a linearly increasing load, $\varepsilon_0 = kt$,

$$\frac{u_0}{u_0^{(st)}} = 2\left[\frac{\sqrt{1+(kt_r)^2} - 1}{(kt_r)^2}\right] \tag{19}$$

at any time, where the characteristic time of the system, t_r, is given by

$$t_r = \frac{E_f R}{\tau c_f} \tag{20}$$

with the subscript "r" referring to the matrix being rigid. The ratio of Eq. (19) is plotted in Fig. 5. It is always less than unity. For a step function load $\varepsilon_0(t) = \varepsilon_0$, a constant for $t > 0$, all motion ceases when $t = \varepsilon_0 t_r$. At this point, $u_0 = 2u_0^{(st)}$: in contrast to the case of continually increasing loading, inertial effects double the displacement expected from loading statically to the same applied load.   Correspondingly, the strain gradient left in the fibre following dynamic step loading is exactly half that found after static loading.

One may now form a conjecture about the behaviour that should be expected in the composite problem (with a compliant matrix) if a linearly increasing load is followed by a period of constant loading. If the composite strain has been increased linearly to some value ε at time t_1, the matrix and fibre will both be moving at the boundary of the process zone with (positive) velocities given by Eqs. (10a) and (10b) evaluated at $z = l_s$. To achieve this state, the still-intact composite itself must be accelerating towards positive z,

maintaining the same velocity at $z = l_s$. If the composite strain is then fixed (no longer increasing), the composite will slow down and the matrix and fibre will begin to compress into the boundary of the process zone, under the influence of their inertia. This gives rise to quite complex motions, but the end result will be that the matrix will have displaced further relative to the fibre at the crack plane and the effective crack displacement, *u*, will have increased from its value at $t = t_1$. Analogy with the problem of the fibre being pulled out of a rigid matrix suggests that *u* might finally be larger than if the composite strain increased to the same level statically. However, this conjecture must be substantiated by numerical solutions.

6.   Implications for Dynamic Bridged Cracks

Whether or not dynamic effects in the pullout process will be important in the problem of a propagating bridged crack will depend on the loading rate for the bridging element (fibre, stitch, or rod). The fibre loading rate will depend on the crack propagation rate and the crack profile, which will depend on extrinsic factors such as the specimen shape and the loading configuration Taking account of all of these factors in a dynamic fracture problem presents quite a challenging calculation. However, the *onset* of significant dynamic effects can be evaluated without solving a dynamic fracture problem, but simply by considering the rate of change of displacements implied by static solutions when the applied load follows the time history of the dynamic case.

The likely magnitude of inertial effects is analysed for two crack problems in the following. To make use of the results of Section 4, the composite strain at the boundary of the process zone is assumed to rise linearly in time. Of course, this may not be the case – the dynamic crack propagation problem must be solved with a self-consistently derived dynamic traction law before the form of the rate of increase can be known - but in the cases considered it appears plausible.

6.1   Steady-State, Fully-Bridged Crack – the ACK Limit

Consider first a crack that would propagate under static conditions to the so-called ACK limit, in which a uniform applied stress comes into equilibrium with the bridging stresses provided by intact fibres in the far crack wake (Fig. 6). The ACK limit can be attained, for example, by a matrix crack in a ceramic matrix composite in an infinite specimen loaded in remote tension (Aveston, Cooper, and Kelly, 1971; Cox and Marshall, 1994). The static applied stress, σ_{ACK}, required to continue crack propagation in the ACK limit is invariant and the crack opening displacement in the far crack wake is uniform (Fig. 6). For a composite in which the bridging elements are coupled to the matrix by uniform friction, static analysis gives the following well-known results (e.g., McCartney, 1987; Appendix B in Massabò and Cox, 1999; Marshall and Cox, 1988). The critical stress, σ_{ACK}, is given by

$$\sigma_{ACK} = \left[\frac{3}{2} G_c \gamma \right]^{\frac{1}{3}}$$

(21)

where

$$\gamma = \frac{p}{\sqrt{u}} = \frac{2fE}{\left((1-f)E_{\mathrm{m}}\right)}\left[\frac{E_{\mathrm{f}}\tau}{R}\right]^{1/2} \qquad (22)$$

and G_{c} is the critical crack tip energy release rate for the matrix crack. The bridging stress approaches close to σ_{ACK} at a characteristic distance, l_{ACK}, from the crack tip given by

$$l_{\mathrm{ACK}} = \frac{\pi\overline{E}}{4}\left[\frac{3}{2}G_{\mathrm{c}}\right]^{1/3}\gamma^{-4/3} \qquad (23)$$

where $\overline{E}$ is an elastic constant that depends on the degree of anisotropy of the composite (defined, e.g., in Cox and Marshall, 1991). If the composite strain on the boundary of the process zone in the wake of the ACK crack is assumed to rise linearly in time, as in Eq. (8), then

$$k = \frac{\sigma_{\mathrm{ACK}}/E}{l_{\mathrm{ACK}}/c_{\mathrm{d}}} \qquad (24)$$

where c_{d} is the velocity of propagation of the delamination crack tip, which is assumed constant. Using Eq. (9d), the product $\alpha\beta$, which determines the magnitude of inertial effects for a linearly rising load, is then

$$\alpha\beta \approx \frac{\pi}{16}\frac{1-f}{f}\frac{\overline{E}}{E}\frac{E_{\mathrm{m}}}{E_{\mathrm{f}}}\frac{c_{\mathrm{m}}}{c_{\mathrm{d}}} \qquad \text{(ACK crack)} \qquad . \qquad (25)$$

For the square root traction law, $p \propto u^{1/2}$, the friction stress, τ, the fibre radius, R, and the critical energy release rate for the matrix, G_{c}, do not appear in this expression, although they appear in l_{ACK} and σ_{ACK} separately (Eqs. (21) and (23)).

For composites satisfying $\beta > 1$, the criterion for significant inertial effects in the bridging mechanism is that $\alpha\beta < 2$ (Eq. (15)). For elastically homogeneous composites, $\overline{E} \approx E$ and $\alpha\beta$ depends only on f and the ratio of the wave speed c_{m} and the crack velocity c_{d}. For example, for $f = 0.5$, $\alpha\beta$ will have a value less than 2 if $c_{\mathrm{d}} \geq (\pi/32)c_{\mathrm{m}}$. The velocity of a crack propagating in the ACK configuration has not previously been calculated. However, if the crack is fully bridged, as in an unnotched composite exhibiting multiple matrix cracking, crack growth is known to be unstable (e.g., Cox and Marshall, 1994), so that crack velocities satisfying $c_{\mathrm{d}} \geq (\pi/32)c_{\mathrm{m}}$ would appear to be feasible.

For composites satisfying $\beta < 1$ ($\beta \sim 0.1$ would appear to be easily attainable), inertial effects will appear at crack velocities lower by a factor of β^{2} (Eq. (18)).
Thus inertial effects are predicted to be significant for the ACK crack configuration for at least some common composites.

6.2   Wedge-Loaded Double Cantilever Beam

The double cantilever beam (DCB) specimen loaded dynamically by a flying wedge offers a relatively simple experimental approach to the mode I dynamic delamination problem (Fig. 7).   The test is especially attractive for studying the bridging effects supplied by through-thickness reinforcement (e.g., stitches or rods) in laminates.   An estimate of the likely role of inertia in bridging by stitches or rods follows.   In the context of this paper, the "fibre" refers in this case to a stitch or rod and the "matrix" to the laminate.

For an increasing bridging traction law, i.e., a law for which $dp/du > 0$, the crack surfaces at the crack tip are predicted to come into contact in the DCB specimen under static loading at a certain crack length (Massabò and Cox, 2000).   The crack will be arrested at this point, since the crack tip energy release rate must then vanish.   Furthermore, the crack surfaces remain in contact when the applied load is increased so that the crack remains arrested and failure eventually ensues by another mechanism.   An analogue of this interesting phenomenon of crack tip closure and crack arrest, which is a result of large scale bridging effects, might also be anticipated in dynamic loading (Beyerlein et al., 2000).   An interesting case therefore is to consider the rate of opening of a crack that has arrested and is being loaded further by the flying wedge.

Simple analytical expressions for the opening displacements are available in the static case for a linear bridging law, $p = \beta_3 u$, and a composite with moderate levels of elastic anisotropy.   If l is suitably large in Fig. 7, then the bending moment at the notch root, $x = 0$, will dominate over the shear load at $x = 0$.   In this case, the crack will arrest after propagating a distance a_1 given by (Massabò and Cox, 2000)

$$a_1 = \frac{\pi}{2b} \tag{26}$$

where

$$b = \left[\frac{\beta_3}{4E_x' I_d} \right]^{\frac{1}{4}} \tag{27}$$

with $E_x' = E_x/(1 - \nu_{xy}\,\nu_{yx})$ (plane strain conditions assumed) and $I_d = 12/h^3$, with h the laminate half-thickness (see Fig. 7 for coordinates and dimensions).   Insight into the magnitude of dynamic effects in the bridging phenomenon can be gained by considering the rate at which the crack opens at the end of the bridging zone ($x = 0$ in Fig. 7) under the influence of the wedge load when the crack length is fixed at $a = a_1$.   From the results of Massabò and Cox (2000), the load point displacement, δ, at the point where the wedge

contacts the specimen can be related for large l to the crack opening displacement, $\widehat{u}_0$, at $x = 0$ (the last intact bridging element) by (see Appendix B)[3]

$$\delta = \frac{2}{\sqrt{3}}\left[\frac{\beta_3 l^4}{E_x' h^3}\right]^{1/2}\widehat{u}_0 \qquad . \tag{28}$$

The composite strain at the boundary of the process zone at $x = 0$ is

$$\varepsilon = \frac{\beta_3 \widehat{u}_0}{E_3} \tag{29}$$

while, for a wedge subtending an angle 2ϕ and moving at velocity v_w,

$$\frac{d\delta}{dt} = v_w \tan\phi \qquad . \tag{30}$$

If v_w is constant, Eqs. (28 – 30) yield a linear rate of increase for ε, where, in the notation of Eq. (8),

$$k = \frac{\sqrt{3}}{2}\left[\frac{E_x' \beta_3 h}{E_3^2}\right]^{1/2}\frac{h v_w \tan\phi}{l^2} \tag{31}$$

and thence

$$\alpha\beta = \frac{2}{\sqrt{3}}\frac{f}{1-f}\frac{\tau}{\sqrt{E_x' \beta_3 h}}\frac{E_3}{E_m}\frac{l^2}{hR}\frac{c_m}{v_w \tan\phi} \qquad \text{(wedge-loaded DCB)} . \tag{32}$$

Here c_m refers to the bar wave speed in the laminate ("matrix") in the through-thickness direction. The modulus E_3 is that of the composite (with stitches or rods) in the through-thickness direction, while E_m is that of the laminate (without stitches or rods) in the same direction. If f is small, which is the usual case, $E_m \approx E_3$; and the factor $f/(1-f) \approx f$, with $f = 0.05$ a typical value. Experimental data for typical stitched laminates show $\beta_3 \approx 100$ MPa/mm (Massabò et al., 1998; Turrettini, 1996). Taking $E_x' = 60$ GPa and $h = 6$ mm, the factor $\sqrt{E_x' \beta_3 h}$ has the representative value 6 GPa. The ratio $\tau/\sqrt{E_x' \beta_3 h}$ will have typical values $\sim 10^{-3} - 10^{-2}$ ($\tau = 6 - 60$ MPa). With $l = 20$ mm, $R = 1$ mm, and $\phi = 20°$, for example, Eq. (32) reduces to the particular numerical estimate

---

[3] These estimates are based on results for a linear bridging law. Equivalent results for a quadratic law, $p \propto u^{1/2}$, which is expected for static loading of fibers coupled to the matrix by friction, have not been published. However, the estimated times for reaching a given displacement and composite strain are likely to be of the same order of magnitude as for a linear law.

$$0.01\frac{c_m}{v_w} \le \alpha\beta \le 0.1\frac{c_m}{v_w} \qquad . \qquad (33)$$

For composites for which $\beta > 1$ (including most stitched laminates), inertial effects will be significant (i.e., $\alpha\beta < 2$) provided $v_w > c_m/200$ ($\tau = 6$ MPa) or $v_w > c_m/20$ ($\tau = 60$ MPa).

Such wedge velocities are eminently attainable and inertial effects in the bridging law are likely to be significant in the wedge-loaded DCB test.

7. Discussion

7.1 Shear Lag Approximation

The solutions presented here are based on the approximation that displacements are functions of z only. For static loading, this is an accurate approximation as long as the slip distance is large compared to the fibre diameter (Hutchinson and Jensen, 1990). The condition that the slip zone length should be much larger than the fibre diameter will be satisfied if the friction stress, τ, takes values typical in brittle matrix composites or polymer textile composites.

For dynamic problems, the conditions under which solutions that depend on z only will be accurate have not yet been studied. The solutions presented in this work will at least provide tentative limits against which three-dimensional numerical solutions can be compared.

Whether the approximation that displacements depend on z alone is accurate will also depend on the presence of a nonzero debond energy (energy required for separation of the fibres and the matrix). Here the debond energy was assumed to be zero (fibres and matrix already chemically separated). Dynamic analysis of materials in which the debond energy is not small will be significantly more complicated.

7.2 Nature of the Friction Stress

Recent, unpublished experiments on the dynamic push-in of a thin plate (plane strain analogue of the push-in of a rod or fibre) have shown some interesting characteristics that suggest more complicated states of friction than those assumed here (Rosakis and Owen, 2001). In the push-in tests, dynamic strain field measurements revealed indirect evidence that the friction stress was not uniform, but consistent rather with dynamic stick-slip behavior. The velocity of the advance of the stress disturbance in the thin plate exceeded the shear wave speed and was always less than the bar wave speed (i.e., was intersonic), consistent with the predictions of the present model. However, the velocity appeared to take only two discrete values – the bar wave speed or $\sqrt{2c_s}$, where c_s is the shear wave speed of the fibre. This speed is associated by prior theoretical work with the condition for energy consistency of an intersonic shear delamination crack (Lambros and Rosakis,

1995; Liu et al., 1995). The simple assumption of spatially uniform friction in the present model leads in contrast to a continuous spectrum of possible velocities.

The friction characteristics during push-in tests are very likely related to Poisson's effect, which leads under the sense of loading for the push-in case to predicted interpenetration of the contacting surfaces in the wake of the friction front. The interpenetration vanishes for only one special velocity, $\sqrt{2c_s}$, which is close numerically to that observed in the new experiments. One might infer that this velocity is selected in the push-in experiment to minimise the energy of the system by avoiding the strong friction that would be caused by a driving force for interpenetration. In bridged cracks opening in mode I, the fibre (or reinforcement) is being pulled out of the matrix. In this case, Poisson's effect will usually tend to separate the sliding surfaces; there may not be a selection mechanism for any particular velocity. Further experiments will be of great interest.

7.3   Other Physical Aspects of the Solutions

For stitched laminates, one of the cases assessed in Section 5, the requirement that the slip or process zone, l_s, be large compared to the fibre (stitch) diameter (typically 1 mm) implies that it will also be comparable to or greater than a typical laminate half-thickness, h (~ 6 mm). When the value of l_s predicted for an infinite body would exceed h, stress waves will reflect from the laminate surface, complicating the micromechanics of the process zone. These effects are not studied here.

A feature of the wave solutions for loads that increase monotonically from zero with time is that stress disturbances propagate away from the fracture plane at velocities other than either the matrix or fibre bar wave speed. This is the case for both the composite problem (Section 4) and the problem of a fibre being pulled out of a rigid matrix (Nikitin and Tyurekhodgaev, 1990; Appendix A). In the composite problem, the front velocity is always less than the matrix bar wave speed. The possibility exists that the front velocity will exceed the bar wave speed in the fibres, but numerical checks show that this can happen only for very high (and unlikely) ratios of fibre to matrix density.

No account has been attempted here of the conditions under which the strain at the boundary of the process zone, ε, can be expected to rise linearly in time, apart from the special case of a wedge loaded DCB specimen. The relationship between ε and the far field conditions in a dynamically loaded body will generally be complicated and revealed only by computational solutions of the dynamic stress propagation problem for the whole body, including the process zone. The particular problem of finding far field loading conditions that will result in $\varepsilon(t)$ being linear in time is very challenging.

8.   Conclusions

Some analytical results have been presented for the problem of bridging by the mechanism of fibre pullout when the inertia of the fibre and the matrix are taken into account. Simple criteria have been specified for significant inertial effects in the bridging mechanism in representative mode I crack propagation problems. Inertial effects in the

bridging mechanism will often be significant for a matrix crack propagating dynamically in the steady state ACK limit in a brittle matrix continuous fibre composite or delamination in laminates reinforced by through-thickness stitching or rods.

Significant inertial effects are favoured by low fibre volume fraction, low friction stress, low matrix bar wave speed, and low fibre modulus; and high fibre diameter and high matrix modulus. If the fibre modulus is high enough (relative to the matrix modulus), the criterion for inertial effects becomes independent of fibre modulus. The matrix density enters the criterion only through the matrix bar wave speed. The criterion is always independent of the fibre density.

For pullout or bridging stresses that rise linearly in time, the instantaneous crack displacement is less in the presence of inertial effects than it would be under static loading to the same bridging stress. However, solutions for pullout from a rigid matrix suggest that, if the bridging stress rises rapidly and is then held at a constant value, the crack displacement when all particle motion finally stops will be greater than it would have been under static loading to that stress level. Thus regimes of both hardening and softening of the bridging traction law due to inertial effects can be expected in bridged crack problems.

Acknowledgments

References

J. D. Achenbach, *Wave Propagation in Elastic Solids*, North-Holland, 1973, pp. 138-143.

J. Aveston, G. A. Cooper, and A. Kelly, "Single and Multiple Fracture. The Properties of Fibre Composites," Conf. Proc., National Physical Lab., IPC Science and Tech. Press Ltd., pp. 15-24 (1971).

G. Bao and Z. Suo, "Remarks on Crack Bridging Concepts," *Applied Mech. Review*, **24**, 355-366 (1992).

I. Beyerlein, N. Sridhar, and B. N. Cox, "Large Scale Bridging Effects in Dynamic Delamination," to be submitted to *J. Mech. Phys. Solids.*

B. N. Cox, "Extrinsic Factors in the Mechanics of Bridged Cracks," *Acta Metallurgica et Materialia* **39**, 1189-1201 (1991).

B. N. Cox and D. B. Marshall, "Stable and Unstable Solutions for Bridged Cracks in Various Specimens," *Acta Metall. et Mater.* **39**, 579-89 (1991).

B. N. Cox and D. B. Marshall, "Concepts for Bridged Cracks in Fracture and Fatigue," Overview No. 111, *Acta Metall. Mater.* **42**, 341-63 (1994).

J. W. Hutchinson and H. M. Jensen, "Models of Fiber Debonding and Pullout in Brittle Composites with Friction," *Mechanics of Materials*, **9**, 139-163 (1990).

L. K. Jain and Y.-W. Mai, "Determination of Mode II Delamination Toughness of Stitched Laminated Composites," *Composites Sci. and Tech.*, **55**, 241-253 (1995).

J. Lambros and A. Rosakis, "Shear Dominated Transonic Interfacial Crack Growth in a Bimaterial – I. Experimental Observations," *J. Mech . Phys. Solids*, **43**, 169-188 (1995).

C. Liu, Y. Huang, and A. J. Rosakis, "Shear Dominated Transonic Interfacial Crack Growth in a Bimaterial – II. Asymptotic Fields and Favourable Velocity Regimes," *J. Mech. Phys. Solids*, **43**, 1890-206 (1995).

L. N. McCartney, "Mechanics of Matrix Cracking in Brittle-Matrix Fibre-Reinforced Composites," *Proc. Roy. Soc. Lond.* **A409**, 329-350 (1987).

D. B. Marshall and B. N. Cox, "A J-Integral Method for Calculating Steady-State Matrix Cracking in Composites," *Mechanics of Materials* **7**, 127-33 (1988).

D. B. Marshall, B. N. Cox and A. G. Evans, "The Mechanics of Matrix Cracking in Brittle-Matrix Fiber Composites," *Acta Metall.* **33**, 2013-2021 (1985).

R. Massabò and B. N. Cox, "Concepts for Bridged Mode II Delamination Cracks," *J. Mech. Phys. Solids*, **47**, 1265-1300 (1999).

R. Massabò and B. N. Cox, "Unusual Characteristics of Mixed Mode Delamination Fracture in the Presence of Large Scale Bridging," *Mechanics of Comp. Mater. and Struct.*, in press.

L. V. Nikitin and A. N. Tyurekhodgaev, 1990, "Wave Propagation and Vibration of Elastic Rods with Interfacial Frictional Slip," *Wave Motion*, **12**, 513-526.

A. Rosakis and D. Owen, 2001, California Institute of Technology, Pasadena, California, unpublished work.

A. Turrettini, Masters Thesis, University of California, Santa Barbara, 1996.

Appendix A. Fibre Pullout from a Rigid Matrix.

Solutions are exhibited here to the problem described in Fig. 4 and related text.[4] Since the matrix is rigid, it experiences no motion. The motion of the fibre is governed by the wave equation of Eq. (2a). The problem is defined by stating the value of the load applied to the end of the fibre at $z = 0$, rather than the matrix strain at the end of the process zone.

Boundary Conditions for Front of Propagating Disturbance

Let the location of the front limiting the extent of the stress disturbance caused by waves propagating along the fibre be written $l_r = \eta c_f t$, where the applied load is turned on at time $t = 0$. (The subscript "r" is used for this problem as a mnemonic for "rigid" matrix.) The jump in the stress, $\Delta \sigma_f$, and jump in particle velocity, $\Delta \dot{u}_f$ (where $\dot{u}_f \equiv \partial u_f / \partial t$), across the front, i.e., from $z > \eta c_f t$ to $z < \eta c_f t$, must satisfy the energy-conserving relation expected from integration of the impulse across the front, namely (see, e.g., Achenbach, 1973)

$$\Delta \dot{u}_f = -\frac{\Delta \sigma_f}{\rho_f v_0} \tag{A.1}$$

where v_0 is the velocity of the front, $v_0 = c_f \partial(\eta t)/\partial t$. To ensure integrity of the fibre, the displacement must be continuous across the front, i.e.,

$$u_f(z,t) = 0 \qquad\qquad (z \to l_r^-) \qquad . \tag{A.2}$$

Two front conditions may now be distinguished. If a stress discontinuity exists at the front, $\Delta \sigma_f > 0$, then kinematic considerations along with Eq. (A.1) necessitate that (see, e.g., Achenbach, 1973)

$$\eta = 1 \qquad\qquad (\Delta \sigma_f > 0) \tag{A.3a}$$

or, equivalently, $v_0 = c_f$. If the stress is continuous across the front, i.e., $\sigma_f = 0$ at $z = z_f$, then the velocity of the front remains indeterminate:

$$0 < \eta < 1 \qquad\qquad (\Delta \sigma_f = 0) \qquad . \tag{A.3b}$$

Solutions obeying both Eqs. (A.3a) and (A.3b) will be demonstrated in the following.

---

[4] See also (Nikitin and Tyurekhodgaev, 1990). Dynamic solutions are developed here for the cases of particular interest to the delamination problem, with emphasis on the relationship between the dynamic results and the static limit. Some minor errors in Nikitin and Tyurekhodgaev for the case of loading that is linear in time are corrected.

Step function Load

Consider first a step function load such that

$$E_f \frac{\partial u_f}{\partial z}\bigg|_{z=0} = E_f \varepsilon_0 \qquad \text{for } t > 0 \qquad . \tag{A.4}$$

Since a stress discontinuity is implied by a propagating step load, the front conditions given by Eqs. (A.1), (A.2), and (A.3a) are expected to apply. The solution to the wave equation, Eq. (2a), that satisfies these boundary conditions is

$$u_f = -\frac{\tau}{2RE_f}\left(z^2 - c_f^2 t^2\right) + \varepsilon_0\left(z - c_f t\right) \tag{A.5}$$

with $\eta = 1$ (front velocity $v_0 = c_f$) always. The particle velocity is thus

$$\frac{\partial u_f}{\partial t} = \frac{\tau}{RE_f}c_f^2 t - \varepsilon_0 c_f = c_f \frac{t}{t_r} \tag{A.6a}$$

where

$$t_r = \frac{E_f R}{\tau c_f} \tag{A.6b}$$

and is independent of z: within the sliding zone $0 < z < c_f t$, the fibre moves with uniform velocity. The particle acceleration is given by

$$\frac{\partial^2 u_f}{\partial t^2} = \frac{\tau}{RE_f}c_f^2 = \frac{c_f}{t_r} \tag{A.7}$$

which is uniform in time. Motion stops when

$$t = \varepsilon_0 t_r \qquad . \tag{A.8}$$

This is the characteristic time of the dynamic process for the case of a rigid matrix. At $t = \varepsilon_0 t_r$, the sliding zone has advanced a distance

$$l_r = c_f t_r \varepsilon_0 = \frac{E_f R}{\tau}\varepsilon_0 \qquad\qquad (t = \varepsilon_0 t_r) \tag{A.9}$$

The strain along the rod has the distribution

$$\frac{\partial u_f}{\partial z} = \varepsilon_0 - \frac{\tau}{RE_f} z \qquad . \qquad (A.10)$$

The load point displacement, u_0, (i.e., the displacement at $z = 0$) evolves in time according to

$$u_0 = -\varepsilon_0 c_f t \left[1 - \frac{1}{2\varepsilon_0} \frac{t}{t_r} \right] \qquad . \qquad (A.11)$$

When $t = \varepsilon_0 t_r$,

$$u_0 = -\frac{E_f R}{2\tau} \varepsilon_0^{\,2} \qquad (t = \varepsilon_0 t_r) \qquad (A.12)$$

which is exactly twice the displacement, $u_0^{(st)}$, developed under static loading (see below). The final slip length, l_r, is also twice the slip length for static loading; and the strain gradient, $\partial u_f / \partial z$, is half that developed under static loading.

One important consequence of the last fact is that when motion is arrested at $t = \varepsilon_0 t_r$, no further stress relaxation is required: the stress gradient at $t = \varepsilon_0 t_r$ is only half the maximum gradient that can be supported in the fibre by the friction tractions. According to the constitutive behaviour assumed for the friction phenomenon, Eq. (1c), the fibre will remain motionless. Therefore, the configuration predicted for $t = \varepsilon_0 t_r$ is the final configuration. Since Eq. (A.10) predicts that $\sigma_f(l_r) = 0$ at $t = \varepsilon_0 t_r$, the front condition will switch at this instant to Eq. (A.3b): the condition of Eq. (A.1) leads to an indeterminate front velocity.

When the fibre arrests at $t = \varepsilon_0 t_r$, the particle acceleration in the slip zone falls instantaneously to zero from the constant value of Eq. (A.7). At the same instant, the friction tractions along the slip zone fall from the uniform value, τ, which they had during the motion of the fibre, to $\tau/2$, the value required to sustain the stress gradient in the fibre at the time of arrest. This discontinuous change in the friction stress is a direct consequence of the constitutive behavior embodied in Eq. (1).

For the step load case, Eq. (A.5) yields the following energy analysis. The work done by the load at time $t < \varepsilon_0 t_r$ is given by

$$W_1 = \pi R^2 E_f \varepsilon_0 u_0 = \frac{\pi E_f^2 \varepsilon_0^3 R^3}{\tau} \left(\frac{t}{\varepsilon_0 t_r} \right) \left[1 - \frac{1}{2} \left(\frac{t}{\varepsilon_0 t_r} \right) \right] \qquad . \qquad (A.13)$$

The kinetic energy in the moving fibre at time t is given by

$$W_{\mathrm{k}} = \int_0^{c_{\mathrm{f}} t} \frac{\pi R^2 \rho_{\mathrm{f}}}{2} \left(\frac{\partial u_{\mathrm{f}}}{\partial t} \right)^2 dz = \frac{\pi E_{\mathrm{f}}^2 \varepsilon_0^3 R^3}{2\tau} \left(\frac{t}{\varepsilon_0 t_{\mathrm{r}}} \right) \left[\left(\frac{t}{\varepsilon_0 t_{\mathrm{r}}} \right) - 1 \right]^2 . \tag{A.14}$$

The strain energy in the fibre at time t is given by

$$W_{\mathrm{e}} = \int_0^{c_{\mathrm{f}} t} \frac{\pi R^2 E_{\mathrm{f}}}{2} \left(\frac{\partial u_{\mathrm{f}}}{\partial z} \right)^2 dz = \frac{\pi E_{\mathrm{f}}^2 \varepsilon_0^3 R^3}{2\tau} \left(\frac{t}{\varepsilon_0 t_{\mathrm{r}}} \right) \left[1 - \left(\frac{t}{\varepsilon_0 t_{\mathrm{r}}} \right) + \frac{1}{3} \left(\frac{t}{\varepsilon_0 t_{\mathrm{r}}} \right)^2 \right] . \tag{A.15}$$

These energy dissipated in friction up to time t is given by

$$W_{\mathrm{f}} = -\int_0^{c_{\mathrm{f}} t} 2\pi R \, \tau u \, dz = \frac{\pi E_{\mathrm{f}}^2 \varepsilon_0^3 R^3}{\tau} \left(\frac{t}{\varepsilon_0 t_{\mathrm{r}}} \right)^2 \left[1 - \frac{2}{3} \left(\frac{t}{\varepsilon_0 t_{\mathrm{r}}} \right) \right] . \tag{A.16}$$

The energy terms are plotted in Fig. A.1. The total work done at time $t = \varepsilon_0 t_{\mathrm{r}}$ is exactly three times that done in static loading to $\varepsilon_0 E_{\mathrm{f}}$ (see below).

Linearly Increasing Load

Consider next the case of an applied strain that is given by the linear law

$$\sigma_{\mathrm{f}}(0) = E_{\mathrm{f}} \left. \frac{\partial u_{\mathrm{f}}}{\partial z} \right|_{z=0} = E_{\mathrm{f}} k t \qquad (t > 0) . \tag{A.17}$$

In this case, a physically meaningful solution is found only for the front condition given by $\Delta\sigma_{\mathrm{f}} = 0$ and Eq. (A.3b). With these boundary conditions, Eq. (2a) has the solution

$$\begin{aligned} u_{\mathrm{f}}(z,t) &= -\frac{\tau z^2}{2RE_{\mathrm{f}}} \left[\sqrt{1 + (kt_{\mathrm{r}})^2} + 1 \right] - \frac{\tau c_{\mathrm{f}}^2 t^2}{2RE_{\mathrm{f}}} \left[\sqrt{1 + (kt_{\mathrm{r}})^2} - 1 \right] + ktz \\ &= -\frac{\tau}{RE_{\mathrm{f}}} \frac{1}{1-\eta^2} (z - \eta c_{\mathrm{f}} t)^2 \end{aligned}$$

$$(z \leq \eta c_{\mathrm{f}} t) \tag{A.18}$$

with

$$\eta = k t_{\mathrm{r}} \Big/ \left[\sqrt{1 + (kt_{\mathrm{r}})^2} + 1 \right] \tag{A.19}$$

where t_{r} is the characteristic time of Eq. (A.8). Thus the particle velocity is given by

$$\frac{\partial u_f}{\partial t} = -\frac{\pi c_f^2 t}{RE_f}\left[\sqrt{1+(kt_r)^2}-1\right]+kz \qquad (z \le \eta c_f t) \qquad \text{(A.20)}$$

the acceleration by

$$\frac{\partial^2 u_f}{\partial t^2} = -\frac{\pi c_f^2}{RE_f}\left[\sqrt{1+(kt_r)^2}-1\right] \qquad (z \le \eta c_f t) \qquad \text{(A.21)}$$

the stress distribution by

$$\sigma_f = kE_f t -\frac{\tau z}{R}\left[\sqrt{1+(kt_r)^2}+1\right] \qquad (z \le \eta c_f t) \qquad \text{(A.22)}$$

and the load point displacement by

$$u_0 = -\frac{\pi c_f^2 t^2}{2RE_f}\left[\sqrt{1+(kt_r)^2}-1\right] \qquad (t > 0) \qquad . \qquad \text{(A.23)}$$

The static limit in this case can be found by taking the limit $k \to 0$. One finds

$$\eta c_f t \to \frac{E_f Rkt}{2\tau} = \frac{\sigma_f(0,t)R}{2\tau} = l_r^{(st)} \qquad (k \to 0) \qquad \text{(A.24a)}$$

$$\frac{\partial u_f}{\partial t} \to k\left[z - \frac{\sigma_f(0,t)}{\tau}R\right] \to 0 \qquad (k \to 0) \qquad \text{(A.24b)}$$

$$\sigma_f \to \sigma_f(0,t)\left[1 - \frac{2\tau}{\sigma_f(0,t)}\frac{z}{R}\right] = \sigma_f^{(st)} \qquad (k \to 0) \qquad \text{(A.24c)}$$

$$u_0 \to \frac{E_f R}{4\tau}(kt)^2 = \frac{[\sigma_z(0,t)]^2 R}{4E_f \tau} = u_0^{(st)} \qquad (k \to 0) \qquad \text{(A.24d)}$$

where the superscript "(st)" indicates the result obtained by static analysis for loading to the instantaneous value, $\sigma_z(0,t)$, of the applied tractions (see below). In the static limit, Eq. (A.24b) also shows that $\eta \to 0$ (consistently with Eq. (A.24a)); while in the limit of very rapid loading ($k \to \infty$), or vanishing friction ($\tau \to 0$), Eq. (A.24b) leads to $\eta \to 1$, i.e., the front reverts to propagating at the bar wave velocity.

Equations (A.23) and (A.24d) allow the dynamic load point displacement to be related very simply to the displacement expected for static loading to the same instantaneous applied load:

$$\frac{u_0}{u_0^{(st)}} = 2\left[\frac{\sqrt{1+(kt_r)^2}-1}{(kt_r)^2}\right] \qquad . \tag{A.25}$$

The same characteristic time, t_r, identifies cases where dynamic effects are important in both the step and linear loading cases.

The Static Problem

Under static loading to stress $\sigma_0 = E_f\varepsilon_0$, force equilibrium leads to a linear stress gradient along the fibre

$$\sigma_f^{(st)} = \sigma_0\left[1 - \frac{2\tau z}{\sigma_0 R}\right] \tag{A.26}$$

so that the slip length, where $\sigma_f^{(st)} = 0$, is given by

$$l_r^{(st)} = \frac{E_f R}{2\tau}\varepsilon_0 \qquad . \tag{A.27}$$

The load point displacement can be found by integrating the strain along the fibre and is given by

$$u_0^{(st)} = -\frac{E_f R}{4\tau}\varepsilon_0^2 \qquad . \tag{A.28}$$

The total work done by the load in the static problem is given by

$$W_1^{(st)} = \int_0^{u_0^{(st)}} \pi R^2 \sigma du = \frac{\pi E_f^2 \varepsilon_0^3 R^3}{6\tau} \tag{A.29}$$

where here u and σ denote the displacement and stress at $z = 0$ during loading.

Appendix B. The Wedge-Loaded DCB Specimen with Large Scale Bridging.

In a specimen in which shear deformation may be neglected (material anisotropy not too large) and in which a linear bridging law, $p = \beta_3 u$, acts on the bridged part of the crack (Fig. 7), analytical expressions can be found for the characteristics of crack propagation (Massabò and Cox, 2000). The crack displacement profile is given by

$$u = e^{bx}\left(c_1 \cos bx + c_2 \sin bx\right) + e^{-bx}\left(c_3 \cos bx + c_4 \sin bx\right) \tag{B.1}$$

where

$$b = \left[\frac{\beta_3}{4E_x' I_d}\right]^{1/4} \quad . \tag{B.2}$$

and $I_d = h^3/12$, $E_x' = E_x/(1 - \nu_{yx}\nu_{xy})$, and E_x and ν_{yx} and ν_{xy} are Young's modulus and Poisson's ratios for the laminate, respectively. The constants c_i are determined by boundary conditions. At the crack tip, $u = 0$ and the bending rotation $\phi = -\,du/dx = 0$ (shear deformation neglected); while at the notch root, $x = 0$, one can write generally that $u = \hat{u}_0$ and $\phi = \hat{\phi}_0$.   Observing that the bending moment, $\hat{M} = M(x = 0)$, and shear force, $\hat{Q} = Q(x = 0)$, at $x = 0$ are related by

$$\frac{\hat{M}}{\hat{Q}} = -\frac{Pl}{P} = -l \tag{B.3}$$

where P is the load applied by the wedge and, for a beam with negligible shear deformation, $Q = -(E_x' I_d)d^3 u/dx^3$ and $M = -(E_x' I_d)d^2 u/dx^2$, one finds by solving for the coefficients c_I in (B.1) that

$$\hat{\phi}_0 = \frac{-b\hat{u}_0\left[e^{-\pi} + 1 + 2lb\left(e^{-\pi} - 1\right)\right]}{e^{-\pi} - 1 + lb\left(e^{-\pi} + 1\right)} \tag{B.4}$$

and thence

$$\hat{M} = -2\hat{u}_0 \frac{lb^3 E_x' I_d\left(e^{-\pi} + 1\right)}{e^{-\pi} - 1 + lb\left(e^{-\pi} + 1\right)} \quad . \tag{B.5}$$

If the loading arm length, l, is not short, then the deflection at the point of contact with the flying wedge, δ, will be much greater than u_0 and therefore δ can be estimated as the deflection expected for a cantilever beam with built-in end condition at $x = 0$:

$$\delta = -\frac{\hat{M}l^2}{3E'_x I_d} \tag{B.6}$$

and thus

$$\delta = \frac{2}{3}\hat{u}_0 l^2 b^2 \frac{e^{-\pi}+1}{e^{-\pi}+1+(lb)^{-1}(e^{-\pi}-1)} \quad . \tag{B.7}$$

In the limit that lb is large,

$$\delta \approx \frac{2}{\sqrt{3}}\left[\frac{\beta_3 l^4}{E'_x h^3}\right]^{1/2} \hat{u}_0 \quad . \tag{B.8}$$

Figure Captions

1. (a) Schematic of a crack bridged by fibres, showing process zone where relative displacement exists between fibres and matrix. (b) Idealisation of the bridged crack problem with process zone replaced by surface tractions acting on the fracture surfaces.

2. Schematic of the dynamic pullout problem in a representative volume near the fracture plane.

3. The product $2\alpha\beta\eta$, which indicates the relative importance of inertial effects in the bridging phenomenon. (a) Numerical results for representative values of β. (b) Numerical results for $2\alpha\beta\eta$ compared with asymptotic limit for large E_m (dashed curves). The value of $(\alpha\beta)_1$ is marked for $\beta = 0.01$ and is to be compared with the value of $\alpha\beta$ at which $2\alpha\beta\eta \approx 0.9$, which is taken as a representative cutoff for significant inertial effects.

4. Fibre pullout from a rigid matrix.

5. The ratio of dynamic and static load point displacements for a fibre pulled out of a rigid matrix by a load that rises linearly with time.

6. A matrix crack propagating in the ACK limit.

7. A double cantilever beam specimen loaded by a flying wedge.

A.1 The distribution of energy as a function of time for a fibre pulled out of a rigid matrix by a step load.

(a)

(b)

Figure 1

Figure 2

(a)
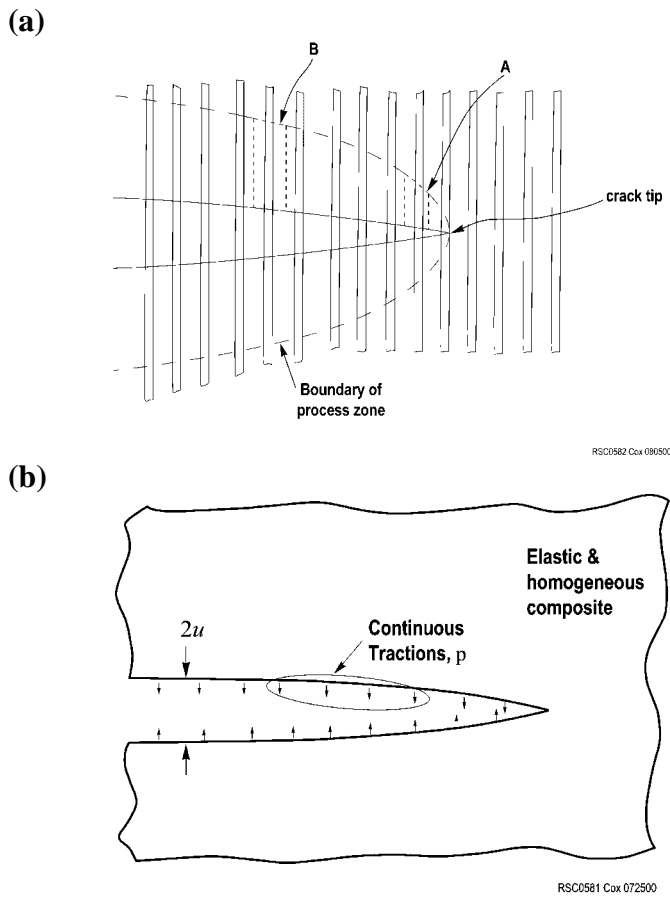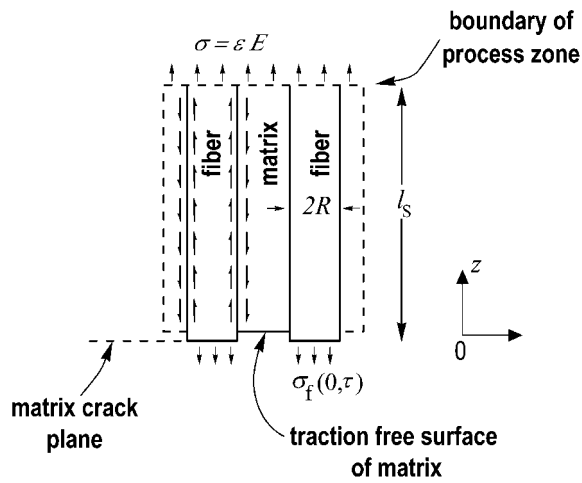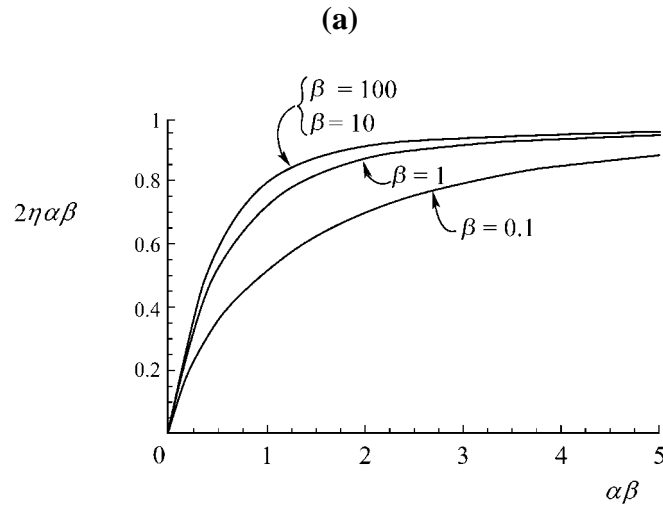
RSC0583 Cox 080500

(b)
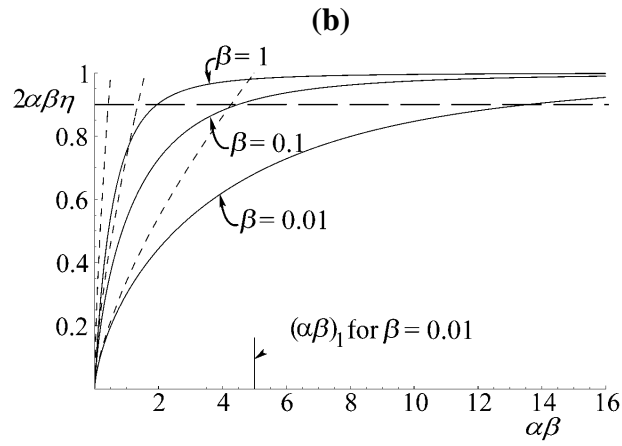
RSC0600.COX.0607.00

Figure 3
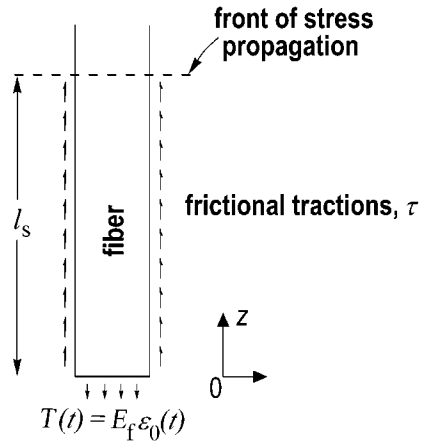
RSC0585 Cox 080500

Figure 4.
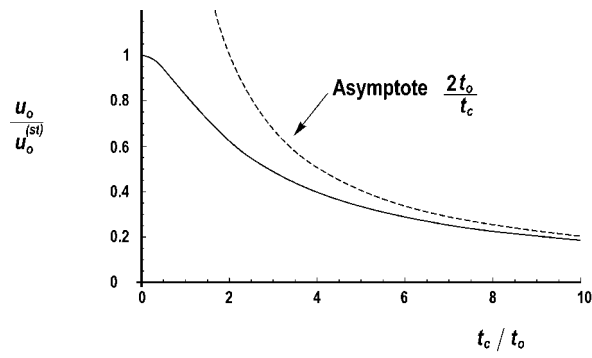
RSC0573 Cox 061600

Figure 5.
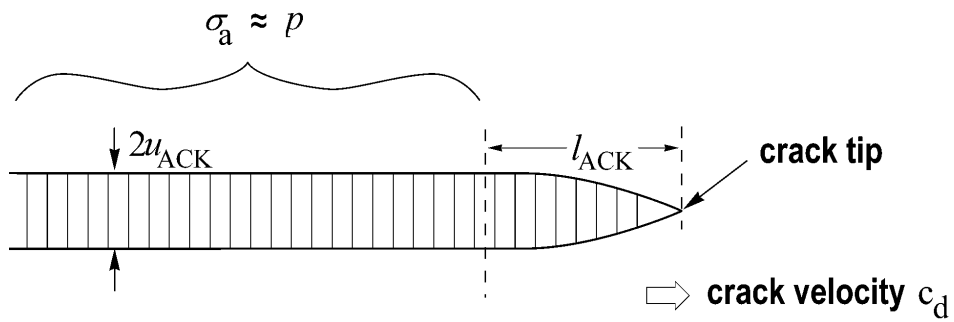
RSC0584 Cox 080500

Figure 6.
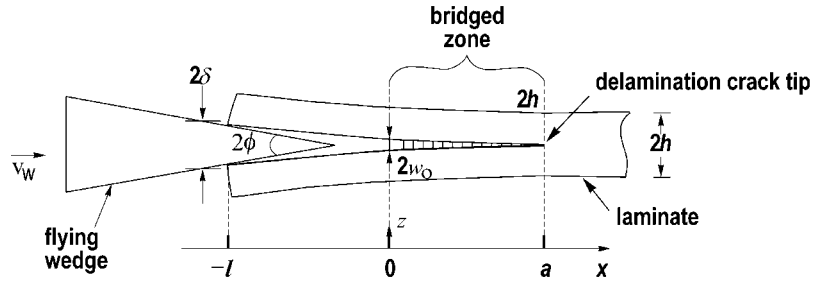
RSC0571 Cox 072500

Figure 7.
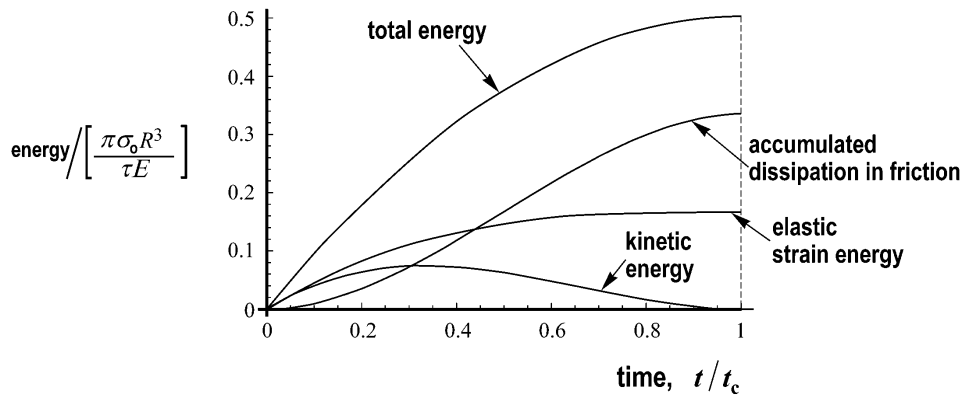
RSC0574 Cox 080500

Figure A.1

Rockwell
Science Center

Simple form for the Dynamic *G* – *K* relationship in Orthotropic Materials

N. Sridhar and B. N. Cox

Rockwell Science Center
1049 Camino Dos Rios
Thousand Oaks, CA 91360
U.S.A.

and

I. J. Beyerlein

Los Alamos National Laboratory
Los Alamos, New Mexico
U.S.A.

1. Introduction

This note presents explicit relations between the dynamic crack energy release rate and crack tip stress intensity factors in a form most amenable to computational work for a crack propagating along any principal axis in an orthotropic material. The results presented in this form may be particularly useful for work on delamination cracks in laminated composites, which are orthotropic in many important applications.

Prior work in the literature that treats the problem of interest here include the analysis of a mode I crack in an orthotropic medium by Piva and Viola (1988); and the analysis of a mixed mode crack in a transversely isotropic medium by Wu (1989). Yang and co-workers (1991) presented results for a mixed mode crack in an orthotropic material, but in a form that is not best suited for immediate computation. By an adaptation of the Stroh method of analysis used by Wu, the results of Yang et al. are rendered here in a different form better suited to numerical evaluation. The role of orthotropic anisotropy in determining the velocity dependence of G_d is then illustrated for delamination cracks in typical ceramic, metal and polymer matrix laminated composites.

2. Results

The relation between the energy release rate and the crack tip stress intensity factor is central to fracture analysis. It appears, for example, in the derivation of stress intensity factors from applications of the *J*-integral and in the derivation via energy arguments of integral equations for bridged cracks from weight functions. Details of the latter for dynamic cracks with large scale bridging in the crack wake will appear elsewhere.

Freund (1972) showed that the dynamic crack energy release rate for an extending crack in an elastic body can be written as the modified J-integral, which leads to the *G-k* relationship in the following, convenient form:

$$G_d = \frac{1}{2} k^D(t)^T L^{-1} k(t) \tag{1}$$

where G_d is the dynamic crack energy release rate and k(t) is the instantaneous crack tip stress intensity factors (see Eq. 4.19 in Wu and references therein). The elements of the

L^{-1} matrix are universal functions, in the sense that they are independent of the details of the applied loading or on the configuration of the body being analyzed. We present results for the L^{-1} matrix when the material possesses orthotropic symmetry and when the crack is extending along one of the principal axis. In this case, the off-diagonal elements of the matrix are zero and the diagonal elements of the L^{-1} matrix is just dependent on the elastic properties of the orthotropic medium and the instantaneous value of the crack tip velocity. For an orthotropic material with the crack propagating along the 1 direction (and direction 3 being the plane strain direction), elements of the L^{-1} matrix are:

$$L^{-1} = \frac{1}{C_{66}} \begin{pmatrix} \dfrac{-(\gamma_5 + \gamma_1\gamma_4)}{(\gamma_4^2 - \gamma_3\gamma_5)} & 0 & 0 \\ 0 & \dfrac{-(\gamma_3 - \gamma_2\gamma_4)}{(\gamma_4^2 - \gamma_3\gamma_5)} & 0 \\ 0 & 0 & \dfrac{1}{\gamma_6} \end{pmatrix} \tag{2}$$

where the γ's are

$$\gamma_1 = \frac{C_{66} - \beta_2^2 C_{22} - \rho v^2}{\beta_2(C_{12} + C_{66})} \qquad \gamma_2 = \frac{C_{11} - \beta_1^2 C_{66} - \rho v^2}{\beta_1(C_{12} + C_{66})} \qquad \gamma_3 = \frac{C_{11} + \beta_1^2 C_{12} - \rho v^2}{\beta_1(C_{12} + C_{66})}$$

$$\gamma_4 = \frac{C_{12} + \beta_2^2 C_{22} + \rho v^2}{(C_{12} + C_{66})} \qquad \gamma_5 = \frac{C_{12} + \beta_2^2 C_{22} - \dfrac{C_{12}}{C_{66}}\rho v^2}{\beta_2(C_{12} + C_{66})} \qquad \gamma_6 = \frac{C_{44}}{C_{66}}\beta_3$$

$$\tag{3}$$

where C_{ij} are coefficients of the stiffness matrix, ρ is the density of the medium and v is the instantaneous velocity of the crack tip. The expressions for β are:

$$\beta_1 = \sqrt{\frac{r_1 + \sqrt{r_1^2 - r_2}}{2\,C_{22}\,C_{66}}} \qquad \beta_2 = \sqrt{\frac{r_1 - \sqrt{r_1^2 - r_2}}{2\,C_{22}\,C_{66}}} \qquad \beta_3 = \sqrt{\frac{C_{55} - \rho v^2}{C_{44}}}$$

$$\tag{4}$$

where

$$r_1 = C_{11}C_{22} - C_{12}^2 - 2C_{12}C_{66} - (C_{22} + C_{66})\rho v^2$$
and
$$r_2 = 4C_{22}C_{66}(C_{11} - \rho v^2)(C_{66} - \rho v^2) \quad .$$

The $L^{-1}_{3,3}$ matrix elemenet is

$$L^{-1}_{3,3} = \frac{1}{C_{44}\sqrt{\dfrac{C_{55}}{C_{44}} - \dfrac{\rho v^2}{C_{44}}}}$$

(5)

We can also define the generalized Rayleigh wave function R(v) as

$$R(v) = \gamma_4^2 - \gamma_3\gamma_5$$

(6)

and the Rayleigh wave speed (v_r) is obtained by setting $R(v_r) = 0$.

In the next section, the diagonal elements $L^{-1}_{1,1}$ and $L^{-1}_{2,2}$ are plotted numerically for cracks propagating along different principal axes in various representative composites. The L^{-1} matrix elements are functions of the elastic properties and the instantaneous crack velocity. Each diagonal element approaches the corresponding static value as $v \to 0$ and has the property of $O[(v_r - v)^{-1}]$ as $v \to v_r$, where v_r is the Rayleigh wave speed.

3. Discussion

In this section, we will present results for the the mode I and mode II contributions to the crack energy release rate, as represented by the $L^{-1}_{1,1}$ and $L^{-1}_{2,2}$ matrix elements, for various representative composites that possess orthotropic symmetry and where the crack is extending along one of the principal axis. These results are presented graphically as a function of the orthotropy parameters and the instantaneous crack tip velocity. The mode III contribution to the crack energy release rate is a simple expression (see Eq. 5) and hence will not be examined further.

In the results presented below, the orientation is such that the principal axes of orthotropic symmetry are aligned with the coordinate axis, the crack lies in the 1-3 plane and the crack is propagating along the 1 direction (with direction 3 being the plane strain direction). Table I shows the stiffness tensor for various representative composites, the corresponding orthotropy paramaters and the Rayleigh velocity (v_r) normalized by the shear wave velocity (v_s). Also examined in Table I are cases where the crack is running along the different principal directions of orthotropic symmetry. The orthotropy parameters λ and ρ as presented by Suo, et al. (1991) are:

$$\lambda = \frac{b_{11}}{b_{22}} \quad \text{and} \quad \rho = \frac{b_{12} + \frac{1}{2} b_{66}}{\sqrt{b_{11} b_{66}}} \quad \text{where}$$

$$b_{ij} = \begin{cases} S_{ij} \ (plane\ stress) \\ S_{ij} - \dfrac{S_{i3} S_{j3}}{S_{33}} \ (plane\ strain) \end{cases}$$

and where S_{ij} are the elements of the compliance tensor.

Figure 1 shows the variation of the normalized $L^{-1}_{1,1} / [L^{-1}_{1,1}]_{static}$, where $[L^{-1}_{1,1}]_{static}$ is the value of $L^{-1}_{1,1}$ when $v \to 0$, as a function of the normalized crack velocity v/v_r, where v_r is the Rayleigh wave speed. This variation is shown for the different cases listed in Table I. However, it is clear from the figure that the variation in the crack energy release rate can be rationalized in terms of the orthotropy parameters λ and ρ. For the same normalized crack speed, the normalized mode I contribution ($L^{-1}_{1,1} / [L^{-1}_{1,1}]_{static}$) to the dynamic crack energy release rate increases as λ monotonically increases and as ρ monotonically decreases.

Figure 2 similarly shows the variation of the normalized $L^{-1}_{2,2} / [L^{-1}_{2,2}]_{static}$, where $[L^{-1}_{2,2}]_{static}$ is the value of $L^{-1}_{2,2}$ when $v \to 0$, as a function of the normalized crack velocity v/v_r, where v_r is the Rayleigh wave speed. This variation is shown for the different cases listed in Table I. As in the mode I case, the variation in the crack energy release rate can be rationalized in terms of the orthotropy parameters λ and ρ. For the same normalized crack speed, the normalized mode II contribution ($L^{-1}_{2,2} / [L^{-1}_{2,2}]_{static}$) to the dynamic crack energy release rate increases as λ increases and as ρ decreases. However, as opposed to the mode I case, the variation on λ and ρ is much smaller. In addition, we observe that

although the energy release rate shows a monotonic dependence on λ, the dependence on ρ, for small ρ, is not monotonic.

4. Conclusions

An analytical form for easy estimation of the dynamic crack energy release rate, in terms of the crack tip stress intensity factors, has been presented for cracks propagating along any of the principal axis in orthotropic material systems. The dynamic crack energy release rate depends on the magnitude of the two orthotropic parameters and the instantaneous crack tip velocity. The dynamic crack energy release rate is $O[(v_r - v)^{-1}]$ as $v \rightarrow v_r$, and where v_r is the Rayleigh wave speed. The variation in the dynamic crack energy relase rate for orthotropic materials can be rationalized in terms of the two orthotropy parameters λ and ρ.

References

Piva, A., and Viola, E., 1988, "Crack Propagation in an Orthotropic Medium", *Engineering Fracture Mechanics*, vol.29, 535-548

Freund, L.B., 1972, "Energy flux into the tip of an extending crack in an elastic solid", *Journal of Elasticity*, vol. 2, 341-349

Wu, K.-C., 1989, "On the crack tip fields of a dynamically propagating crack in an anisotropic solid", *Intl. Journal of Fracture*, vol. 41, 253-266

Yang, W., Suo, Z., and Shih, C.F., 1991, "Mechanics of dynamic debonding", *Proc. R. Soc. Lond. A*, vol. 433, 679-697

Suo, Z., Bao, G., Fan, B., and Wang,T.C., 1991, "Orthotropy Rescaling and Implications for Fracture in Composites", *Int. J. Solids. Structures*, vol.28, 235-248

<u>Figure Caption</u>

Figure 1: The variation of $L^{-1}_{1,1}$ (Fig.1a) and $L^{-1}_{2,2}$ (Fig.1b) normalized by their corresponding static values as a function of the crack tip velocity, normalized by the Rayleigh wave velocity, is shown for different values of λ and ρ.

Table I

		C11 GPa	C22 GPa	C33 GPa	C44 GPa	C55 GPa	C66 GPa	C12 GPa	C13 GPa	C23 GPa	λ	ρ	v_r/v_s
Carbon/Epoxy Unidirectional composite	**1a**	150	12	12	5	30	30	5	5	5	0.08	0.58	0.838
	1b	12	150	12	30	5	30	5	5	5	12.5	0.58	0.593
	1c	12	12	150	30	30	5	5	5	5	1.0	0.58	0.864
Carbon/Epoxy $0^0/90^0$	**2a**	10	90	90	10	10	10	5	5	30	9.0	1.29	0.854
	2b	90	10	90	10	10	10	5	30	5	0.11	1.29	0.946
Carbon/Epoxy Quasi-isotropic	**3a**	10	60	60	10	30	30	5	5	20	6.0	0.19	0.512
	3b	60	10	60	30	10	30	5	20	5	0.17	0.19	0.695
C-SiC ceramic matrix composite	**4a**	20	120	120	23	9	9	8	8	20	6.0	2.49	0.971
	4b	120	20	120	9	23	9	8	20	8	0.17	2.49	0.982
Representative Isotropic Comp.	**5**	80	80	80	30	30	30	20	20	20	1.00	1.00	0.911
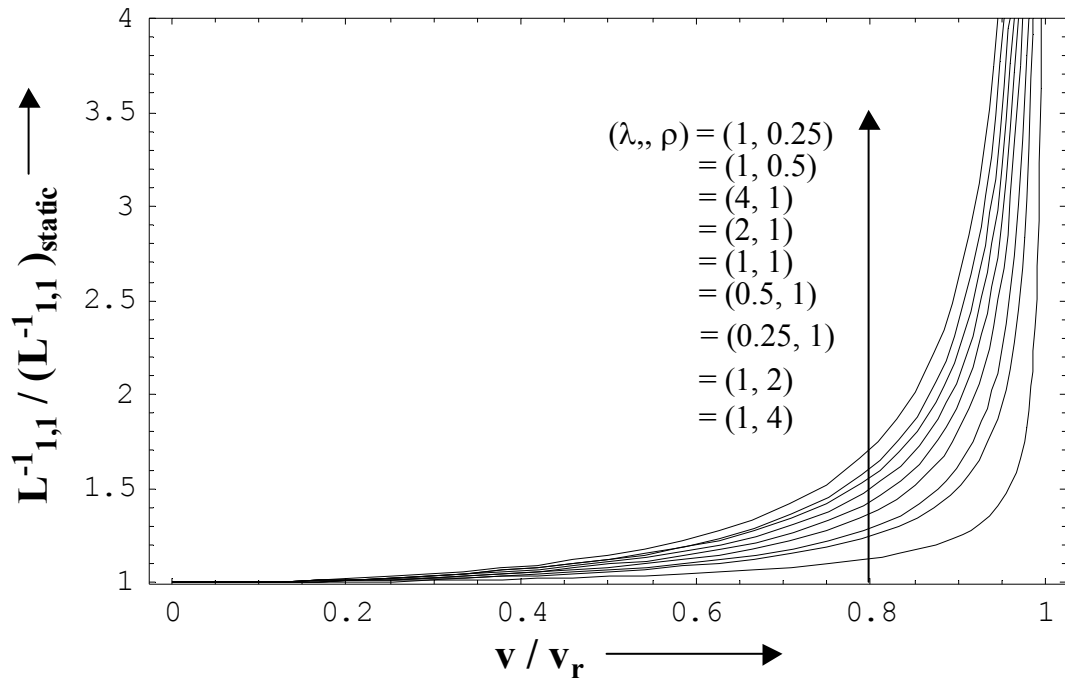
Figure 1: The variation of $L^{-1}_{1,1}$ normalized by the corresponding static value as a function of the crack tip velocity, normalized by the Rayleigh wave velocity, is shown for different values of λ and ρ.
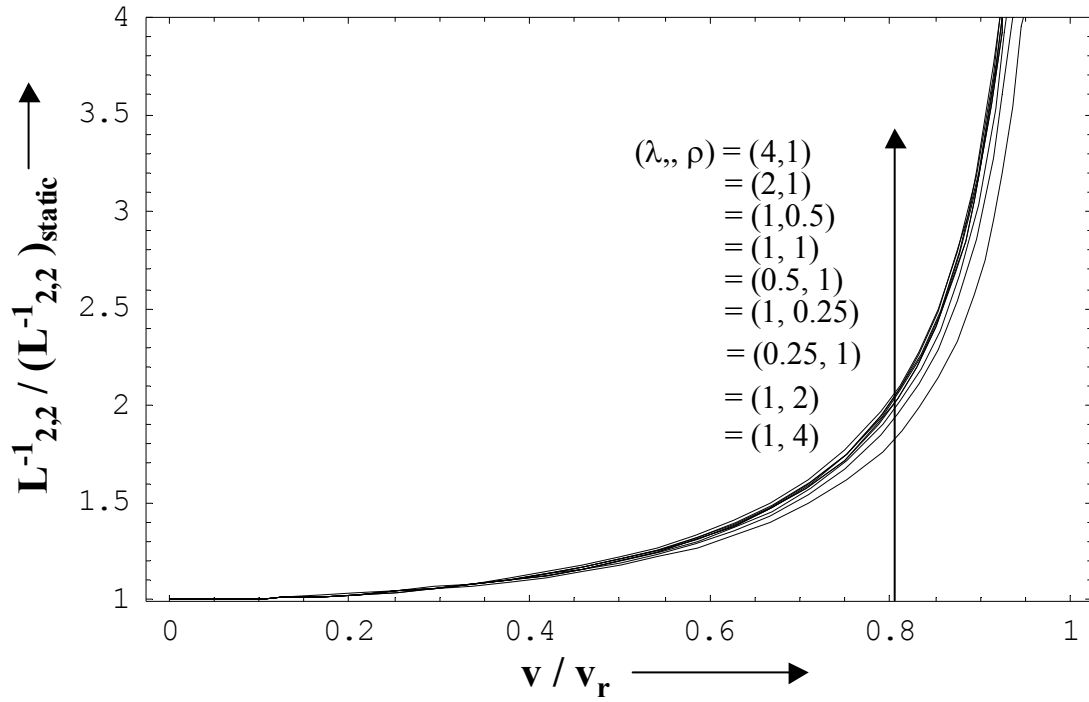
Figure 2: The variation of $L^{-1}_{2,2}$ normalized by the corresponding static value as a function of the crack tip velocity, normalized by the Rayleigh wave velocity, is shown for different values of λ and ρ.

The Physics of Dynamic Fiber Push-In Opposed by Friction

A. Rosakis
Department of Aeronautics
California Institute of Technology
Pasadena, CA
U.S.A.

Q. D. Yang, B. N. Cox and N.Sridhar
Rockwell Scientific
1049 Camino Dos Rios
Thousand Oaks, CA
U.S.A.

Abstract

Inertial effects in the mechanism of fibre pullout (or push-in) are examined, with emphasis on how the rate of propagation of stress waves along the fibre, and thence the pullout dynamics, are governed by friction and the propagation of companion waves excited in the matrix. Basic experiments have already been perfomed and the key strain field and velocity data successfully recorded. Dynamic photoelasticity was used to reveal the nature of the stress fields associated with the dynamic sliding process. A fundamental model has been proposed and numerically solved to gain a good understanding of the friction mediated push-in process.

1.0   INTRODUCTION

The mechanics of pullout have been much studied and are well understood for static loading. Simple analytical forms are available for $p(\delta)$, the relationship between the pullout load, p, and the displacement, δ, of the fibre's end, when the frictional coupling of the reinforcement to the matrix is uniform and slip extends over distances that are large compared to the reinforcement diameter (Marshall et al.,1985; McCartney, 1989; Hutchinson and Jensen, 1990). In this limit, which is a common case in ceramic composites and textile polymeric composites, the shear lag model of load transfer between the reinforcement and the matrix is accurate.

The success of shear lag models in matching numerical calculations and experiments for static pullout, given appropriate restrictions, encourages the viewpoint that similarly simple models might reveal some key aspects of pullout under dynamic loads. Prior work on the problem of a dynamically loaded rod subject to uniform friction has revealed some interesting characteristics of the effect of friction on the propagation of stress waves (Nikitin and Tyurekhhodgaev, 1990). For end-loading that rises continuously from zero, the stress front propagates at velocities less than the bar wave speed by a factor that depends on the loading rate. Only for step loading does the front propagate at the bar wave speed. This strong effect of friction results in significant stiffening of the response of the bar, measured as its end displacement for a given load, relative to the static loading case. On the other hand, when motion ceases following step loading, the net fibre displacement is exactly twice that expected for static loading to the same load – in this

case, dynamic effects lead to effective softening of the response (Nikitin and Tyurekhhodgaev, 1990). The front configuration and front speed for this simple bar problem can be explained by considering energy conservation and kinetic constraints at the front.

When the fibres are embedded in an elastic matrix, the problem is complicated by the interaction between the stress waves in the fibre and those excited in the matrix. The front conditions must then be expected to exhibit new characteristics and consequently the load-displacement relationship for the fibre end must be affected. The role of the matrix in dynamic pullout is the topic of this paper.

In a previous study (Cox, et al. 2001 and Sridhar, et al. 2001) a shear lag model that was directly analogous to that used successfully in static pullout problems (Hutchinson and Jensen, 1990) was extended to high loading rates with loading boundary conditions that were appropriate to the context of a bridged crack: the load was specified as a far-field condition within the body of the fibre/matrix system, rather than at the fibre end. Here new solutions are derived using a shear lag formulation with conditions appropriate to fibre pullout: the load is specified as a condition on the fibre end, with the far-field being stress-free. This configuration, as well as being interesting as a theoretical study, is representative of laboratory experiments that might be used to study frictional effects during pullout (Rosakis and Owen, 2002). Some interesting new characteristics of stress wave propagation are discovered for the particular case of a load that increases linearly in

time.　The frictional pullout process is modeled by finite element calculations of a fibre/matrix system in which friction is represented as a cohesive zone**.**

2.　　Model Description

The numerical model (Figure 1) was scaled to 1/80 of the experimental model through proper normalization. The normalization procedure is given in Appendix 1. In addition, only half of the experimental specimen was modeled owing to its symmetry. Symmetry boundary conditions ($U_3 = 0$; $\tau_{12} = 0$) were imposed along the center of the homolite piece and the top surface of the steel piece. Infinite elements were used to prevent elastic waves bouncing back from the right end.

Cohesive zone model was used to mimic the frictional interface between the homolite and steel piece (need a more detailed description of the CZM). Constant friction stress was assumed (despite the fact that a linear zone has to be introduced for the sake of numerical stability)

A dynamic loading history was imposed on the left end of the homolite piece. The loading history is obtained from CalTech's experimental measurement, which is shown in Figure 2. The interfacial frictional stress used was 40 MPa.
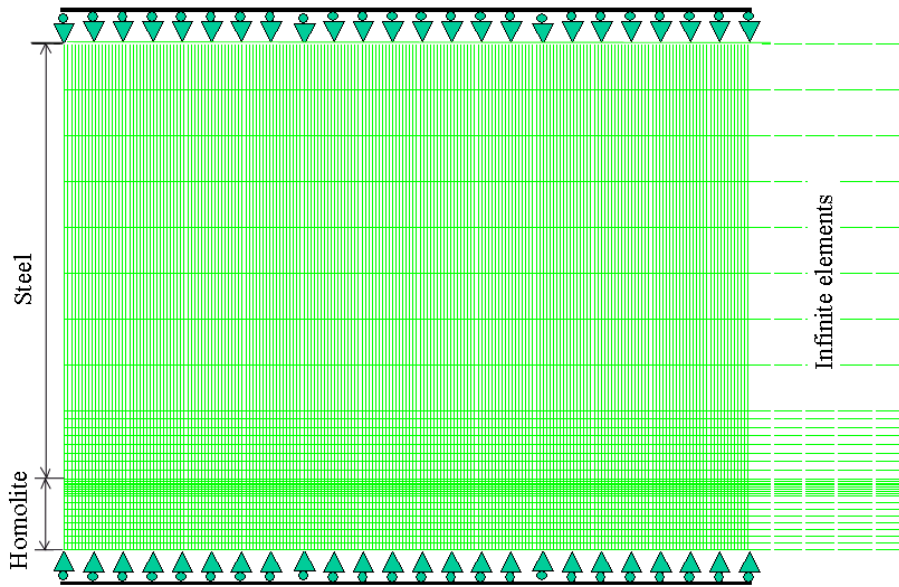
Figure 1   Numerical Model
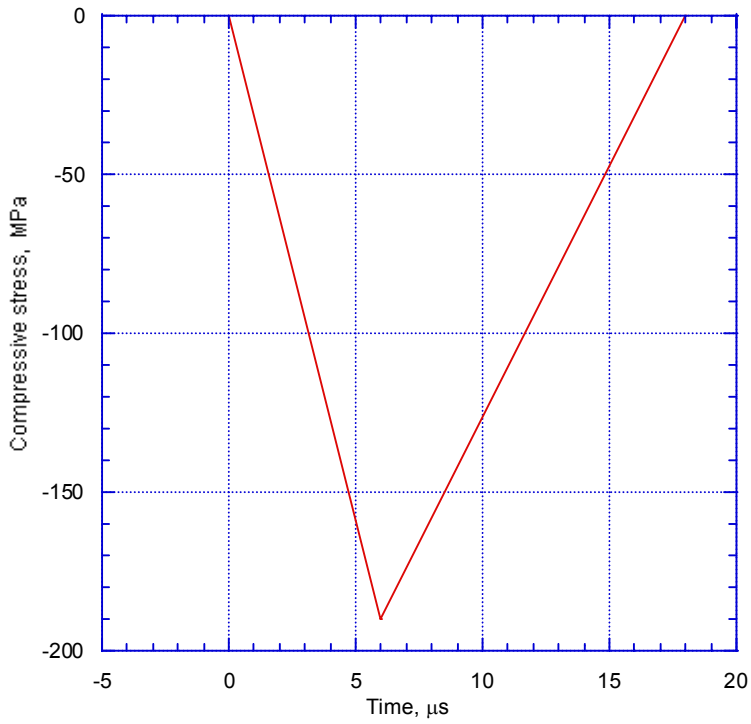
Figure 2   Loading history: Loading rate =31.5 MPa/µs, rising time 6.0 µs, total time 18.0 µs.

3.   Results

3.1   Characteristic Zones

Figure 3 show the contour plots of $(\sigma_1\text{-}\sigma_2)$ and τ_{12} in the homolite at an instant of $t =$ 9.822 μs. It is seen that there are three distinct zones associated with the wave propagation in the homolite. To the right most is the so-called head wave zone. This is the stick zone characterized by shear lag analysis, where the interface friction stress has an opposite sense compared to that in the zones following it. In this zone, the homolite is loaded by the steel piece and, the wave front travels at a speed larger than the wave speed of homolite (C_f), but smaller than that of the steel (C_m).

Following the head wave zone is the linearly increasing shear stress zone. In this region, the interface friction stress gets increasingly large before it reaches the constant value given by the cohesive law. The existence of this zone is caused by the finite-sloped transition from negative to positive shear stress used in the CZ model. However, zones of this feature were indeed observed in experiments (Fig 7 in CalTech's report). The interface friction stress causes the kinks in the contours of $(\sigma_1\text{-}\sigma_2)$ that form in angled bands, which is confirmed by experimental observations.

Immediately behind the linear friction zone is the constant friction zone, which is characterized by a sudden drop in contour density in the $(\sigma_1\text{-}\sigma_2)$ contour plot. This region is characterized as "slip zone" in shear-lag analysis, where the relative particle velocity in the steel and homolite (at interface) exceeds the critical value for transition in CZ law. According to shear lag analysis, the wave front of this zone travels at a speed smaller than C_f.

Behind the constant friction zone is a zone associated with the unloading part of the loading history. The contour lines in this region near the interface are quite chaotic, which is also seen in the experiments. This may be related to the local instabilities excited

by the unloading wave. Actually, in the numerical simulation, alternating contacting and separation zones exist in this region. Interestingly, experimentally obtained $(\sigma_1 - \sigma_2)$ fringes also showed this chaotic phenomena.
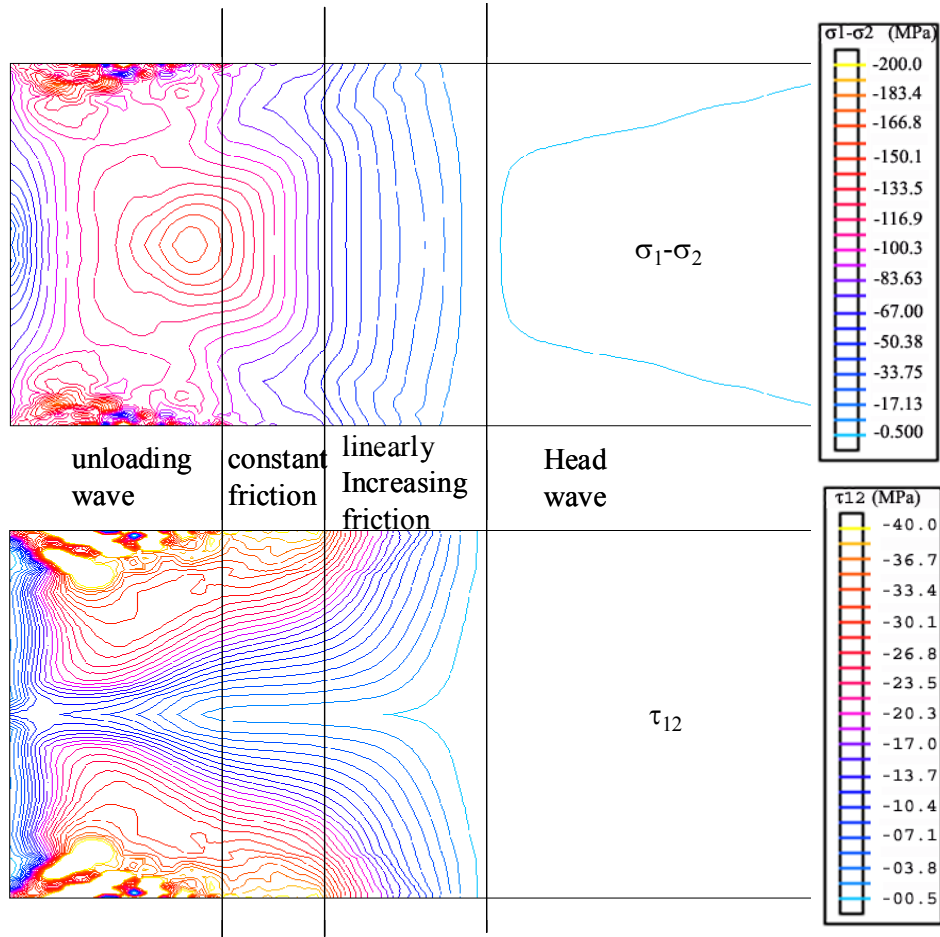

Figure 3   Contour plots of $(\sigma_1 - \sigma_2)$ and τ_{12} in the homolite at $t = 9.822$ μs

3.2 Stress profiles and wave velocities

Figure 4 shows the stress profiles in homolite at three different instants. Plotted in Figure 4(a) are the axial stress profiles along the center line of the homolite. The wave velocity calculated from this plot is $V \approx C_f$ (0.995 C_f), which agrees very well with elasto-dynamics, and also agrees well with experimental measurement. However, note that for each curve, there is a change of slope at some distance behind the wave front. The slope

of these curves, according to elastodynamics, is $-\dot{\sigma}_0/V$ (because $\sigma_{11}(x)=\dot{\sigma}_0(t-x/V)$).
Since the velocity V is constant, it follows that it is the loading rate that is decreasing
with time. Also note that the peak load that is experienced at the centerline seems also
dropping as the wave propagates. This is attributed to the dissipative frictional sliding
process along the interface.

Figure 4(b) shows the interface shear stress at the three instants. The shear stress
increases near linearly until the constant friction stress assigned in the CZ law is reached.
It shows an almost linearly increasing region followed by a constant shear stress region
(with very small fluctuations around the assigned value). The wave velocity indicated by
the interface τ_{12} curves is $V_{int} = 0.87\ C_f$, which is markedly smaller than the wave
velocity along the center (Shear lag prediction for this case is $0.68\ C_f$). The constant
shear stress region is followed by a region marked by the high frequency, violent
fluctuations. This indicates that unloading wave begins.

Figure 4(c) shows the axial stress at interface as a function of location. The wave velocity
is $0.87\ C_f$, which is consistent with that measured from the interface shear stress wave.
However, there is a region immediately after the wave front where the loading rate is
very small, marked by the very small slope.

The high-frequency oscillation associated with the unloading wave seems not related to
numerically-induced oscillations like the Gibbs phenomenon, because the oscillation only
happens at interface (Fig. 4b & c), while the axial stress measured at the center line of
homolite is very smooth (Fig. 4a). This may be explained by some sort of local instability
mechanism.

Since the stress waves at interface propagate at a different velocity compared to the
waves travel along the center of the homolite. There must be some changing of
configurations of contour patterns as functions of time. Figure 5 superimpose the contour
plots on top of the stress profile plots so that any change in contour configuration can be
directly related to the stress profiles. Compare the zone configurations of the two time

instants, it is clear that the contour lines in the linearly increasing friction zone are scattering at larger time. This is because the wave velocity of stick zone is larger than that of the stick zone. The scattering of (σ_1-σ_2) fringes in experiments was also seen. Another zone change is the shrinkage of the constant friction stress zone. This indicates that the unloading waves are faster than the interface loading wave in this zone.


(a)

(b)
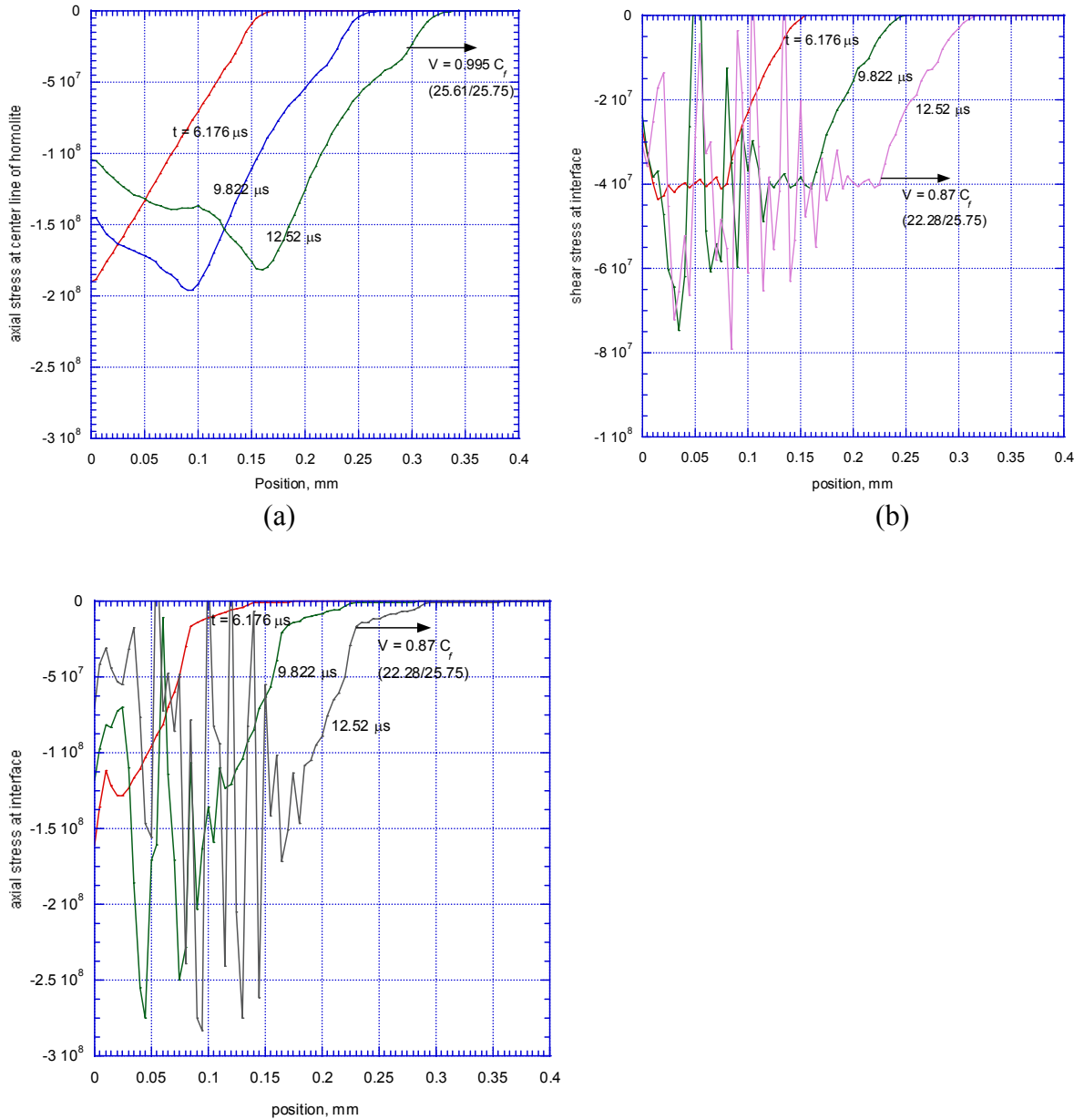
Figure 4   Stress profiles in homolite at three different instant. (a) axial stress (σ_{11}) along the center line of homolite; (b) shear stress (τ_{12}) along the interface.
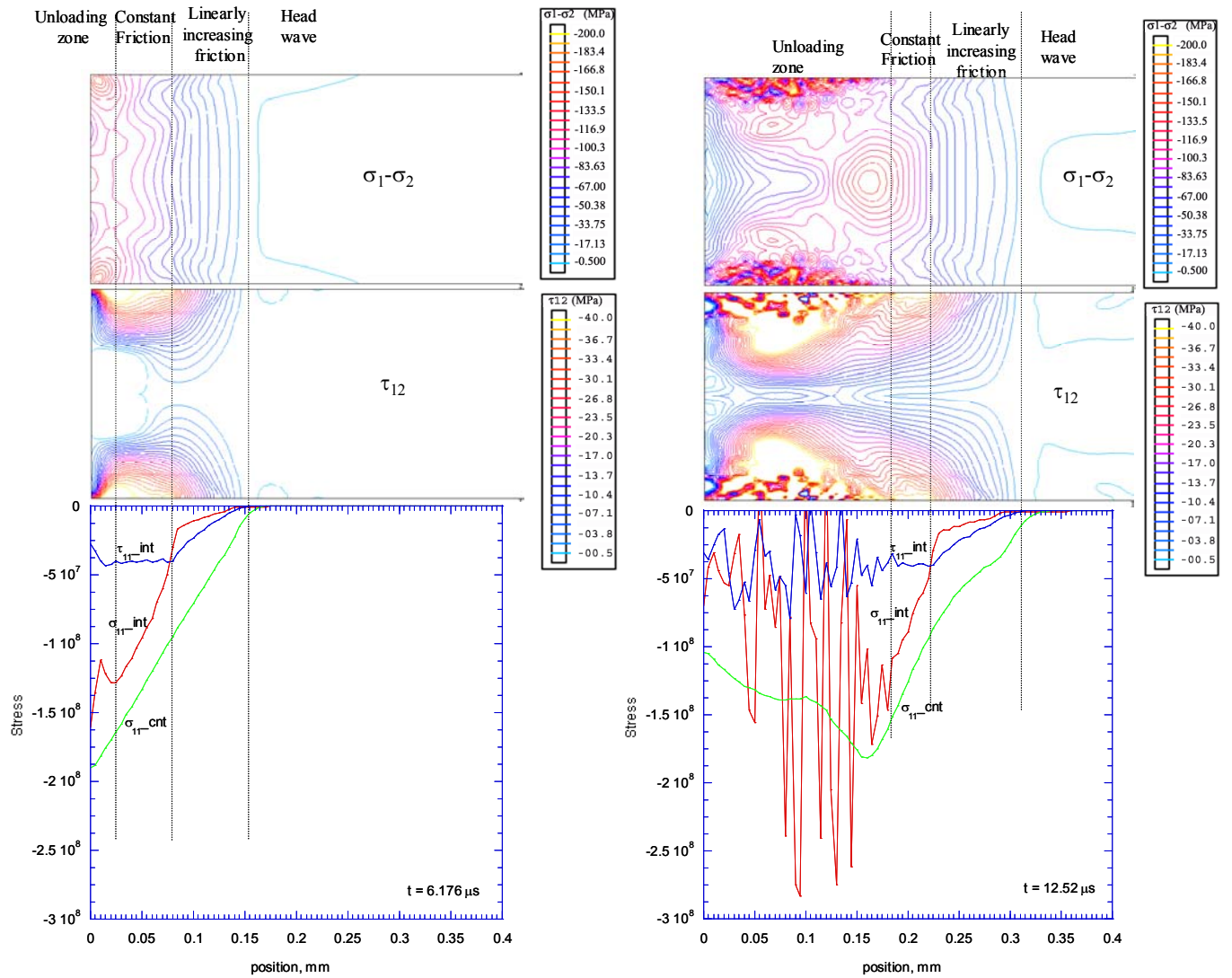
Figure 5   Contour plots imposed on top of stress profiles for two different time instants, t = 6.176 µs, and t = 12.52 µs.

3.3 Issues about Identifying Slip Zone Experimentally

In CalTech's experiments, the slip zone was determined by finding abrupt slope changes of $(\sigma_1-\sigma_2)$ along the interface (Figure 9 of CalTech report). The value of $(\sigma_1-\sigma_2)$ in the sliding zone, $(\sigma_1-\sigma_2)_{sliding}$, may have some indication for evaluating the interface friction stress. Because

$$\sigma_1 - \sigma_2 = \sqrt{(\sigma_{11}-\sigma_{22})^2 + 4\tau_s^2} \ .$$

Further, the experiments showed that the $(\sigma_1-\sigma_2)_{sliding}$ measured is a decreasing function of lateral confinement stress. This is somewhat counter intuitive because usually the larger the lateral confinement level leads to larger friction stress at interface. Therefore, it is worthwhile to investigate further the stress state at interface. Figure 6 gives the stress components along the interface for two levels of interfacial friction stresses, $\tau_s = 20$ MPa (Fig. 6a) and 40 MPa (Fig. 6b). Values of $(\sigma_1-\sigma_2$ calculated from the three stress components are superimposed on the figures. It is very clear that there is a distinct change of slope in $(\sigma_1-\sigma_2$ at the beginning of slip zone (constant friction zone). The magnitude of $(\sigma_1-\sigma_2$ is approximately $2\tau_s$. However, the magnitude of $(\sigma_1-\sigma_2)$ continues to increase after the turning point – there is no explicit relation between of $(\sigma_1-\sigma_2)$ and τ_s beyond the turning point.

Note that in Figure 6 the lateral confinement is not included, that is, the stress component σ_{22} is purely from the dynamic loading process. However, the lateral confinement stress can be added in Eqn (1) to reveal how it would affect the $(\sigma_1-\sigma_2)$. Figure 7 gives the results of different lateral confinement levels, 0.5 MPa, 50.0 MPa, 100.0 MPa and 150.0 MPa. It is seen that $(\sigma_1-\sigma_2)$ at turning point decreases with the increase of lateral confinement stress. This may be used to explain the experimental observation (Figure 10 in CalTech's report)
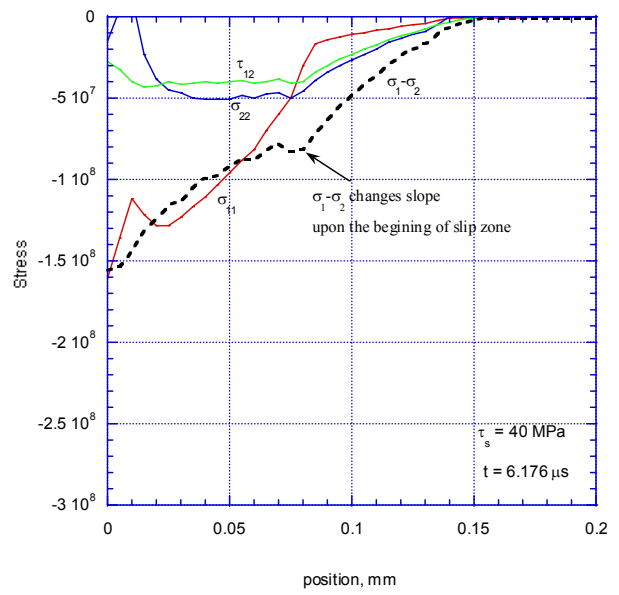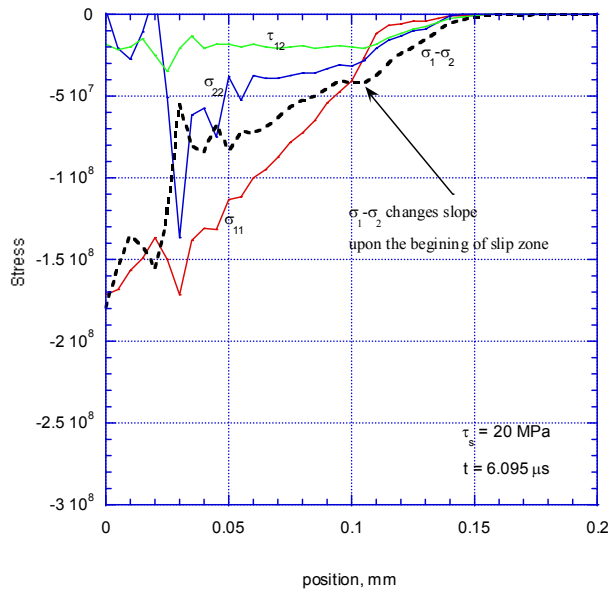
Figure 6
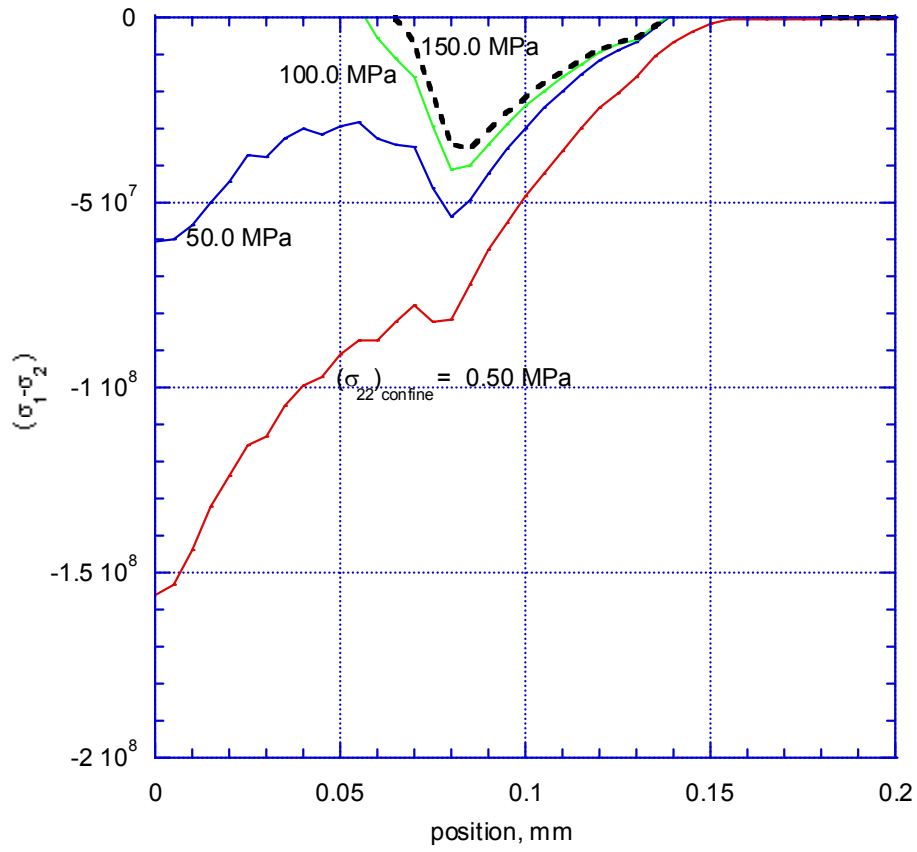
Figure. 7 Influence of lateral confinement pressure on $(\sigma_1-\sigma_2)$

Appendix A

Note for Normalization:

$$E_m \quad \nu_m \quad E_f \quad \nu_f \quad C_m \quad C_f \quad R \quad f \quad \tau_s \quad \dot{\sigma}_t$$

$$- \quad \nu_m \quad \frac{E_f}{E_m} \quad \nu_f \quad - \quad \frac{C_f}{C_m} \quad - \quad f \quad \frac{\tau_s}{E_m} \quad \frac{\dot{\sigma}_t R}{E_m C_m}$$

Experimentally used normalized numbers

$$\frac{E_f}{E_m} = 0.0211; \quad \frac{C_f}{C_m} = 0.3785; \quad f = 0.14; \quad \frac{\tau_s}{E_m} = 9.17E-5; \quad \frac{\dot{\sigma}_t R}{E_m C_m} = 2.19E-4$$

$(\tau_s = 40\,\text{MPa used, corresponding to lateral confinement of } 50\,\text{MPa})$

$(\dot{\sigma}_t = 31.5\,\text{MPa}/\mu\text{s, rising time } 6\,\mu\text{s} - -1/3 \text{ of the impact process})$

The numerical model was scaled to 1/80 (in size) of the experimental model. The equivalence of the numerical model and experimental model was guaranteed by enforcing the dimensionless groups in the numerical model to be identical with the corresponding experimental values. There are multiple ways to achieve this. The one used in this study is

$$E_m' = E_m = 218\,\text{GPa}; \quad \nu_m' = \nu_m = 0.285; \quad C_m' = C_m/80 \ (\rho_m' = 6400\rho_m = 5.12\text{E}7\,\text{kg/m}^3)$$

$$E_f' = E_f = 4.6\,\text{GPa}; \quad \nu_f' = \nu_f = 0.344; \quad C_f' = C_f/80 \ (\rho_f' = 6400\rho_f = 7.872\text{E}6\,\text{kg/m}^3)$$

$$\tau_s' = \tau_s = 20\,\text{MPa}; \quad \dot{\sigma}_t' = \dot{\sigma}_t = 31.5\,\text{MPa}/\mu\text{s}; \quad R' = R/80 = 0.103125$$

Modern Topics and Challenges in Dynamic Fracture

Brian Cox
Rockwell Scientific, LLC
1049 Camino Dos Rios
Thousand Oaks, CA 91360
U. S. A.

Huajian Gao
Max-Planck Institute
Stuttgart
Germany

Dietmar Gross
TU Darmstadt
Darmstadt
Germany

Daniel Rittel
Technion
Israel Institute of Technology
Israel

February, 2004

_____

ABSTRACT

The field of dynamic fracture has been enlivened over the last five years or so by a series of remarkable accomplishments in different fields – earthquake science, atomistic (classical and quantum) simulations, novel laboratory experiments, materials modeling, and continuum mechanics. Important concepts have been discovered for the first time or elaborated in new ways to reveal wider significance. Here the literature of this progress is summarized.

Much of the value of the new work resides in the new questions it has raised, which suggest profitable areas for research in the next few years and beyond. From the viewpoint of fundamental science, excitement is greatest in the struggle to probe the character of dynamic fracture at the atomic scale, using Newtonian or quantum mechanics as appropriate (a qualifier to be debated!). But lively interest is also directed towards modeling and experimentation at macroscales, all the way up to the geological, where the science of fracture is pulled at once by fundamental issues, such as the curious effects of friction, and engineering challenges in applications, where dynamic effects are essential to proper design or certification or manufacture.

INTRODUCTION

At some scale, all fracture is dynamic. Our common experience in the macroscopic world may lead to the generalization that the dynamic nature of fracture is manifest only when the inertia of relatively large pieces of material is large enough that the correct balancing of the energy of fracture requires including kinetic energy. Equivalently, we may say that dynamic (inertial) effects are important when the propagation of stress waves through the material is not very fast relative to the rate of advance of the crack tip. But even when these conditions for dynamic effects at the macroscopic scale are not met, still at the atomic scale, the most fundamental for understanding crack propagation, the inertia of individual atoms must be accounted for in depicting their separation from one another, even when the crack at the macroscopic scale appears to be advancing quasi-statically. Bond rupture (at least at temperatures above absolute zero!) is a dynamic process. The inertia of the atoms involved enters the problem. The dynamic fracture problem is the most fundamental in the science of fracture.

The dynamic fracture literature has been sustained in a wide number of journals by several distinct scientific communities, who have been focused on different objectives. The communities have been divided partly by the scale of the systems they consider, which ranges from single atoms to earthquake fault lines, partly by the phenomena they have chosen to address, and partly by the balance of their leanings towards curiosity-driven science or technology. Some cross-referencing among the different bodies of work is found, but not as much as the inter-relationship between the ideas being explored would justify. Here progress is reviewed in sections that reflect the major boundaries between the dynamic fracture communities, because this is a convenient categorization, but fixed points where analogous results or concepts appear re-scaled or otherwise re-stated in different sections are repeatedly in evidence. A rich prospect would seem to present itself for transferring concepts and methods from one field to another.

Scientific progress has been rapid and fascinating. The technological relevance of dynamic fracture to structures and systems that will sustain impact or ballistic threats remains very high. The insertion of the new scientific and engineering concepts and methods into engineering design is therefore a very timely topic for new research.

1.   Dynamic Fracture at the Geological Scale

Earthquake modeling is concerned with dynamic shear cracks under slow loading. A stream of recent work by Rice and his colleagues has led to new understanding of the complex phenomoena of dynamic cracking under such conditions. First, Ben-Zion and Rice (Ben-Zion and Rice, 1997) developed a dynamic simulation scheme of dynamic shear cracks under slow loading, which was further improved by Lapusta and colleagues (Lapusta *et al.*, 2000). Lapusta and Rice (Lapusta and Rice, 2003) went on to study nucleation of shear cracks and their early dynamic stages in the context of dynamic shear ruptures. They established that nucleation processes of large and small events are very similar. Further, events at different scales interact: the irregular initial dynamic phases of large events are influenced by stress concentrations induced by initiation and arrest of small events.

Self-healing or pulse-like dynamic shear ruptures are also being actively investigated in the field. In a pioneering paper, Heaton (Heaton, 1990) showed that some earthquake observations can be explained if the duration of the dynamic sliding at each point along the interface is short compared to the overall time of the dynamic event. Since then many similar observations have been made. This mode of rupture propagation was called self-healing or pulse-like, in contrast to the "crack-like" mode in which the duration of sliding at a point is comparable to the overall duration of the dynamic event. In parallel theoretical work, Zheng and Rice (Zheng and Rice, 1998) demonstrated conditions under which crack-like rupture modes are indeed replaced by pulse-like modes at velocity-weakening interfaces. Adams (Adams, 1998) further demonstrated that the dynamic coupling in the frictional relationship between normal stress and shear displacement discontinuity (slip) leads to pulse-like slip on a generic bimaterial interface. Andrews and Ben-Zion (Andrews and Ben-Zion, 1997) were the first to simulate a slip pulse on a dissimilar material interface with a constant coefficient of friction. They observed splitting of the pulse which was later shown, in a fundamental revelation concerning the nature of friction, to be the consequence of ill-posedness of the problem when formulated with constant friction. Ranjith and Rice (Ranjith and Rice, 2001) took up this problem using stability analysis to demonstrate a wide range of parameters for which the problem of dynamic sliding with a constant coefficient of friction is ill-posed. They proposed a regularization procedure based on an experimentally based law in which the shear strength in response to an abrupt change in normal stress evolves continuously with time or slip toward the corresponding Coulomb strength. Cochard and Rice (Cochard and Rice, 2000) proved the validity of the analytical results of Ranjith and Rice by numerical simulations of dynamic slip on dissimilar material interfaces.

This important line of research has shown that rupture along a bi-material interface has remarkable dynamic properties that may be relevant to many problems, over broad ranges of scales, from geophysics to composite materials. The problem has the fascinating feature that it starts in a situation well-posed as a static continuum problem but evolves dynamically to a non-continuum state of slip pulses. Recent papers on this topic include, e.g., (Ben-Zion, 2001; Ben-Zion and Huang, 2002; Ranjith and Rice, 2001).

The effects of non-linear rheology that extends beyond the elastic regime, which create some interesting and important characteristics in studies of general dynamic cracks (see below), are also beginning to attract attention in earthquake studies. The work by Huajian Gao (Gao, 1996; Gao, 1997) on hyperelasticity and Phillipe Geubelle on damage covers some general aspects of this broad topic. Related studies on the evolution of earthquakes and faults can be found in (Lyakhovsky *et al.*, 1997; Lyakhovsky *et al.*, 2001) and (Ben-Zion and Lyakhovsky, 2002).

2.   Dynamic Fracture at the Atomic Scale

A broad development that many participants of the workshop found particularly inspiring and at times simply beautiful is the bridge that has grown between continuum and atomic (or other discrete) descriptions of dynamic fracture. Lectures that contributed to the impression that the bridge is real and present include those by Farid Abraham, Huajian Gao, Mike Marder, David Kessler, and Peter Gumbsch. *In his keynote lecture*, Farid

Abraham gave a condensed overview of how the rapid advance of computer power during the few decades of his career has revolutionized the field. In 1965, a typical problem addressed by computational physicists consisted of about 100 atoms. By the turn of 21st century, the system size has reached 1 billion atoms, roughly corresponding to a cubic crystal of 250 nm in edge length. This size is certainly in the regime where a "hand shake" to continuum formulations becomes possible. Abraham showed spectacular examples (Abraham *et al.*, 2002) of his 1-billion-atom simulations of work hardening and supersonic fracture. He predicted by 2007 that the state of the art will have reached a trillion atoms and simulations on the billion-atom level will become routine. This puts the pace of development in the field into a nice perspective.

Atomistic studies, largely represented by molecular dynamics simulations, have been used significantly in the past to provide fundamental understanding of underlying basic physical processes of dynamic fracture, rather than being predictive or specific to a particular material. Examples are the method of lattice dynamics modeling, which originated with Leonid Slepyan and is advocated by Mike Marder and David Kessler (Marder and Gross, 1995; Slepyan, 1981); or Farid Abraham's studies of simple model materials. While Abraham et al. (Abraham *et al.*, 1994) opened up the possibility of studying fracture through large-scale simulations of model materials, the question remains (especially in the minds of experimentalists!) of how much applicability such results have. This is particularly an issue given the very complex microstructure on different length scales in real materials and – in contrast – the often very simple and ideal microstructure in simulations. More studies are obviously needed to provide a more seamless bridge between atomistic approaches and continuum scale theory and experimentation (rather than "isolated" results that are possibly only valid in very specific cases). This is a challenging task given the fact that fracture is a very complex process.

However, there are some promising areas where the atomistic viewpoint has been successfully coupled to continuum scale theory or experiments. An example of such "handshaking" of experiment-theory-simulation is the intersonic fracture of mode II cracks, where experiments by Ares Rosakis (Rosakis *et al.*, 1999) have stimulated recent MD simulations of Abraham and Gao (Abraham and Gao, 2000). The MD simulations were able to match essential features of intersonic fracture that are observed in the experiments and also predicted by cohesive modeling (Needleman, 1999) and continuum elasticity (Gao *et al.*, 2001).

Atomistic studies are often associated exclusively with molecular dynamics simulations. During the workshop, Mike Marder and David Kessler pointed out that an alternative class of analytical methods developed by Slepyan (Slepyan, 1981; Slepyan, 2002), using a formulation where atoms remain associated with particular points on a lattice, can also and in much smaller computations reveal insight into atomic-scale dynamic fracture. For example, Marder and Gross (Marder and Gross, 1995) made use of Slepyan's technique to calculate a velocity gap and transverse instability during dynamic crack propagation. Hauch and colleagues (Hauch *et al.*, 1999) attempted to compare theory and experiment for brittle fracture without phenomenological parameters. Starting from the atomic point of view, Gao and colleagues (Gao *et al.*, 2001) demonstrated existence of intersonic cracks under shear dominated conditions, while Gerde and Marder (Gerde and Marder, 2001) demonstrated the existence of self-healing cracks under mixed-mode conditions.

Some open questions regarding atomistic modeling were raised during the workshop. How predictive are atomistic simulations of dynamic fracture? How can we develop tools that model very complex fracture processes such as the collapse of a building? A rather radical view articulated by Mike Marder is that atomistic simulations could eventually be developed into practical tools for engineers. One thing that can be safely said is that atomistic modeling will play an increasingly important role in the next decades along with the rapid advance of computer power. Molecular dynamics could potentially be an important part of multi-scale methods describing very complex processes. An important issue is the development of multiscale methods such as continuum methods which incorporate atomistic information. Examples are the VIB method by Gao, Klein, Huang and coworkers (Gao and Klein, 1998; Klein *et al.*, 2001; Zhang *et al.*, 2002) and the concurrent multiscale methods where some regions are treated by finite elements while others are treated by molecular dynamics, such as the At-FE method (Kohlhoff *et al.*, 1991), quasi-continuum method (Shenoy *et al.*, 1998) and the MAAD method (Broughton *et al.*, 1999).

In some cases, model potentials and classical molecular dynamics fail to explain the observed dynamic fracture phenomena and quantum mechanics modeling appears to be required. The lecture by Peter Gumbsch illustrated this point for cleavage fracture in silicon. Pérez and P Gumbsch (Pérez and Gumbsch, 2000a; Pérez and Gumbsch, 2000b) showed that anisotropy in the preferred cleavage direction in silicon, which is experimentally well documented, can only be explained on the basis of quantum mechanical (density functional theory) calculations. Gumbsch (Gumbsch, 2001) discussed some general aspects of atomistic modeling of fracture including bond breaking, lattice and bond trapping, and relevant energies. He emphasized the importance of realistic descriptions of the atomic interaction for the atomistic modelling of fracture processes, showing that the quantum mechanical (DFT) results for the bond breaking process in silicon and the existence of directional anisotropy can only be reproduced with advanced tight binding methods (De Vita and Car, 1998) and not with simple potentials in a classical MD simulation. While the pseudopotential approximation used in the quantum calculations, which precludes relaxation of core electron states, may also be questioned when atomic separations undergo the large changes characteristic of fracture, nevertheless the warning is laid down: classical mechanics may be inherently inadequate for understanding the most fundamental aspects of fracture.

Other experimental studies on single crystal silicon partly confirm theoretical ideas and partly confute modelers by pointing out further complexity. Thus, addressing the existence of a velocity gap in silicon, Sherman et al. (Sherman and Be'ery, 2003) recently produced evidence of cracks propagating at very low velocities under controlled conditions in silicon. However, further work from the same group discovered new mechanisms for the deflection of a crack from one cleavage system to another as a function of crack velocity and crystallographic orientation (Sherman and Be'ery, 2003). Shilo and colleagues demonstrated, both experimentally and by modeling, the potentially important interaction of a crack in silicon with microstructural defects (dislocations) and ramifications for the stability of the crack-front (Shilo *et al.*, 2002).

A method that aims between the quantum and classical formulations has been suggested by De Vita and Car (De Vita and Car, 1998), who developed a new method of

dynamically fitting empirical potentials in the region of interest to forces calculated from quantum methods. The computational approach includes refitting the forces after a short time interval to guarantee accurate match with the ab initio forces at particular epochs.

Further work from the group of Peter Gumbsch (Rudhart *et al.*, 2003) addressed dynamic fracture in quasi-crystals, a class of materials structurally between glass and crystal, and found distinct changes in fracture mode with temperature. The fracture modes in quasi-crystals include brittle fracture, brittle fracture following "virtual" dislocation emission and at high temperature, glass-like breaking of bonds in front of the actual crack tip, and crack growth by linking of these microcracks.

3. Dynamic Fracture at the Macroscopic Scale

Fracture Roughness, Crack Front Waves, and Dissipation Mechanisms

Measurements and modeling of fracture surface roughness in materials of different type, including ductile alloys and brittle glasses, and under dynamic and static loading, has led to new insight into the conditions for crack propagation. First, remarkably similar self-affine fracture surface morphology has been observed in fatigue fractures in metals and stress corrosion cracks in glasses (Daguier *et al.*, 1997), a result that has stimulated a search for mechanisms that could be universal to such disparate cases. A further clue on the trail came from molecular dynamics simulations, which showed that similar morphology can also arise in the fracture of glass in the dynamic regime (Nakano *et al.*, 1995). Other simulations revealed that a dynamic crack in amorphous glass propagates by the nucleation and coalescence of cavities, much as a crack in a ductile metal (Celarie *et al.*, 2003; van Brutzel *et al.*, 2002). Thus apparently similar roughness is found in static, stress corrosion, and dynamic cases; and theory hints at universality among very different material classes. A separate and rather provocative theoretical study has further suggested that *only* dynamic conditions near the crack tip can account for the roughness; dynamic stress transfer affects the crack tip conditions significantly even in cracks that are propagating quasi-statically from the macroscopic view (Ramanathan *et al.*, 1997).

Simultaneously with these developments, basic mathematical tools were developed by Willis and colleagues for analyzing in-plane and out-of-plane perturbations of a propagating crack front and dynamic stress transfer during crack propagation (Willis and Movchan, 1995; Willis and Movchan, 1997). These techniques have found immediate application in understanding various features of earthquake rupture and they have been used, in particular, to study crack front waves for generic dynamic cracks (Morrissey and Rice, 1998; Ramanathan and Fisher, 1997)**.** In the latter works, a localised perturbation of a propagating crack front has been shown to be able to propagate without decay along the crack front, resulting in a new kind of wave, called a crack front wave, which is a distinct mode from the classical longitudinal, shear, and Rayleigh wave modes. The association was then suggested, that crack front waves may be responsible for the small-scale, self-affine fracture surface roughness found experimentally and in simulations for so many different materials in both dynamic and (macroscopically) static loading (Bouchaud *et al.*, 2002).

Attempts have been made at direct experimental verification of crack front waves, but the outcome remains subject to some controversy. Fineberg and co-workers reported observations of solitary waves, which they inferred to be crack front waves (Sharon *et al.*, 2001). However, K. Ravi-Chandar has claimed contrary experimental evidence, which seems to indicate that the solitary waves observed in the experiments of Fineberg may be due to an interaction between shear waves and the propagating crack front. More experiments, and perhaps large-scale molecular dynamics simulations, are obviously needed to settle this fundamental point.

Fracture surface roughness may also be the result of microcracking, which is an important dissipation mechanism for a broad class of materials (Ravi-Chandar and Yang, 1997; Sharon *et al.*, 1996; Washabaugh and Knauss, 1994). Microcracks can roughen cracks by acting as nuclei for macroscopic crack branching; and they can lead by this and by other mechanisms to shielding and amplification effects. When numerous microcracks appear as a cloud, they reduce the effective stiffness of the material surrounding the macroscopic crack tip so that the effective wave speed and therefore the crack speed through the damaged material are reduced (Gao, 1996) and the macroscopic fracture toughness increases. Early studies of the effect of diffuse microcracks used spatial averaging to develop a phenomenological cohesive law that reduced the nonlinear material to a narrow band or line of displacement discontinuity. The evolution of the damage zone was modeled (*Dietmar, is this correct? If not, what di you mean by "cohesive laws"?*) ~~Smearing out discrete microcracking by purely phenomenological cohesive laws, the evolution of such a damaged process zone during dynamic cracking was studied by Yang and Ravi-Chandar~~ (Yang and Ravi-Chandar, 1996) and Johnson (Johnson, 1992). More advanced studies by Gross and colleagues represent the microcracks individually, using a time domain boundary element method, which is particularly efficient for multiple crack problems in homogeneous materials (i.e., when heterogeneous elasticity is unimportant *is this a correct restriction?*). Crack closure effects have been taken into account and crack branching and the interaction between macro and microcracks during crack growth have been investigated in detail (Rafiee *et al.*, 2003; Rafiee *et al.*, 2004; Seelig and Gross, 1997; Seelig and Gross, 1999). These studies show that microcracking can explain the increase of fracture toughness with crack velocity and also predict an upper bound for the crack velocity *please correct this – I was looking for something more explicit (without actually reading the papers!)*, which lies far below the Rayleigh wave speed. These results agree well with theoretical and experimental findings of other authors (Hawong and Kobayashi, 1987; Ramulu and Kobayashi, 1985; Shukla *et al.*, 1990). Since boundary element methods facilitate the analysis of arbitrary crack paths and the formation of microcracks, crack branching, crack closure and friction, they are being adopted and further developed as an appropriate tool for other macroscopic problems, ~~like~~ including problems at the geophysical scale (Fedelinsky and M.H. Aliabadi, 1997; Tada and Yamashita, 1997).

Question: I am not sure whether the problems of dynamically loaded stationary cracks in layered materials and in piezoelectric materials should be touched. Furthermore, what about the (dynamic) problem of dislocation emission from crack tips: explanation of rate dependence of fracture toughness. In these fields a number of papers appeared during the

past 5 years. B: this is an effort question of effort, among other things. We can always add a statement that we are focusing on the Ringberg themes, which were not exhaustive. Otherwise, would you like to take it on, Dietmar!?

Initiation and Propagation Criteria

The question of the correct way of stating the condition for static crack propagation has lain unresolved at the heart of static fracture mechanics since its inception. In many engineering applications, especially involving single cracks, conditions based on energy release rate or critical stress intensity factors have enjoyed great practical value. However, cases exist with quasi-static loading where an energy condition clearly predicts the wrong crack path; and cases are ubiquitous where a dominant stress singularity is a fundamentally unrealistic view of crack tip conditions. Now, from the work on crack front waves and its possible dominance of fracture surface roughness, it would appear that the ultimate answer to the quasi-static fracture criterion may not be approachable by calculations of static behaviour alone but may lie in essentially dynamic phenomena.

A problem that may turn out to be closely related to crack front waves and surface roughness is the so-called failure mode transition first identified in experimental work by Kalthoff (Kalthoff, 1988). (Brian, I don't think this is related so much to the above issues, but rather a new type of failure mechanism that appears only for mode II loading, not for mode I, and that is closely related with thermoplastic coupling. I suspect this effect is quite general for materials that posess plastic deformation capability along with some tendency to shear localization) Depending on the impact velocity, a shear loaded crack may propagate either under local opening (mode I) conditions, by deflecting through a kink angle, or in mode II, along its initial direction, by forming an adiabatic shear band. This transition, which has been observed for a variety of metallic alloys (Zhuo *et al.*, 1996) and commercial polycarbonate (Ravi-Chandar, 1995; Rittel, 1998) *Is this the correct paper of Dany's?* implies velocity dependence in the failure criterion. One criterion proposed is a simple rate dependent critical mode II fracture toughness (Kalthoff, Ringberg workshop). But one would guess that the mode II toughness is likely to be affected by friction, which will be affected by fracture surface roughness; and so a possible connection to work on crack front stability and crack front waves is completed (here I agree).

In an early, seminal work on initiation, using deeply notched, thin sheets of Homalite loaded in mode I by a clever electromagnetic method, Ravi-Chandar and Knauss (Ravi-Chandar and Knauss, 1984) showed strong correlation between the onset of crack propagation and the crack tip stress intensity factor. Thus for engineering applications, the idea of a dynamic initiation toughness arises, in analogy to the fracture toughness used in quasi-static fracture, where the critical toughness might be a material constant that could be measured in a simple standard experiment. However, the definition of a standard experiment to measure dynamic toughness has not been straightforward. Rittel et al. (Rittel *et al.*, 1992) have proposed and developed some simple methods, but a crucial difficulty arises in determining the time of initiation. This issue relates to the three-dimensional nature of the fracture process: all measurements probe only the surfaces of the specimen, so that the moment of advance of a submerged crack tip, and thus the stress state at the crack tip at the critical instant, is difficult to know. A second challenge arises: while ample evidence shows that initiation toughness depends on the

loading rate, there is no clear relationship between this trend and material type, so that predictive capability is still limited. The resolution of this doubt must lie in experiments that reveal fracture micromechanisms operating in each specific material. Some recent work indicates the power of such evidence in understanding engineering initiation data. For example, commercial polymethylmethacrylate (plexiglass) shows a large increase in initiation toughness with the loading rate (Rittel and Maigre, 1996), which is associated with a marked increase of the roughness of the fracture surface next to the fatigue pre-crack front. This suggests a transition in damage mechanism involving the possible creation of multiple microcracks under the passage of the first stress wave, to an extent that depends on loading rate. Further supporting this idea, numerous non-propagating microcracks have been found in dynamically loaded cermets (porous ceramic matrix infiltrated with a metallic binder), which are absent in statically loaded material of markedly lower initiation toughness (Rittel *et al.*, 2003). But the details of how microcracks interact with the main crack in the stage of damage development that can be identified with engineering initiation remain unresolved.

Cohesive Element Modeling – Links to Atomistics

Perhaps the most important development in computational fracture mechanics in the last decade has been the introduction and refinement of the cohesive element methods (Camacho and Ortiz, 1996; Xu and Needleman, 1994). Cohesive elements introduce the possibility of tractions surviving across fracture surfaces after the propagation of a crack and, furthermore, allow the crack to follow any path during a simulation, rather than being confined to a pre-determined path. Some very appealing simulations have recently appeared of multiple crack development and other complex fracture habits, which could not be realized using prior methods in which the fracture paths had to be specified a priori (Camacho and Ortiz, 1996; Klein *et al.*, 2001; Xu and Needleman, 1994).

However, the newness of cohesive surface methods is evident in the fact that some intrinsic difficulties remain with the original formulations (Klein *et al.*, 2001). The problems include artificial softening of material properties as the size of cohesive elements decreases and mesh dependence in the direction of crack branching (at least at the first onset of a branch). Similar problems have been observed by Falk et al. (Falk *et al.*, 2001). In response to these difficulties, a new class of finite element techniques with dynamic cohesive surfaces has been developed, which appear to relieve constraints on the admissible directions of new fracture surfaces (Zi and Belytschko, 2003). The new elements may lead to significantly improved cohesive method simulations. For some applications, the material itself may provide a length scale for direct application of cohesive methods, such as in the dynamic fragmentation of a granular material *ref to Geubelle (He has no paper yet. Work in progress?)*.

An interesting degree of universality can be discerned in the computational approaches that have evolved in continuum fracture modeling and the older discipline of atomistic studies. In some aspects, the cohesive surface modeling of dynamic fracture can be viewed as incorporating atomic interactions along discrete surfaces.

In the future, it will be important to establish a deeper interaction between experiments and simulations performed at either the atomistic or continuum (cohesive element) scale. It should become an important objective of simulation groups to move beyond idealized

potentials, so that they can extract generally valid information from their simulations and contribute to understanding specific issues in dynamic fracture. Particularly promising areas in which atomistic and cohesive element simulations could play an important role include crack front waves, dynamic crack branching, hyperelasticity, friction, and crack initiation.

4. Experiments

In spite of interesting advances in the realism of numerical simulations, the ultimate reference for newly suggested concepts in dynamic fracture remains, very firmly, experiments. The challenge of obtaining highly resolved, detailed observations of cracks in the dynamic regime continues to be among the most severe in the fracture world (perhaps only rivaled by fracture experiments at very high temperatures). Nevertheless, the dynamic fracture community has recently invented some noteworthy and clever new experiments, from which insight far beyond what was accessible by experiments 20 years ago is now being derived. In these experiments, both materials and mechanics aspects of the dynamic fracture problem have been targeted.

One can broadly distinguish two types of studies in modern experiments. The first concerns single crystals or amorphous polymers. While they have practical relevance in their own right, e.g., cleavage of silicon wafers (see below) and dynamic failure of plastic components, these materials, because of the absence of heterogeneous morphology, may be considered model materials. The second deals with more complex bodies, either structural materials such as multi-phase alloys and composites, or natural systems, including biological materials and the earth's crust.

4.1 Experimental Methods

Perhaps the most informative full-field experimental techniques for revealing the details of interactions between stress waves and propagating cracks are based on optical interference. While the methods of caustics seems to be less used nowadays, optical interferometric techniques, such as dynamic photoelasticity and the coherent gradient sensor method (CGS) have gained increased popularity (Rosakis, 1993). The latter especially has been developed into a powerful and convenient tool for recording displacement gradients and stress fields. In an elastic material, the displacement gradient contours measured by CGS correspond to the stress difference, σ_1 - σ_2, where (x_1, x_2) are the in-plane coordinates. Early work used photographic film and rotating mirrors, but now similarly high density information can be recorded with film replaced by programmable high speed digital cameras, with current systems yielding a total of about 48 frames at rates in excess of $2.5 \ 10^6$ per second. (e.g., (Coker and Rosakis, 2001)). Brian this reference is not specific to high speed cameras. So whe should perhaps omit it for this specific issue. *Dany, I did find statements about rate of data acquisition in this paper. Are there better references to quote about modern data speeds? Please specify.*

Beyond imaging of displacement fields, much can be learned about dynamic fracture from thermal and optical emissions. Temperature fields contain direct information about the thermodynamics of nonlinear processes, both at the crack tip and in the crack wake, especially, in the latter region, friction due to sliding crack contact. Direct measurements

of temperature changes due to friction are now possible with high speed infra-red array imaging devices, although the pixel resolution remains very modest, due to delays in transferring the data from the device to storage (e.g., (Zehnder and Rosakis, 1991)). Despite the limited resolution of this device, the thermal structure of an adiabatic shear band could nevertheless be characterized for the first time, and as technology progresses, one can expect the development of high speed thermal cameras that will complement existing high speed optical cameras. Moreover, one may now think of coupling the high speed cameras to appropriate microscopic lenses to reveal unprecedented information about dynamic fracture phenomena at the microscale. At present, such a direct link to microstructure is still missing for all the phases of dynamic fracture, namely initiation, propagation, and arrest. At the macroscale, inferences of temperature can be made in earthquake slip zones by examining the crystallographic phases found along the fault (Otsuki *et al.*, 2003)).

In laboratory tests, temperature measurements have occasionally led to surprising implications. For example, thermoelastic coupling effects (changes of temperature with elastic strain) have commonly been assumed to be negligible, based on experience with smooth specimens. However, recent work (Rittel, 1998) *correct ref?* has shown that this is not always the case: in brittle polymeric materials, the crack-tip temperature may drop significantly upon rapid loading. Such a thermoelastic effect may be important in the ductile to brittle transition and deserves additional study and incorporation alongside plasticity effects in modeling the overall crack-tip thermodynamics.

Light emission during fracture has also been the subject of numerous investigations, ranging from ice to metal through ceramics, carried out mostly by physicists (see e.g., (Yasuda *et al.*, 2002)). These fascinating results remain largely isolated from the mainstream of dynamic fracture experiments. Nevertheless, the advent of sophisticated atomic scale simulations, including quantum calculations of changes in electronic state during dynamic fracture, opens the possibility of using light emission to test models of some of the most fundamental aspects of fracture.

The quest for understanding mechanisms of dynamic fracture during earthquakes (the geological scale) has led to an exciting advance in laboratory experimental methods, with relevance to all scales. Ares Rosakis and colleagues have demonstrated that some key features of earthquake dynamics, including intersonic rupture and rupture initiation under slip or velocity weakening friction laws, can be captured in the laboratory using PMMA plates held together by friction forces under compression. This is interesting because there is an enormous difference in length scales between seismic faults and laboratory materials. A "laboratory earthquake" is initiated along a set of pre-designed fault lines (material boundaries) by an electric spark that simulates a seismogenic source. Pulsed slip ensues, similar to that in an earthquake slip event. While the simulation in a small specimen of events occurring naturally on a geological scale is eye-catching, the same experimental technique may prove equally valuable in probing dynamic friction effects in structural materials, such as laminated composites. The technique has the potential of being further developed into a unique experimental platform to test ideas and models of mode II and mixed mode cracking under various loading, environmental, and materials conditions. An example demonstrated by Rosakis is the study of dynamic branching and transfer of slip along interacting fracture planes (fault lines or material interfaces), with

results comparable to seismic measurements and theoretical models developed by Rice and co-workers (Kame *et al.*, 2003; Poliakov *et al.*, 2002).

Such novel laboratory experiments provide bridges not only between theory and observations but also between small and large-scale phenomena. A coherent approach combining traditional seismic and fracture measurements and theoretical modeling with modern laboratory experimental tools and large-scale computer simulations may revolutionize the fields of seismology and dynamic structural design.

4.2   Challenges for Experimenters

Major experimental challenges remain, in both fundamental and engineering aspects of dynamic fracture. One issue of continuing engineering importance is the problem of defining and characterizing a condition for crack initiation under dynamic conditions. For example, in many structures intended for long life, initiation of a single crack under a rare dynamic load, e.g., foreign object damage in an aircraft turbine blade, can be enough to reduce the fatigue life under normal duty cycling quite dramatically.

In more recent work, Sharon and Fineberg (Sharon and Fineberg, 1996) produced a large body of experimental evidence related to the evolution of crack velocity and the nature of the micromechanisms that lead to crack branching. Crack branching was also investigated by Ravi-Chandar and Yang (Ravi-Chandar and Yang, 1997), in terms of activation of secondary microcracks near the main crack-tip. Yet, looking beyond such investigations, the role of the microstructure in the dynamic fracture process – its effect on crack branching, initiation, etc. – remains very much an open question. This problem is not totally new, having concerned pioneers in the field of quasi-static material fracture, such as the late A.S. Tetelman (Tetelman and McEvily Jr., 1967). Yet, new tools, such as high speed optical and thermal cameras coupled to microscopes and sophisticated numerical codes will allow a re-examination of the structure-property relationship. In the modern context, some new aspects of this overarching problem challenge experimenters. For example, dynamic delamination in composites poses difficult questions regarding multiple cracking, mixed mode propagation, and the effects of long zones of friction in the crack wake (see Section 7).

Additional work on crack propagation in single crystals of sapphire has led to new appreciation of the complexity of the creation of fracture surface roughness in the context of nonlinear dynamics (Sherman and Be'ery, 1998) *correct ref?*. These authors analyzed crack profiles in a sapphire single crystal and concluded that the governing equation of motion contains seven independent dynamical variables.

Finally, natural materials, other than engineering alloys or polymers are also investigated for their dynamic fracture behavior. As an example, the dynamic ejection of magma that occurs during a volcanic eruption represents a challenge in both experimental and analytical terms. Here, one deals with the dynamic fracture of a highly viscous material that contains numerous bubbles. The rate of decompression will affect the nature of the volcanic eruption and the related damage. A series of experimental results can be found in Ichihara et al. (Ichihara et al., 2002), in which the failure process is analyzed using fluid mechanics concepts. For this example, dynamic fracture mechanics concepts should yield new insights into the phenomenon. Indeed, first of all,

the experiments show a ductile to brittle transition of the failure mode with the (decompression) rate. Additional work is needed to characterize the failure micromechanisms of this complicated bubbly material, and their rate sensitivity. Ultimately, the fragmentation process can be analyzed using fragmentation models in which the (dynamic) fracture toughness of the material appears explicitly, thus establishing an additional link between mechanics and physics of fracture in geomaterials. *I wonder about omitting this work, at the risk of offending Ichihara, because I don't understand what it has to do with dynamic fracture. Am I missing something? As you wish! This is dynamic fragmentation in fact and not f.m. oper-se. Yet, the dynamic fracture/fragmentation of a viscous material is stuill an open question with huge implications, as in the present case. OK, I'm being thick again. Is there any dynamic fracture in Ichihara's paper? If not, then we would need a statement of what the physics was that she included and then an argument that one really ought instead to include dynamic fracture to be able to understand the magma problem. (Once again I'm trying to avoid work! Dany, do you want to re-write this?)*

5.   Intersonic and Supersonic Fracture

Intersonic fracture has attracted much attention in the last few years, mainly due to the Ares Rosakis' experimental work (Rosakis *et al.*, 1999) which has motivated the cohesive modeling (Needleman and Rosakis, 1999) Geubelle and Kubair 2001), and the molecular dynamics studies (Abraham and Gao, 2000; Gao *et al.*, 2001). The lecture by Yonggang Huang presented the fundamental solution of intersonic mode II cracks (Huang and Gao, 2001). The fundamental solution has been used by the group of Wei Yang (Guo and Yang, 2003) to construct transient solutions of intersonic crack propagation.

A comprehensive review of the historical development of studies on intersonic cracks can be found in Rosakis (Rosakis, 2002). In the past decade, scientists working at all length scales, from the atomistic, the continuum, all the way up to scale of geological ruptures, have undertaken joint efforts to study this unexplored area of fracture mechanics. Early contributions to the theoretical literature of dynamic subsonic and intersonic fracture highlights significant differences between tensile and shear cracks. Direct laboratory observations (Rosakis *et al.*, 1999) have provided a framework for discussing the physics of intersonic shear rupture occurring in constitutively homogeneous (isotropic and anisotropic) as well as in inhomogeneous systems, all containing preferable crack paths or faults. Experiments, models, simulations and field evidence at all length scales have been used to discuss processes such as shock wave formation, large-scale frictional contact and sliding at the rupture faces, and maximum attainable rupture speeds. This topic is of particular interest to the exploration of intersonic fault rupture during shallow crustal earthquake events.

Another important field that was tackled at the workshop was supersonic fracture, a phenomenon totally unexplained by the classical theories of fracture. Molecular dynamics simulations by the group around Abraham and Gao (Abraham *et al.*, 2002; Buehler and Abraham, 2003) have shown the existence of intersonic mode I and supersonic mode II cracks. This has motivated a recent continuum mechanics analysis of supersonic mode III cracks by Wei Yang (Guo and Yang, 2003). Huajian Gao discussed

recent progress in theoretical understanding of hyperelasticity in dynamic fracture and showed that the phenomenon of supersonic crack propagation could only be understood by introducing a new length scale, called χ, which governs the process of energy transport near a crack tip. The crack dynamics is completely dominated by material properties inside a zone surrounding the crack tip with characteristic size equal to χ. When the material inside this characteristic zone is stiffened due to hyperelastic properties, cracks propagate faster than the longitudinal wave speed. The research group of Gao has used this concept to simulate the Broberg problem of crack propagation inside a stiff strip embedded in a soft elastic matrix. The simulations, which confirmed the existence of an energy characteristic length, were reported during the workshop (Buehler and Abraham, 2003). This study also has implications for dynamic crack propagation in composite materials. If the characteristic size of the composite microstructure is larger than the energy characteristic length, χ, models that homogenize the materials into an effective continuum would be in significant error. During the workshop, fruitful interactions between Gao's simulation groups and experimentalists, in particular Rosakis and Ravi-Chandar, led to ideas for the design of experiments to verify the energy characteristic length. The ultimate goal would be to conduct experiments on supersonic cracks to test the predictions of the simulations and analysis.

While much excitement rightly centers around the relatively new activity related to intersonic cracking, an old but interesting possibility remains to be incorporated in the modern work: interface crack propagation that is subsonic but exceeds the Rayleigh wave speed has been predicted for at least some combinations of elastic properties of the two joined materials (Goldstein, 1966).

6.   Friction

Friction effects dominate many problems of dynamic fracture, but friction remains one of the least understood aspects of material behaviour.

Most earthquakes propagate along existing fault lines. The dynamic slip process is complicated by the fact that fault zones contain many rock types, which exhibit distinct mechanisms during crack propagation. The fault zone generally consists of layers of finely granulated rock, created by the fragmentation, melting, and recrystallization of rock during many prior slip events. The fragments or grains within a fault line exhibit a range of sizes extending over one or two orders of magnitude (Chester *et al.*, 1993; Otsuki *et al.*, 2003; Wibberley and Shimamoto, 2003). This suggests that dynamic slip might tend to fragment fault material in such a way that the total fraction of space occupied by the grains is maximized. The grain pattern is reminiscent of the Sierpinski gasket, with smaller grains lying in the interstices of larger grains, in a pattern that recurs down through many length scales. However, the fractal dimension of the grain pattern varies from one slip system to another, suggesting that melting and fragmentation occur at different rates depending on the rock composition in a particular fault. The relation between material composition and the details of nonlinear mechanisms in fault zones, including fragmentation and the resulting distribution of particle sizes, remains obscure.

An analogous situation exists in delamination cracking of many structural materials. Layers of rubble, which have at least superficial morphological similarity, but on much

smaller scales, to earthquake fault lines, are also pervasive in predominantly mode II cracks in brittle polymer or ceramic materials, especially delamination cracks propagating between plies in a laminated structure. In such materials, the origins of the rubble can be traced to systems of microcracks that form in layers subjected to shear (Bradley and Cohen, 1985; Fleck, 1991; Xia and Hutchinson, 1994). At large displacements, these microcrack systems coalesce to form entirely detached particles in a layer. Since crack displacements far exceed the particle size in the further crack wake, one infers that shear tractions are transferred across the crack by a mechanism analogous to that acting in the rubble layer in an earthquake fault line, but with the characteristic length scales being four or more orders of magnitude smaller (Massabò and Cox, 1999; Rice, 1980a). Under dynamic loading conditions, adiabatic heating of the rubble layer is, again in attractive analogy to the geological case, likely to cause some melting and therefore rate-dependence through dynamic viscosity.

In both earthquake and structural simulations and models, the action of material along a slip line is represented as friction, i.e., a relationship between the shear traction supported, the prevailing compressive stress across the slip line, and the displacement discontinuity (and its rate, etc.). Since the dynamics of friction at the scale of individual grains in a slip line is very complicated, simple Coulomb friction cannot be expected to be correct; both rate effects and non-linear proportionality will be the norm. Non-Coulombic friction can also be inferred directly from certain characteristics of dynamic mode II crack propagation. Zheng and Rice have shown, for example, that self-healing or pulse-like crack propagation, which is the prevalent mode of earthquake motion, requires a velocity-weakening friction law (Zheng and Rice, 1998). In a structural or laboratory context, Ranjith and Rice demonstrated that ill-posedness in generic dynamic sliding problems involving dissimilar materials can be regularized by assuming that friction responds slowly to an abrupt change in the compressive stress (Ranjith and Rice, 2001). Understanding the relation of these inferred characteristics to material processes remains a challenge.

The constitutive behaviour of dry and cool granular material is a complicated problem of load transfer through random contacts that change in time. The outcome is strongly affected by the state of hydrostatic compression, rate effects, and the magnitude of the shear displacements. Work to date on this problem has been confined to large aggregates of powder (Anand, 1983; Nemat-Nasser, 2000) *check Anand's 1993 paper* rather than the thin layers expected in the wake of a crack, with applications to ballistics, shear faulting in shock compression, etc. (Nesterenko, 2001). In ballistic applications, constitutive modeling is often reduced to representing comminuted (fragmented) material trapped ahead of a penetrator as a viscous fluid, whose viscosity originates in friction at the contact points of individual particles. In an engineering sense, such models have been at least partially successful in demonstrating the relation between armour design and ballistic performance. However, such constitutive modeling is too crude to permit credible inferences about the role of material type and morphology in determining friction (viscous flow) effects in fracture. Extension of the more complete models of granular mechanics to the conditions found in a dynamic crack remains to be made.

The problem of predicting crack branching and bifurcation is also related to the phenomenon of fragmentation during dynamic wave propagation, which has received

some attention by approximate analytical methods. In the simple case of fragmentation of a brittle homogeneous medium subject to uniaxial stress waves, Drugan derived a characteristic length, l_{min}, for the minimum elastic fragment size, which is related to the wave speed and a cohesive law that is similar to that used in the first cohesive element finite element methods (Drugan, 2001). His length scale can be re-written within a factor of order unity as $l_{min} = \delta^* E / 2\sigma_{max}$, where δ^* and σ_{max} are the critical displacement and stress in the cohesive law and E is a reduced modulus. This result is curiously similar in form to the characteristic bridging length scale, l_{ch}, introduced by Hillerborg, Rice and others to characterize the length of the bridging zone in a bridged static crack (Cox and Marshall, 1994; Hillerborg *et al.*, 1976; Massabò and Cox, 1999; Rice, 1980b). However, Drugan's length scale is independent of the shape of the cohesive law for displacements beyond the critical displacement. The length scale, l_{ch}, is more often written in bridged crack work as $l_{ch} = GE/\sigma_{max}^2$, where G is the fracture energy (total area under the cohesive law), and only takes the form $l_{ch} = \delta^* E / 2\sigma_{max}$ in the special case of a Dugdale law (rectangular cohesive law, $G = \sigma_{max}\delta^*$). Why information about the nature of the cohesive law beyond the critical displacement, δ^*, should have no effect on the size of elastic fragments, as in Drugan's length scale, is an issue for further consideration. Analytical models that deal with the entire domain of the cohesive traction/displacement law and form a link to computational work on cohesive elements (Section 3 above), in which the tail of the traction law has a strong effect, would be timely.

The length scale characterizes the zone of stress relief on either side of an existing crack and is therefore a measure of the fragment size. An analogue of this effect could account for regularly spaced branch cracks in dynamic fracture simulations (who showed these at Ringberg?). A related length scale, perhaps involving the shear wave speed, may appear in the creation of arrays of cracks under dynamic mode II conditions. While this simple concept provides insight into the first fracture of an elastic material under dynamic overload, little insight is yet available into the subsequent maturation of first crack systems into granulated material or the progression of large displacements through that material. If earthquake fault lines are taken as indicators, high deformation will create a distribution of grain sizes ranging over several orders of magnitude – there is a tendency away from any single length scale and towards scale invariance. Experiments of granulation effects in polymer and ceramic composites, especially for mode II delaminations, would be most revealing.

The dominance of friction in various dynamic problems has been well illustrated in recent work. In fiber pullout, for example, which is the main mechanism of toughening of brittle matrix composites, the presence of friction modifies the nature of the propagating stress wave in two fundamental ways (Cox *et al.*, 2001; Nikitin and Tyurekhodgaev, 1990; Sridhar *et al.*, 2003). Under smoothly varying loading, the furthest propagation of the stress disturbance propagates not at the bar wave speed, but at a reduced speed which depends on the loading rate. Second, when interactions between the loaded fiber and the matrix are taken into account, even simple time-linear loading results in quite complex possibilities of slip, stick, and reverse slip domains, propagating along the fiber matrix interface. Which pattern of domains is observed depends on the loading rate and material parameters. For loading that varies in time in a non-linear manner, the patterns of slip become extremely complicated. This character forms a

strong contrast with the same problem in the static case, for which elementary solutions, which have been the basis of many engineering material designs, can be written down for arbitrary loading and unloading cycles.

One result of particular significance for dynamic fracture in structures relates to laminates in which through-thickness reinforcement is present. Through-thickness reinforcement is often introduced to increase delamination resistance, which it does very effectively. Importantly, experiments and theory have both shown that, for common through-thickness reinforcement types, such as stitches and rods, mode I displacements tend to be suppressed more effectively than mode II displacements, for both static and dynamic loading (Massabò and Cox, 2001). Consequently, a strong engineering principle is implied: that robust or damage tolerant laminated structures will tend to delaminate in mode II and therefore their failure habits will be dominated by friction. This represents a major departure in emphasis from prior work, the great majority of which has studied mode I fracture (where friction is irrelevant). The mode I case is increasingly appearing to be an academic ideal, with the important issues of engineering design depending on mode II behaviour.

7.   Problems in Materials Design and Engineering Certification

A new class of materials, the functionally graded materials, has been the subject of recent dynamic fracture studies. These materials are designed especially such as to optimize a given property, such as fracture toughness. Both layered and continuously graded materials have been thoroughly investigated by Shukla and his group (Chalivendra *et al.*, 2002; Chalivendra *et al.*, 2003; Parameswaran and Shukla, 1998; Parameswaran and Shukla, 1999), experimentally and analytically. An important result was that the square-root singularity remains valid but the higher order terms are influenced by the grading of the material, in other words by its microstructure. Numerical simulations on such cracked materials under impact loading recently have been done by Sladek and colleagues (Sladek *et al.*, 2004).

8.   Dynamic Fracture for Device Manufacture

This paragraph was moved here from Dany's experimental section Michael Marder reviewed a fascinating new application dynamic fracture in device manufacture. In recent pioneering work, dynamic fracture was used to cleave a silicon single crystal along a plane along which a crack cannot normally propagate stably. The crystal was doped by ion bombardment with impurities, which changed the atomic interactions along the desired plane of fracture and a smooth cleavage was then achieved by loading the crystal dynamically. Here would appear to be an excellent show-case for the potential of atomistic or quantum simulations for exploring and optimizing a practical process.

8.   The Future – Unsolved Problems in Dynamic Fracture

Research over the last five to ten years has brought forward numerous fundamental insights into the nature of dynamic fracture. New theoretical and experimental methods, discoveries made in studies at all scales (from the atomic to the geological), and the (relatively recent) venture of dynamic fracture researchers into problems of real

structures, have all contributed to making the field rich in ideas, possibilities, and – most gratifyingly to the curious – unsolved problems that are fundamental in nature and wide-ranging in relevance.

What are the problems whose solution could change the way we conceive of dynamic fracture?

1.

With the preparation of The implications for understanding complex fracture processes at all scales are profound. the field has been supported by a number of interested agencies in a somewhat fragmentary way, from earthquakes to quantum simulations, in work supported mainly by small grants from very diverse sources. In spite of the relatively small scale of support and the (incorrect) opinion in uninterested agencies and researchers that dynamic fracture is a solved or marginal problem, the involved community has a very strong and active spirit. A particularly rewarding result of the Ringberg Workshop was that, out of many diverse interests, such a strong sense of the universality of dynamic fracture arose that much hope was created for future advances by collective action.

The importance of coordinated or collective action for the future must be emphasized. There is a palpable gap between the really interesting new fundamental work that is going on and the needs of engineers in materials design, system certification, and manufacture (yes, dynamic fracture as a manufacturing method!). Because of this, the problems being taken up or the manner in which they are being posed are not necessarily those that would have the most benefit. While value remains in research that is driven by curiosity alone, the field of dynamic fracture suggests great rewards can also be found by posing basic research problems to respond directly to applications needs.

References

Abraham F, Gao H (2000). How Fast Can Cracks Propagate? *Physical Review Letters* 84(3113-3116.

Abraham F, Walkup R, Gao H, Duchaineau M, D. DLRT, Seager M (2002). Simulating Materials Failure by Using Up to One Billion Atoms and the World's Fastest Computer: Brittle Fracture. *Proceedings of the National Academy of Sciences of USA* 99(5777-5782.

Abraham FF, Brodbeck D, Rafey RA, Rudge WE (1994). Instability Dynamics of Fracture: A Computer Simulation Investigation. *Physical Review Letters* 73(2):272-275.

Adams GG (1998). Steady Sliding of Two Elastic Half-Spaces with Friction Reduction due to Interface Stick-Slip. *Journal of Applied Mechanics* 65(470-475.

Anand L (1983). Plane Deformations of Ideal Granular Materials. *Journal of the Mechanics and Physics of Solids* 31(105-122.

Andrews DJ, Ben-Zion Y (1997). Wrinkle-Like Slip Pulse on a Fault Between Different Materials. *Journal of Geophysical Research* 102(553-571.

Ben-Zion Y, Rice JR (1997). Dynamic Simulations of Slip on a Smooth Fault in an Elastic Solid. *Journal of Geophysical Research* 102(17,771-17,784.

Ben-Zion Y (2001). Dynamic Rupture in Recent Models of Earthquake Faults. *Journal of the Mechanics and Physics of Solids* 49(2209-2244.

Ben-Zion Y, Huang Y (2002). Dynamic Rupture on an Interface Between a Compliant Fault Zone Layer and a Stiffer Surrounding Solid. *Journal of Geophysical Research* 107(DOI 10.1029/2001JB000254.

Ben-Zion Y, Lyakhovsky V (2002). Accelerated Seismic Release and Related Aspects of Seismicity Patterns on Earthquake Faults. *Pure and Applied Geophysics* 159(2385-2412.

Bouchaud E, Bouchaud JP, Fisher DS, Ramanathan S, Rice JR (2002). Can Crack Front Waves Explain the Roughness of Cracks. *Journal of the Mechanics and Physics of Solids* 50(1703-1725.

Bradley WL, Cohen RN (1985). Matrix Deformation and Fracture in Graphite Reinforced Epoxies. In: Delamination and Debonding of Materials: ASTM, pp. 389-410.

Broughton JQ, Bernstein N, Kaxiras E, Abraham F (1999). Concurrent Coupling of Length Scales: Methodology and Application. *Physical Review B* 60(2391-2403.

Buehler MJ, Abraham FF (2003). Hyperelasticity Governs Dynamic Fracture at a Critical Length Scale. *Nature* 426(141-146.

Camacho GT, Ortiz M (1996). Computational Modelling of Impact Damage in Brittle Materials. *International Journal of Solids and Structures* 33(2899-2938.

Celarie L, Prades S, Bonamy D, Ferrero L, Bouchaud E, Guillot C, Marliere C (2003). Glass Breaks like Metal, but at the Nanometer Scale. *Physical Review Letters* 90(075504-1-4.

Chalivendra VB, Shukla A, Parawesmaran V (2002). Asymptotic Stress Fields for Stationary Cracks along the Gradient in Functionally Graded Materials. *Journal of Applied Mechanics* 69(240-243.

Chalivendra VB, Shukla A, Parawesmaran V (2003). Dynamic Out of Plane Displacement Fields for an Inclined Crack in Graded Materials. *Journal of Elasticity* 69(99-119.

Chester FM, Evans JP, Biegel RL (1993). Internal Structure and Weakening Mechanisms of the San Andreas Fault. *Journal of Geophysical Research* 98(771-786.

Cochard A, Rice JR (2000). Fault Rupture Between Dissimilar Materials: Ill-Posedness, Regularization, and Slip-Pulse Response. *Journal of Geophysical Research* 105(25891-25907.

Coker D, Rosakis AJ (2001). Experimental Observations of Intersonic Crack Growth in Asymmetrically Loaded Unidirectional Composite Plates. *Philosophical Magazine* 81(3):571-595.

Cox BN, Marshall DB (1994). Concepts for Bridged Cracks in Fracture and Fatigue. *Acta Metallurgica et Materialia* 42(2):341-363.

Cox BN, Sridhar N, Beyerlein I (2001). Inertial Effects in the Pullout Mechanism During Dynamic Loading of a Bridged Crack. *Acta Materialia* 49(3863-77.

Daguier P, Nghiem B, Bouchaud E, Creuzet F (1997). Pinning and Depinning of Crack Fronts in Heterogeneous Materials. *Physical Review Letters* 78(1062-1065.

De Vita A, Car R (1998). A Novel Scheme for Accurate MD Simulations of Large Systems. Symposium on Tight-Binding Approach to Computational Materials Science: Materials Research Society, Warrendale, Pennsylvania.

Drugan WJ (2001). Dynamic Fragmentation of Brittle Materials: Analytical Mechanics-Based Models. *Journal of the Mechanics and Physics of Solids* 49(1181-1208.

Falk ML, Needleman A, Rice JR (2001). A Critical Evaluation of Cohesive Zone Models of Dynamic Fracture. *Journal de Physique IV* 11(43-50.

Fedelinsky P, M.H. Aliabadi MH (1997). The Time-Domain DBEM for Rapidly Growing Cracks. *International Journal of Numerical Methods in Engineering* 40(1555-1572.

Fleck NA (1991). Brittle Fracture due to an Array of Microcracks. *Proceedings of the Royal Society of London* A432(55-76.

Gao H (1996). A Theory of Local Limiting Speed in Dynamic Fracture. *Journal of the Mechanics and Physics of Solids* 44(1453-1474.

Gao H (1997). Elastic Waves in a Hyperelastic Solid Near Its Plane Strain Equibiaxial Cohesive Limit. *Philosophical Magazine Letters* 76(307-314.

Gao H, Klein P (1998). Numerical Simulation of Crack Growth in an Isotropic Solid With Randomized Internal Cohesive Bonds. *Journal of the Mechanics and Physics of Solids* 46(187-218.

Gao H, Huang Y, Abraham FF (2001). Continuum and Atomistic Studies of Intersonic Crack Propagation. *Journal of the Mechanics and Physics of Solids* 49(2113-2132.

Gerde E, Marder M (2001). Friction and Fracture. *Nature* 413(285-288).

Goldstein RV (1966). On a Steady Motion of a Crack at the Straight Interface of Two Joined Elastic Materials. *Solid Mechanics (Mekhanika Tverdogo Tela)* 5(93-102.

Gumbsch P (2001). Brittle Fracture and the Breaking of Atomic Bonds. In: Materials Science for the 21st Century: JSMS, The Society of Materials Science, pp. 50-58.

Guo GF, Yang W (2003). Supersonic Crack Growth in a Solid of Upturn Stress-Strain Relation under Anti-Plane Shear. *Journal of the Mechanics and Physics of Solids* 51(1971-1985.

Hauch J, Holland D, Marder M, Swinney HL (1999). Dynamic Fracture in Single-Crystal Silicon. *Physical Review Letters* 82(3823-3826.

Hawong JS, Kobayashi AS (1987). Dynamic Crack Curving and Branching under Biaxial Loading. *Experimental Mechanics* 27(140-153.

Heaton TH (1990). Evidence for and Implications of Self-Healing Pulses of Slip in Earthquake Rupture. *Phys. Earth and Planet. Inter.* 64(1-20.

Hillerborg A, Modeer M, Petersson PE (1976). Analysis of Crack Formation and Crack Growth in Concrete by Means of Fracture Mechanics and Finite Elements. *Cement and Concrete Research* 6(773-782.

Ichihara M, Rittel D, Sturtevant B (2002). Fragmentation of a Porous Viscoelastic Material: Implications to Magma Fragmentation. *Journal of Geophysical Research - Solid Earth* 106(B10):2226-2239.

Johnson E (1992). Process Region Changes for Rapidly Propagating Cracks. *International Journal of Fracture* 55(47-63.

Kalthoff JF (1988). Shadow Optical Analysis of Dynamic Fracture. *Optical Engineering* 27(835-840.

Kame N, Rice JR, al. e (2003). Effects of Prestress State and Rupture Velocity on Dynamic Fault Branching. *Journal of Geophysical Research - Solid Earth* 108(Art. No. 2265.

Klein PA, Foulk JW, Chen EP, Wimmer SA, Gao H (2001). Physics-Based Modeling of Brittle Fracture: Cohesive Formulations and the Application of Meshfree Methods. *Theoretical and Applied Fracture Mechanics* 37(

Kohlhoff S, Gumbsch P, Fischmeister HF (1991). Crack-Propagation In Bcc Crystals Studied With A Combined Finite-Element And Atomistic Model. *Philosophical Magazine* A64(4):851-878.

Lapusta N, Rice JR, Ben-Zion Y, Zheng G (2000). Elastodynamic Analysis for Slow Tectonic Loading with Spontaneous Rupture Episodes on Faults with Rate- and State-Dependent Friction. *Journal of Geophysical Research* 105(23765-23789.

Lapusta N, Rice JR (2003). Nucleation and Early Seismic Propagation of Small and Large Events in a Crustal Earthquake Model. *Journal of Geophysical Research* 108(doi:10.1029/2001JB000793.

Lyakhovsky V, Ben-Zion Y, Agnon A (1997). Distributed Damage, Faulting, and Friction. *Journal of Geophysical Research* 102(27635-27649.

Lyakhovsky V, Ben-Zion Y, Agnon A (2001). Earthquake Cycle, Fault Zones, and Seismicity Patterns in a Rheologically Layered Lithosphere. *Journal of Geophysical Research* 106(4103-4120.

Marder M, Gross SP (1995). Origin of Crack Tip Instabilities. *Journal of the Mechanics and Physics of Solids* 43(1-48.

Massabò R, Cox BN (1999). Concepts for Bridged Mode II Delamination Cracks. *Journal of the Mechanics and Physics of Solids* 47(1265-1300.

Massabò R, Cox BN (2001). Unusual Characteristics of Mixed Mode Delamination Fracture in the Presence of Large Scale Bridging. *Mechanics of Composite Materials and Structures* 8(61-80.

Morrissey JW, Rice JR (1998). Crack Front Waves. *Journal of the Mechanics and Physics of Solids* 46(467-487.

Nakano A, Kalia RK, Vashista P (1995). Dynamics and Morphology of Brittle Cracks: A Molecular Dynamics Study of Silicon Nitride. *Physical Review Letters:*3138-3141.

Needleman A (1999). An Analysis of Intersonic Crack Growth under Shear Loading. *Journal of Applied Mechanics* 66(847-857.

Needleman A, Rosakis AJ (1999). The Effect of Bond Strength and Loading Rate on the Conditions of Governing the Attainment of Intersonic Crack Growth Along Interfaces. *Journal of the Mechanics and Physics of Solids* 47(2411-2445.

Nemat-Nasser S (2000). A Micromechanically-Based Constitutive Model for Frictional Deformation of Granular Materials. *Journal of the Mechanics and Physics of Solids* 48(1541-1563.

Nesterenko VF (2001). Dynamics of Heterogeneous Materials New York: Springer.

Nikitin LV, Tyurekhodgaev AN (1990). Wave Propagation and Vibration of Elastic Rods with Interfacial Frictional Slip. *Wave Motion* 12(513-526.

Otsuki K, Monzawa N, Nagase T (2003). Fluidization and Melting of Fault Gouge During Seismic Slip: Identification in the Nojima Fault Zone and Implications for Local Earthquake Mechanisms. *Journal of Geophysical Research* 108(B4)*:*ESE 4-1 - 4-18.

Parameswaran V, Shukla A (1998). Dynamic Fracture of a Functionally Gradient Material having Discrete Property Variation. *Journal of Material Science* 33(3303-3311.

Parameswaran V, Shukla A (1999). Crack Tip Stress Fields for Dynamic Fracture in Functionally Gradient Materials. *Mechanics of Materials* 31(579-596.

Pérez R, Gumbsch P (2000a). Directional Anisotropy in the Cleavage Fracture of Silicon. *Physical Review Letters* 84(5347.

Pérez R, Gumbsch P (2000b). An ab-initio Study of the Fracture Anisotropy of Silicon. *Acta Materialia* 48(4517.

Poliakov ANB, Dmowska R, al. e (2002). Dynamic Shear Rupture Interactions with Fault Bends and Off-Axis Secondary Faulting. *Journal of Geophysical Research - Solid Earth* 107(Art. No. 2295.

Rafiee S, Seelig T, Gross D (2003). Simulation of Dynamic Crack Curving and Branching under Biaxial Loading by a Time Domain Boundary Integral Equation Method. *International Journal of Fracture* 120(545-561.

Rafiee S, Gross D, Seelig T (2004). The Influence of Microcrack Nucleation on Dynamic Crack Growth - a Numerical Study. *Engineering Fracture Mechanics* 71(849-857.

Ramanathan S, Ertaz D, Fisher DS (1997). Quasistatic Crack Propagation in Heterogeneous Media. *Physical Review Letters* 79(873-876.

Ramanathan S, Fisher DS (1997). Dynamics and Instabilities of Planar Tensile Cracks in Heterogeneous Media. *Physical Review Letters* 79(877-880.

Ramulu M, Kobayashi AS (1985). Mechanics of Crack Curving and Branching - a Dynamic Fracture Analysis. *International Journal of Fracture* 27(187-201.

Ranjith K, Rice J (2001). Slip Dynamics at an Interface Between Dissimilar Materials. *Journal of the Mechanics and Physics of Solids* 49(341-361.

Ravi-Chandar K, Knauss WG (1984). An Experimental Investigation into Dynamic Fracture. 1. Crack Initiation and Arrest. *International Journal of Fracture* 25(2):247-262.

Ravi-Chandar K (1995). On the Failure Mode Transitions in Polycarbonate under Dynamic Mixed Mode Loading. *International Journal of Solids and Structures* 32(6/7):925-938.

Ravi-Chandar K, Yang B (1997). On the Role of Microcracks in the Dynamic Fracture of Brittle Materials. *Journal of the Mechanics and Physics of Solids* 45(4):535-563.

Rice JR (1980a). The Mechanics of Earthquake Rupture. International School of Physics "E. Fermi", Course 78, 1979: Italian Physical Society/North Holland Publ. Co.

Rice JR (1980b). The Mechanics of Earthquake Rupture. Physics of the Earth's Interior: Italian Physical Society/North Holland Publ. Co.

Rittel D, Maigre H, Bui HD (1992). A New Method for Dynamic Fracture Toughness Testing. *Scripta Metallurgica et Materialia* 26(1593-1598.

Rittel D, Maigre H (1996). An Investigation of Dynamic Crack Initiation in PMMA. *Mechanics of Materials* 23(3):229-239.

Rittel D (1998). Experimental Investigation of Transient Thermoelastic Effects in Dynamic Fracture. *International Journal of Solids and Structures* 35(22):2959-2973.

Rittel D, Frage N, Daniel MP (2003). Dynamic Mechanical and Fracture Properties of an Infiltrated TiC-1080 Steel Cermet.

Rosakis AJ (1993). Two Optical Techniques Sensitive to the Gradients of Optical Path Difference: The Method of Caustics and the Coherent Gradient Sensor (CGS). In: Experimental Techniques in Fracture. JS Epstein editor. New York: VCH, pp. 327-425.

Rosakis AJ, Samudrala O, Coker D (1999). Cracks Faster than the Shear Wave Speed. *Science* 284(1337-1340.

Rosakis AJ (2002). Intersonic Shear Cracks and Fault Ruptures. *Advances in Physics* 51(1189-1257.

Rudhart C, Gumbsch P, Trebin H-R (2003). Crack Propagation in Quasicrystals. In: Quasicrystals: Structure and Physical Properties: Wiley-VCH, Weinheim, Germany, pp. 484-500.

Seelig T, Gross D (1997). Analysis of Dynamic Crack Propagation using a Time-Domain Boundary Integral Equation Method. *International Journal of Solids and Structures* 34(2087-2103.

Seelig T, Gross D (1999). On the Interaction and Branching of Fast Running Cracks - a Numerical Investigation. *Journal of the Mechanics and Physics of Solids* 47(535-563.

Sharon E, Fineberg J (1996). Microbranching Instability and the Dynamic Fracture of Brittle Materials. *Physical Review B* 54(10):7128-7139.

Sharon E, Gross P, Fineberg J (1996). Energy Dissipation in Dynamic Fracture. *Physical Review Letters* 76(12):2117-2120.

Sharon E, Cohen G, Fineberg J (2001). Propagating Solitary Waves along a Rapidly Moving Crack Front. *Nature* 410(68-71.

Shenoy VB, Miller R, Tadmor EB, Phillips R, Ortiz M (1998). Quasicontinuum Models of Interfacial Structure and Deformation. *Physical Review Letters* 80(742-745.

Sherman D, Be'ery I (1998). The Non-Linear Dynamic Rupture in Sapphire. *Physical Review Letters* 80(3):540-543.

Sherman D, Be'ery I (2003). Velocity Dependent Crack Deflection in Silicon. *Scripta Materialia* 49(551-555.

Shilo D, Sherman D, Be'ery I, Zolotoyabko E (2002). Large Local Deflections of a Dynamic Crack Front Induced by Intrinsic Dislocations in Brittle Single Cystals. *Physical Review Letters*.

Shukla A, Nigam H, Zervas H (1990). Effect of Stress Field Parameters on Dynamic Crack Branching. *Engineering Fracture Mechanics* 36(429-438.

Sladek J, Sladek V, Zhang C (2004). An Advanced Method for Computing Elastodynamic Fracture Parameters in Functionally Graded Materials. *Computational Materials Mechanics* in press(

Slepyan L (1981). Dynamics of a Crack in a Lattice. *Soviet Physics Doklady* 26(538-540.

Slepyan L (2002). Models and Phenomena in Fracture Mechanics Berlin: Springer.

Sridhar N, Yang QD, Cox BN (2003). Slip, Stick and Reverse Slip Characteristics during Dynamic Fiber Pullout. *Journal of the Mechanics and Physics of Solids* 51(7):1215 - 1241.

Tada T, Yamashita (1997). Nonhypersingular Boundary Integral Equations for Two-Dimensional Non-Planar Crack Analysis. *Geophysical Journal* 130(269-282.

Tetelman AS, McEvily Jr. A (1967). Fracture of Structural Materials New York, NY: J. Wiley and Sons.

van Brutzel L, Rountree CL, Kalia RK, Nakano A, Vashista P (2002). Dynamic Fracture Mechanisms in Nanostructured and Amorphous Silica Glasses: Million-Atom Molecular Dynamics Simulations. Symposium Proceedings: Materials Research Society.

Washabaugh PD, Knauss WG (1994). A Reconciliation of Dynamic Crack Velocity and Rayleigh Wave Speed in Isotropic Brittle Solids. *International Journal of Fracture* 65(97-114.

Wibberley CAJ, Shimamoto T (2003). Internal Structure and Permeability of Major Strike-Slip Fault Zones : the Median Tectonic Line in Mie Prefecture. *Journal of Structural Geology* 25(59-78.

Willis JR, Movchan AB (1995). Dynamic Weight Function for a Moving Crack. Mode I Loading. *Journal of the Mechanics and Physics of Solids* 43(319-341.

Willis JR, Movchan AB (1997). Three Dimensional Dynamic Perturbation of a Propagating Crack. *Journal of the Mechanics and Physics of Solids* 45(591-610.

Xia ZC, Hutchinson JW (1994). Mode II Fracture Toughness of a Brittle Adhesive Layer. *International Journal of Solids and Structures* 31(1133-1148.

Xu X-P, Needleman A (1994). Numerical Simulations of Fast Crack Growth in Brittle Solids. *Journal of the Mechanics and Physics of Solids* 42(1397-1434.

Yang B, Ravi-Chandar K (1996). On the Role of the Process Zone in Dynamic Fracture. *Journal of the Mechanics and Physics of Solids* 42(1955-1976.

Yasuda K, Shimada M, Matsuo Y (2002). Some Aspects of Photon Emission of Polycrystalline Ceramics During Fracture. *Philosophical Magazine A* 82(17-18):3251-3261.

Zehnder AT, Rosakis AJ (1991). On the Temperature Distribution at the Vicinity of Dynamically Propagating Cracks in 4340 Steel: Experimental Measurements using High Speed Infrared Detectors. *Journal of the Mechanics and Physics of Solids* 39(385-417.

Zhang P, Huang Y, Gao H, Hwang KC (2002). Fracture Nucleation in Single-Wall Carbon Nanotubes Under Tension: a Continuum Analysis Incorporating Interatomic Potentials. *Journal of Applied Mechanics* 69(454-458.

Zheng G, Rice JR (1998). Conditions under which Velocity-Weakening Friction Allows a Self-Healing Versus Cracklike Mode of Rupture. *Bulletin of the Seismological Society of America* 88(1466-1483.

Zhuo M, Rosakis AJ, Ravichandran G (1996). Dynamically Propagating Shear Bands in Impact-Loaded Prenotched Plates. I- Experimental Investigations of Temperature Signatures and Propagation Speed. *Journal of the Mechanics and Physics of Solids* 44(6):981-1006.

Zi G, Belytschko T (2003). New Crack-Tip Elements for XFEM and Applications to Cohesive Cracks. *International Journal for Numerical Methods in Engineering* 57(2221-2240.